ELECTRON AND PROTON ACCELERATION USING THE 30 TW, 30 fs HERCULES LASER

by

Stephen A. Reed

A dissertation submitted in partial fulfillment
of the requirements for the degree of
Doctor of Philosophy
(Applied Physics)
in The University of Michigan
2008

Doctoral Committee:

      Associate Research Scientist Anatoly M. Maksimchuk, Co-Chair
      Emeritus Professor Gérard A. Mourou, Co-Chair
      Professor Roy Clark
      Professor Karl Krushelnick
      Professor Herbert Winful

TO MY MOTHER

    for her magnificent devotion to her children

TO MY FATHER

    for giving without asking for anything in return

ACKNOWLEDGEMENTS

This thesis would not have been possible without the help and support of many good people. First, I would like to thank my thesis supervisor Anatoly Maksimchuk for his guidance, encouragement, and dedication, without which this thesis would not be possible. I want to thank Gérard Mourou, Karl Krushelnick, Roy Clarke, and Herb Winful for serving on my thesis committee and for their support and important suggestions on my research.

Many thanks to Takeshi Matsuoka for his help, friendship, and good company on late nights.

I'd like to thank Vladimir Chvykov, Galina Kalinchenko, Pascal Rousseau, and Victor Yanovsky for their tireless efforts in building and maintaining the Hercules laser.

Many thanks to Stepan Bulanov for his help in PIC simulations and very helpful discussions about our data.

To James Easter, Aghapi Mordovanakis, Porscha McRobbi, Jenny Morris, and Tyacie Corle for their friendship, humor, and support.

I'd like to thank my two brothers Chris and Mike for their kindness and always being there, even when they're not. And lastly, I want to thank my Mom and Dad just for everything. Without you - I wouldn't be where I am today.

TABLE OF CONTENTS

LIST OF FIGURES

LIST OF TABLES

CHAPTER I

Introduction

1.1 Introduction

As laser technology advances and petawatt laser systems become commonplace, exciting new fields of research will continue to develop in high intensity laser physics. For light intensities exceeding 10^{18} W/cm^2, assuming a 1 μm wavelength, the electrons are accelerated to nearly the speed of light in one laser period, defining "optics of relativistic plasmas" as the next fundamental level in laser plasma physics. Within the laser focus, fields exceed 10^{11} V/cm, four orders of magnitude greater than those created at large scale particle accelerators. There, the electron's relativistic mass increases and the laser's magnetic field begins to strongly influence the interaction. The laser pressure becomes billions of times the atmospheric pressure and the plasma generated magnetic fields reach thousands of Tesla, taking place within a multi-million degree plasma. Such conditions are similar to those produced in stars and currently, laser produced plasmas are the only way to replicate such extreme conditions.

Two aspects of particle acceleration from high intensity laser produced plasmas are relevant to this thesis and are described here. The first, is laser accelerated electrons and their important applications in photofission and nuclear activation reactions. The second, is the production of energetic proton beams from high intensity

laser solid interactions and potential applications in medicine.

1.1.1   Laser accelerated electron beams and applications

One of the most fascinating applications of high peak intensity lasers is the acceleration of charged particles (e.g. electrons and protons) over very short distances, typically hundreds of microns to millimeters. High field laser interactions have already merged into the domain of nuclear physics by generating electrons with hundreds of MeV energy [1, 2, 3]. This has enabled tabletop photonuclear physics to be studied in university laboratories. Such energetic electron beams have many potential applications in radiography, and the production of short-lived isotopes such as ^{11}C and ^{18}F used in Positron Emission Tomography (PET) scans.

Recent experiments have shown that a high peak power pulse interacting with an underdense gas leads to quasi monoenergetic electron bunches [1, 2, 3, 4]. The acceleration mechanism dubbed, "bubble" acceleration regime was first predicted by Pukhov and Meyer-ter-Vehn in numerical simulations [5]. Laser nuclear physics was introduced by Boyer *et al.* in 1988 [6] and the first experimental demonstration of laser induced (γ,n) reactions were performed with the NOVA laser [7]. As the high energy photons interact with the atomic nucleus, the giant dipole resonance (GDR) of the nuclei is excited, resulting in the fission of the nucleus or the emission of nucleons. The probability of the reaction taking place increases the closer the photon energy matches the GDR energy. In work presented in this thesis, the quasi-monoenergetic nature of the wakefield accelerated electron is exploited to increase the efficiency of photofission and photonuclear activation reactions. Taking into account the increase in photonuclear efficiency, the transmutation of nuclear waste experiments are still in their infancy because the number of events per second are orders of magnitude

below practical levels.

Additionally, (γ,n) reactions can create short-lived radioactive nuclei which can be used to study how heavy elements were created in the universe [8]. Measuring the dependence of nuclear reaction rates on different plasma conditions will help improve the knowledge of these input parameters in astrophysics models. Improving the reliability of these codes, i.e. the input parameters, is one of the most important issues in astrophysics today. In nature, the synthesis of heavy nuclei is often determined by nuclear reactions involving short-lived radioactive nuclei. Stellar environments such as type II supernovae are the only sites with sufficient energy and density to perform nucleosynthesis. There, reaction rates can compete effectively with decay processes and provide significant production pathways for the synthesis of heavy nuclei. Currently, radioactive ion beams provide the only way of measuring production rates and masses of neutron rich nuclei far from stability which are necessary to achieve a detailed model of nucleosynthesis. Present day sources of neutron-rich radioactive ion beams stem from proton or alpha bombardment to induce fission of targets [8, 9, 10]. However, laser induced photonuclear reactions provide another favorable pathway for production of radioactive species. The lower excitation modes generated by high energy bremsstrahlung result in fission products with less subsequent neutron emission, thus higher production of neutron-rich species. Calculations show that the yields from bremsstrahlung produced isotopes such as ^{132}Sn could be enhanced by two orders of magnitude over current yields from proton-induced fission for the same input power [8]. The generation of γ-rays lying within the giant resonance energy range can be made significantly more efficient with a high energy monoenergetic electron source as discussed in chapter 4. This may allow for the production of various radioactive isotopes necessary to understand the nucleosynthesis of heavy nuclei in

stars.

1.1.2 Laser accelerated proton beams and applications

Laser accelerated proton beams have potential applications in fast ignition for laser fusion [11], probing the electric and magnetic fields in plasmas [12, 13] and the most promising application to date is proton beam radiation therapy [14]. Proton therapy is the most precise form of radiation treatment today. This is because the proton beam radiates the tumor site, leaving surrounding healthy tissue and organs intact. Conversely, X-rays have an exponentially decaying absorption profile, delivering most of the dose near the surface of the skin, as well as, throughout the healthy tissue surrounding the tumor site. In chemotherapy drugs move throughout the entire body, unlike radiation and surgery which are considered "site specific" treatments.

The dominant mechanism involving proton acceleration from ultra-intense laser solid interactions is rear surface acceleration dubbed Target Normal Sheath Acceleration (TNSA). Proton acceleration from micron thick targets is a result of the large, hundreds of GV/m electrostatic fields produced from the charge separation of the hot electrons and ions. The ponderomotive force of the laser pulse accelerates the electrons forward with relativistic velocities while the heavier ions remain relatively stationary, creating a charge separation. This electrostatic field is strong enough to ionize any hydrogen containing material and accelerate protons to several MeV energy.

When protons enter a solid they are stopped by the Coulomb forces of the target atoms. The interaction can be divided into two regimes of energy loss. The first is the electronic interaction. As the proton penetrates the target it displaces the
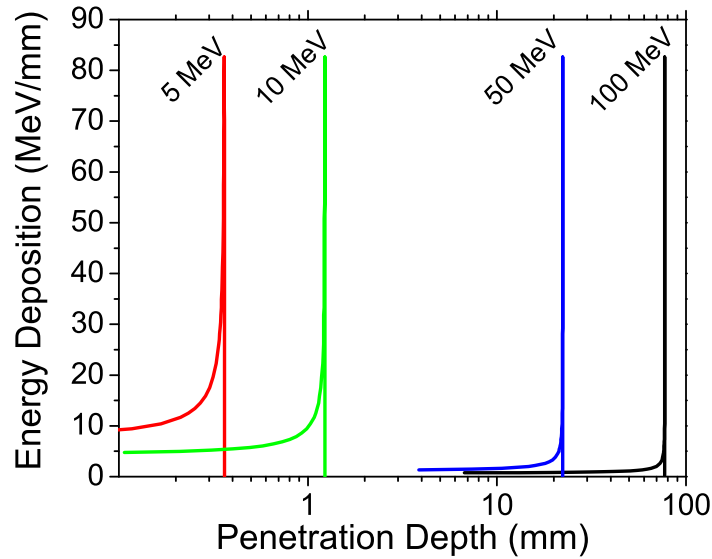
Figure 1.1: The stopping behavior of 5 MeV, 10 MeV, 50 MeV, and 100 MeV protons as a function of depth in water. The plot shows the sharp deposit of energy called the Bragg peak.

electrons along its path causing its velocity to decrease. The second is the nuclear interaction. When the proton velocity is sufficiently slow, elastic scattering by the positive nuclei will cause the proton to come to rest quickly. The sharp increase in absorption at the end of the proton energy range is called the Bragg peak as shown in Fig. 1.1. The proton propagates through most of the bulk material depositing small amounts of energy into the surrounding tissue. Then, at a specific depth, the proton comes to rest and deposits most of its energy.

The total stopping power determines the energy loss of a particle as it propagates though a target material and corresponds to a range which the particle can travel before dissipating its energy (Fig.1.2). The stopping range relevant for cancer therapy is between 1 cm and 20 cm. Therefore, the corresponding proton energy is between 35 MeV and 175 MeV. The stopping power (or deposited energy) in the
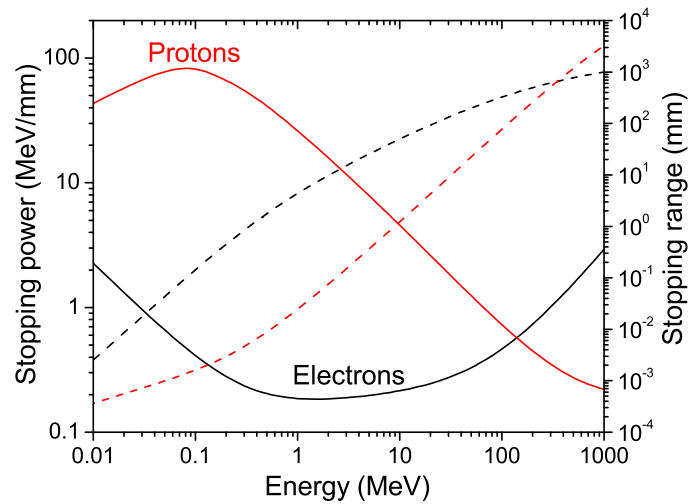
Figure 1.2: Comparison of the stopping powers for electrons and protons in water. The solid line shows the energy loss in MeV/mm. The stopping range is given by the dashed line in mm.

range of interest is much higher for protons than for electrons. Protons also have a higher ionization power than electrons. This is important because radiation therapy attempts to modify the growing cancer cells by altering their DNA preventing replication or simply killing them by direct exposure.

Currently, a major problem with laser accelerated protons is that the energy is too low to be used in cancer therapy. Therefore, techniques for enhancing the proton energy are a topic of experimental and theoretical discussion. Two major advantages of laser accelerated protons are the compactness of the high intensity laser and its potentially low cost.

1.2 Organization of the thesis

This thesis is organized as follows:

Chapter 2 gives a brief overview of the physics of laser plasma interactions at relativistic laser intensities.

Chapter 3 describes the Hercules laser system and the unique characteristics of high intensity and high contrast necessary to perform the presented experiments. First, a general description of the laser system is given. Second, details are described of how to measure and correct the laser wavefront, which is necessary to obtain ultrahigh intensities. Finally, the implementation of a pulse cleaning technique using cross-polarized wave (XPW) generation was developed as part of this thesis, which allows for a record high ASE contrast of 10^{-11}.

Chapter 4 presents the study of electron acceleration from underdense plasmas and describes electron beam energy scaling as a function of plasma density. For the first time, 320 MeV quasi-monoenergetic electron beams are demonstrated from a 40 TW, 30 fs laser focused onto an underdense gas jet. Such quasi-monoenergetic laser wakefield accelerated electrons are used to induce photofission and photonuclear activation with one to two orders of magnitude higher efficiency compared to previous experiments.

Chapter 5 presents, for the first time, an experimental demonstration of a two-stage proton acceleration mechanism. Experimental results show the dependence of the proton beam properties as a function of target material and hydrogen content, from a high intensity (4×10^{20} W/cm^2), high contrast (10^{-11}) laser-plasma interaction. 1-D hydrodynamic simulations were done to describe the effect the prepulse had on proton acceleration for ultrathin targets. Proton acceleration is modeled using 2-D PIC simulations with and without preplasma conditions.

Chapter 6 presents a novel relativistic plasma shutter technique used to increase the laser contrast. This technique is introduced in order to allow for ultrahigh intensity lasers to accelerate protons from 30 nm thick targets. Characteristics of a high intensity, high contrast laser interaction are described are using hydrodynamic and

PIC simulations.

Finally, Chapter 7 summarizes the results and conclusions of the experimentals and simulations and gives perspectives for future experiments.

CHAPTER II

Theory: Physics of High Intensity Laser Plasma Interactions

The experiments described in this thesis deal with laser intensities equal to or greater than $I \simeq 10^{19}$ W/cm^2 corresponding to electric fields on the order of $E_L \sim 10^{11}$ V/cm. Here the electrons are torn away from the nucleus creating plasma temperatures of millions of degrees.

This chapter contains the general background theory necessary to describe laser produced plasmas from basic principles. This chapter is split into 4 sections. The first deals with a single particle in a transverse electromagnetic field, including electron quiver motion and the laser ponderomotive force. Then, collective effects of a large number plasma electrons interacting with an intense laser pulse are described, including Debye-shielding, laser propagation in a plasma, generation of plasma waves and subsequent electron acceleration from underdense plasmas. Section three describes laser energy absorption mechanisms in solid target (overdense) interactions. Finally, proton acceleration in solid targets is described.

2.1 Electron motion in an intense laser field

A free electron in a time varying electric field with frequency ω, oscillates with a classical velocity amplitude, called the quiver velocity given by:

$$v_{osc} = \frac{eE_0}{m_0\omega}. \tag{2.1}$$

In the relativistic regime, the quiver energy of the electrons exceed m_0c^2, where m_0 is the electron rest mass, and c is the speed of light. The dimensionless amplitude a_0 called the *normalized vector potential* serves as a parameter to characterize the strength of the laser field and can be written as:

$$a_0 = \frac{p_0}{m_0c} = \frac{eE_0}{m_0c\omega_0} = \sqrt{\frac{I\lambda_{\mu m}^2}{1.37 \times 10^{18} \ W/cm^2}}, \tag{2.2}$$

where I is the intensity of the laser in W/cm^2 and $\lambda_{\mu m}$ is the laser wavelength in microns. This means, for a $\lambda = 800$ nm wavelength laser pulse, a laser intensity of $I = 2.14 \times 10^{18}$ W/cm^2 corresponds to $a_0 = 1$ which indicates relativistic effects will begin to play a significant role. Now the electron motion is no longer determined by the electric field alone, but the laser's magnetic field becomes important. Fig. 2.1(a) shows the change in a free electron trajectory as the field strength increases from a_0=0.3 to a_0=3.0. The motion of the electrons is described by the Lorenz equation:

$$\mathbf{F} = \frac{d}{dt}(\gamma m\mathbf{v}) = -e(\mathbf{E} + \mathbf{v} \times \mathbf{B}), \tag{2.3}$$

where $\gamma = (1 - v^2/c^2)^{-1/2}$ is the relativistic factor.

Although the laser pulse may have some temporal shape, it may be neglected and assumed the laser is at its maximum value. Assuming a linearly polarized wave propagating in the z-direction with an electric field given by, $\mathbf{E} = E_0\mathbf{e_x}\cos(\omega t - kz)$,
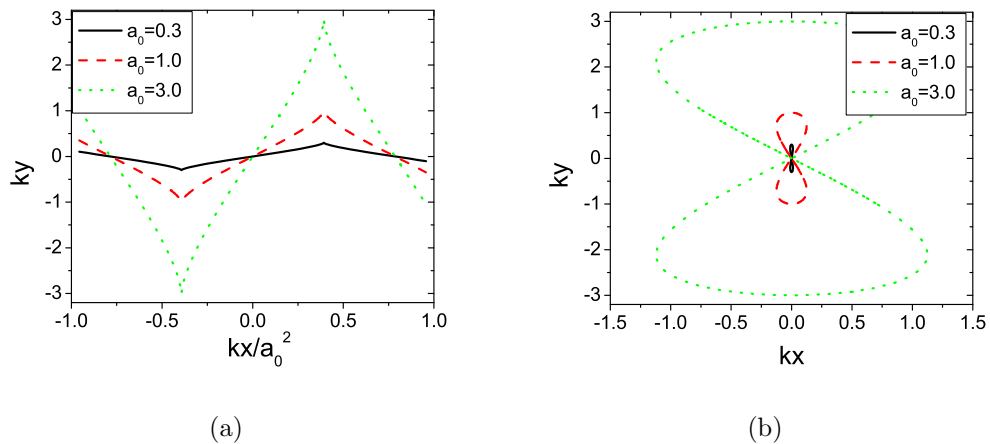
Figure 2.1: The trajectory of a free electron driven by a plane electromagnetic wave is shown for 3 different field strengths both the laboratory frame (a) and the electron rest frame (b).

the motion of an electron can be obtained exactly by analytically solving Eq. (2.3) [15, 16]. Due to the extensive treatment in the literature only the results will be presented here. For electrons initially at rest their relativistic trajectory is described by:

$$k\ x = a_0 \sin \phi, \tag{2.4}$$

$$k\ z = \frac{a_0^2}{4}(\phi - \frac{1}{2}\sin 2\phi), \tag{2.5}$$

where $\phi = \omega t - kz$ is the phase of the electromagnetic field. Due to the magnetic field, the motion in the lab frame of the electron yields a drift in the z-direction with an average velocity of

$$v_{drift}/c = \frac{a_0^2}{4 + a_0^2}. \tag{2.6}$$

Within the electron's rest frame the motion results in a "Figure-8" shaped trajectory. As shown in Eq. (2.5), the transverse oscillation amplitude is proportional to

normalized vector potential, a_0, while the longitudinal momentum is proportional to a_0^2.

2.1.1 Ponderomotive force

In the previous section the electric field was assumed to be an infinitely extended plane wave. However, high intensities can only be achieved by focusing the laser pulse into a spot size on the order of several microns. Here, due to the laser transverse intensity profile, electrons are driven immediately out of the focal region by the high fields in the first half-cycle and feel a weaker force on the return cycle. Therefore, the electron will not return to its original position and is pushed out of the high intensity focal region by a net force called the ponderomotive force. For a high intensity laser pulse with a finite transverse profile this is an effective acceleration mechanism which allows electrons to gain energy from the laser field. The equation of motion for an electron oscillating in an electric field is

$$m\frac{d\mathbf{v}}{dt} = -e\mathbf{E}(\mathbf{r_0}). \tag{2.7}$$

Assuming the electric field has the form $\mathbf{E} = \mathbf{E_0}(\mathbf{r})\cos(\omega t)$ and after linearizing equation (2.7) one obtains

$$m\frac{d\mathbf{v_1}}{dt} = -e\mathbf{E}(\mathbf{r_0}) \tag{2.8}$$

$$\mathbf{v_1} = -\frac{\mathbf{e}}{m\omega}\mathbf{E_0}(\mathbf{r_0})\sin(\omega\mathbf{t}) = \frac{d\mathbf{r}}{dt} \tag{2.9}$$

$$\mathbf{r_1} = \frac{\mathbf{e}}{m\omega^2}\mathbf{E_0}(\mathbf{r_0})\cos(\omega t). \tag{2.10}$$

Next the electric field, $\mathbf{E}(\mathbf{r})$, can be Taylor expanded around the initial position $(\mathbf{r_0})$ of the electrons as

$$\mathbf{E}(\mathbf{r}) = \mathbf{E}(\mathbf{r_0}) + (\mathbf{r_1} \cdot \nabla)\mathbf{E}|_{\mathbf{r}=\mathbf{r_0}} + \cdots \tag{2.11}$$

allowing Eq.(2.7) to be rewritten as

$$m\frac{d\mathbf{v_2}}{dt} = -e[(\mathbf{r_1} \cdot \nabla)\mathbf{E} + \mathbf{v_1} \times \mathbf{B_1}]. \tag{2.12}$$

To obtain $\mathbf{B_1}$ one turns to Faraday's law:

$$\nabla \times \mathbf{E} = -\partial \mathbf{B}/\partial t \tag{2.13}$$

$$\mathbf{B_1} = -\mathbf{1}/\omega \nabla \times \mathbf{E}|_{\mathbf{r}=\mathbf{r_0}} \sin(\omega t). \tag{2.14}$$

Substituting $\mathbf{v_1}$, $\mathbf{r_1}$, and $\mathbf{B_1}$, into Eq.(2.12) and averaging over a laser cycle such that $\langle \cos^2(\omega t) \rangle = \frac{1}{2} = \langle \sin^2(\omega t) \rangle$, the equation of motion becomes:

$$m\frac{d\mathbf{v_2}}{dt} = \frac{-e^2}{2m\omega}[(\mathbf{E_0} \cdot \nabla)\mathbf{E_0} + \mathbf{E_0} \times (\nabla \times \mathbf{E_0})] = \mathbf{f_p}. \tag{2.15}$$

Using the vector identity $\mathbf{A} \times (\mathbf{B} \times \mathbf{C}) = \mathbf{B}(\mathbf{A} \cdot \mathbf{C}) - \mathbf{C}(\mathbf{A} \cdot \mathbf{B})$, one obtains

$$\mathbf{F}_p = -\frac{1}{4}\frac{e^2}{m\omega^2}\nabla E^2, \tag{2.16}$$

given in terms of force per unit volume. This force is prominent in the laser focal volume where the highest intensities are reached on axis. For underdense plasmas the ponderomotive force can "push" electrons off-axis in a process known as plasma cavitation [17].

2.2 Laser interaction with an underdense plasma

To further understand laser plasma interactions the collective behavior of electromagnetic waves propagating through $10^{19}...10^{23}$ electrons/cm^3 must be considered.

Within plasmas, particles remain free to move which screen any chance imbalances. The Coulomb potential of a single particle with charge Ze within a plasma will be modified by the surrounding electrons and become:

$$\Phi_{ion}(r) = \frac{1}{4\pi\epsilon_0}\frac{Ze}{r}e^{-r/\lambda_D} \tag{2.17}$$

where T_e is the plasma temperature in MeV and λ_D is the Debye length given by

$$\lambda_D = \sqrt{\frac{\epsilon_0 T_e}{n_e e^2}}. \tag{2.18}$$

Since plasmas attempt to remain quasi-neutral any displacement of charge will generate a restoring force. The ions are assumed to be infinitely heavy and only serve as a neutralizing background. This approximation is valid since the ions are much heavier than the electrons. The density perturbation is approximated as a sheet of electrons displaced by x, with a given surface charge density $\sigma = -en_e L$, mass $m = m_e n_e L$ and field $E = -\sigma/\varepsilon_0$. The equation of motion can be written as

$$m_e n_e L\frac{d^2 x}{dt^2} = \sigma E = (en_e x)(-en_e L/\varepsilon_0). \tag{2.19}$$

This can be rewritten as a simple harmonic oscillator with a frequency equal to the plasma frequency,

$$\frac{d^2 x}{dt^2} + \omega_e^2 x = 0 \quad \text{where} \quad \omega_e^2 = \frac{n_e e^2}{\epsilon_0 m_e}. \tag{2.20}$$

If the plasma wave is relativistic then the effective mass of the electron is increased by the relativisitic Lorentz factor $\gamma = (1-v^2/c^2)^{-1/2}$, and the electron plasma frequency is given by

$$\omega_e(\gamma) = \sqrt{\frac{n_e e^2}{\epsilon_0 \gamma m_e}} = \omega_e/\sqrt{\gamma}. \tag{2.21}$$

In the case for a general ion species with density, n_i, mass m_i, and charge Ze, the ion plasma frequency is given by:

$$\omega_i = \sqrt{\frac{n_i(Ze)^2}{\epsilon_0 m_i}}. \tag{2.22}$$

2.2.1 Linear propagation

To describe electromagnetic radiation in a plasma one must use Maxwell's equations coupled with the fluid equations. In doing so the three dimensional wave equation has the form

$$\frac{\partial^2 \mathbf{E}}{\partial t^2} - \omega_e^2 \mathbf{E} + c^2 \nabla \times (\nabla \times \mathbf{E}) = 0. \tag{2.23}$$

Because the electron plasma wave oscillates much faster than the ion plasma waves $\omega_e \gg \omega_i$, only the electrons must be taken into account to describe the plasma response to light. If one substitutes an electric field of the form, $\mathbf{E} \propto e^{\mathbf{k}\cdot\mathbf{x} - \omega t}$, into the previous equation, the dispersion relation,

$$\omega^2 = \omega_e^2 + c^2 k^2 \tag{2.24}$$

is obtained, where ω and k are the frequency and wavenumber of the electromagnetic wave, respectively. If the density of the plasma is zero, then $w_e = 0$, and the dispersion relationship for light traveling in free space is obtained, $\omega = ck$. Therefore, a refractive index of the plasma wave can be given by,

$$\eta = ck/\omega = \sqrt{1 - \omega_e^2/\omega^2} = \sqrt{1 - n_e/n_c} \tag{2.25}$$

where n_c is the critical density and is defined when the laser frequency ω equals the plasma frequency ω_e.

$$n_c = \frac{\epsilon_0 m_e \omega^2}{e^2} = \gamma \frac{1.11 \times 10^{21}}{\lambda_{\mu m}^2} [cm^{-3}] \qquad (2.26)$$

It can be seen in the above equation when $\omega_e > \omega$, i.e. $n_e > n_c$, the refractive index becomes imaginary and the light wave cannot propagate in the plasma, being either absorbed or reflected.

2.2.2   Nonlinear propagation

In a plasma, relativistic effects associated with the laser fields can modify the refractive index which in turn alter the laser propagation characteristics. As mentioned earlier, high intensity lasers cause electrons to oscillate with velocities close to the speed of light altering the plasma frequency as shown in Eq.(2.21). This will consequently modify the refractive index given by;

$$\eta(r) = \sqrt{1 - \omega_{pl}^2(r)/\omega^2}, \qquad \omega_{pl}(r) = \sqrt{\frac{n_e(r)e^2}{\gamma(r)m_e\epsilon_0}} \qquad (2.27)$$

Where γ is the relativisitic Lorentz factor $\gamma = \sqrt{1 + a_0^2/2}$ written in terms of the normalized vector potential a_0. Due to the laser's Gaussian spatial profile the laser intensity is peaked on axis causing the refractive index to have a maximum on axis as well. This causes the plasma to act as a positive lens and the laser will self-focus [18]. When the self-focusing of the laser balances diffraction the laser becomes self-guided and takes place for a laser power above the critical power P_c given by [19]

$$P_c = 2\frac{m_e c^2}{e} \frac{4\pi\epsilon_0 m_e c^3}{e} \left(\frac{n_c}{n_e}\right) \simeq 17.4\frac{\omega_0^2}{\omega_p^2} = 17.4\frac{n_c}{n} \ [GW]. \qquad (2.28)$$

When this condition is satisfied the laser beam can effectively propagate in a self-made channel over distances much longer than the Rayleigh range.

2.2.3 Laser wakefield

When an intense laser ($a_0 \gtrsim 1$) propagates through an underdense plasma the ponderomotive force expels electrons from the laser region leaving behind it a plasma wake, also known as a wakefield [20, 21]. The most efficient operation of a laser wakefield accelerator (LWFA) is when the laser pulse length matches half the plasma wavelength,

$$c\tau = \lambda_p/2 = \pi c/\omega_p. \tag{2.29}$$
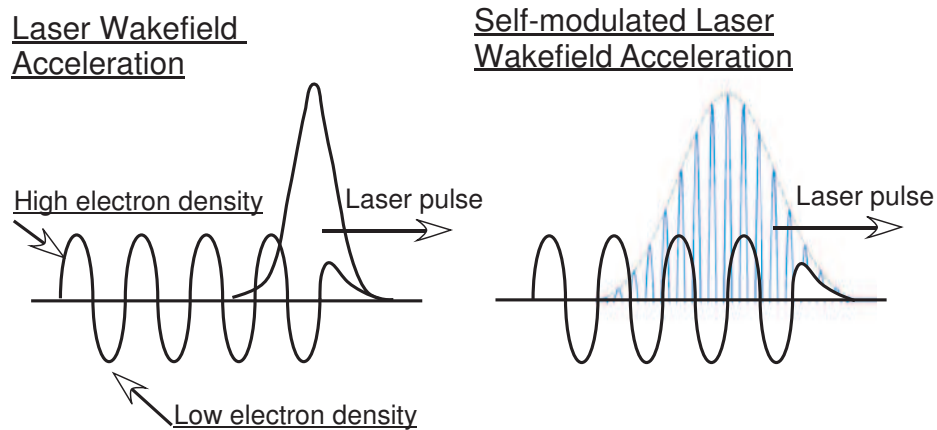
Figure 2.2: (a) Laser wakefield acceleration when the pulse length matches half the plasma wavelength and (b) Self-modulated laser wakefield acceleration (SMLWFA) when the pulse length is longer than the plasma wavelength.

When this condition is satisfied the large amplitude plasma wave is excited and breaks separating electrons from the plasma background. These electrons are injected into or trapped in the laser wakefield and are accelerated with a mechanism similar to

a person surfing an ocean wave. Within the wakefield, the trapped electrons will continue to be accelerated until their velocity exceeds the plasma wave velocity in a process called dephasing. The amplitude E_p of the longitudinal accelerating field can be written down from Poisson's equation given by,

$$\nabla \cdot \mathbf{E}_p = -e \frac{\delta n_e}{\epsilon_0}. \tag{2.30}$$

where the electron plasma wave is described by $\delta n_e / n_e = \delta \sin[k_p(z - vt)]$. Setting the maximum plasma wave amplitude, $\delta = 1$, then the maximum accelerating electric field in the plasma is given by,

$$E_{max} = \frac{e n_e}{\epsilon_o k_p} = \frac{m_e c \omega_p}{e} \cong \sqrt{\frac{n_e}{cm^{-3}}} \quad [V/cm]. \tag{2.31}$$

Thus, for an electron plasma density of 10^{19} cm^{-3} electric fields on the order 300 GV/m are possible; orders of magnitude above conventional rf-linacs which have a limit of ≤ 1 MV/cm due to breakdown of their wall structure. However, as the amplitude of the plasma wave grows nonlinear behavior can cause the waves to lose their sinusoidal profile changing the accelerating fields [22, 23]. Akhiezer and Polovin in [24] calculated the 1D cold wavebreaking limit in the relativistic case given by,

$$E_{WB} = \sqrt{2\gamma_\perp(\gamma_p - 1)} E_{max} \tag{2.32}$$

where γ_p is the relativistic Lorentz factor of the plasma wave. In a cold plasma, the plasma wave approaches the speed of light causing the Lorentz factor to be much greater than 1. Consequently, the above equations show the electric field can be much larger in strength due to relativistic effects. For example, an 800 nm laser pulse propagating through a plasma density of $n_e = 1 \times 10^{19}$ cm^{-3} can drive electric fields

to 1500 GV/m, approximately five times greater than the non-relativistic maximum electric field.

2.2.4 "Bubble" acceleration

As the laser intensity is increased significantly above the wave-breaking limit, the wakefield breaks after just one oscillation forming a single wakefield bubble. This nonlinear regime was first identified by Pukhov and Meyer-ter Vehn [5] and achieved when an ultra-relativistic laser's pulse duration is shorter than the plasma period. Because of the extreme nonlinearities this regime is primarily investigated using 3D particle-in-cell (PIC) simulations to derive scaling rules [5]. As shown in the PIC simulations, for sufficiently short pulses the laser's ponderomotive force creates a bubble-like electron void, hence the name "bubble acceleration". Within the bubble, the background electrons which stream around the growing cavity becoming trapped in the generated longitudinal field, consequently causing the electron "bunch" to be accelerated forward with a narrow energy spread. Theoretical work by Lu *et al.* [25] have shown bubble regime acceleration is optimum for laser pulses with

$$k_p R \approx 2\sqrt{a_0}, \quad \tau \leq \frac{R}{c}, \tag{2.33}$$

where $k_p = w_p/c$ is the wavenumber, R is the focal spot radius, and τ is the pulse duration. It can be shown, from these conditions the laser power must exceed a critical power threshold given by,

$$P > P_{crit} = P_{rel} \approx 0.03 \ TW \ (\frac{\tau_{fs}}{\lambda_{\mu m}})^2, \tag{2.34}$$

where $P_{rel} = m_e^2 c^5/e^2 \approx 8.5$ GW, and τ is in units of fs. The peak electron energy and number of electrons accelerated can be approximated from the laser power and

pulse duration in the following expressions [25],

$$\Delta E \simeq \frac{2}{3}mc^2 \left(\frac{\omega_0}{\omega_p}\right)^2 a_0 \simeq mc^2 \left(\frac{P}{m^2c^5/e^2}\right)^{1/3} \left(\frac{n_c}{n_p}\right)^{2/3} \tag{2.35}$$

$$\Delta E[GeV] \simeq 1.7 \left(\frac{P[TW]}{100}\right)^{1/3} \left(\frac{10^{18}}{n_p[cm^{-3}]}\right)^{2/3} \left(\frac{0.8}{\lambda_0[\mu m]}\right)^{4/3} \tag{2.36}$$

and

$$N \simeq 2.5 \times 10^9 \frac{\lambda_0[\mu m]}{0.8} \sqrt{\frac{P[TW]}{100}} \tag{2.37}$$

where P is the laser power, n_p is the plasma density and λ_0 is the laser wavelength. For a 30 TW and 100 TW laser, assuming a plasma density of 2×10^{19} cm^{-3}, the electron beam energy $E \approx 150$ MeV and 230 MeV respectively.

2.3 Laser interaction with an overdense plasma

Since the development of chirped pulse amplification (CPA) [26] technology multi-terawatt laser systems are being more common. As a result, exciting new fields of research have grown and continue to develop in laser solid interactions. Although CPA systems can achieve high peak powers they inherently produce a poor temporal contrast, defined as the ratio of the low intensity prepulse to the peak intensity. During the interaction of ultra-high intensity laser pulses with solid targets, an unavoidable preplasma is created due to the lasers amplified spontaneous emission (ASE) or prepulse pedestals which exceed the material's ionization threshold. Thus, the peak intensity of the pulse interacts not with a sharp vacuum - solid interface but with a high temperature, highly ionized plasma. As the preplasma expands the electron density is divided into underdense ($\omega_p > \omega_0$) and overdense ($\omega_p \leq \omega_0$) regions connected at the critical surface given by Eqn. 2.26.

2.3.1 Classical resonance absorption

Resonance absorption [27] is an important mechanism through which laser energy can be effectively transferred to the plasma. Near the critical surface, the laser resonantly drives electron plasma waves which can produce energetic electrons that propagate into the overdense plasma. Assuming the p-polarized laser is in the plane of k and some increasing density gradient ∇n_e then there is a component of the electric field along the density gradient ∇n_e. At oblique incidence, the laser will not be able to propagate to the critical surface and will be specularly reflected at a lower density given by,

$$n_{ref}(\theta) = n_c \cos^2 \theta, \qquad (2.38)$$

where θ is the angle of incidence. At the apex of the laser's trajectory the electric field vector, which is in the direction of the density gradient, can tunnel to the critical surface and excite plasma waves. For s-polarized laser light there is no electric field along the density gradient and therefore resonant excitation does not take place. It has been shown [28] that the electrons accelerated though this mechanism have a hot temperature distribution superimposed on an initial Maxwellian background temperature which scales as

$$T_{hot} \approx 10 \ (T_{keV} I_{15} \lambda_{\mu m}^2)^{1/3} \ keV, \qquad (2.39)$$

where T_{keV} is the background temperature in keV, I_{15} is the laser intensity in units of 10^{15} W/cm^2, and $\lambda_{\mu m}$ is the laser wavelength in microns.

Inverse Bremsstrahlung (collisional) absorption is defined as an electron decelerating around a nucleus through the emission of a photon. The electron - ion collision

frequency is given by:

$$\nu_{ei} \simeq 3 \times 10^{-6} \ln(\Lambda) \frac{n_e[cm^{-3}]Z}{T_{eV}^{3/2}} [s^{-1}] \tag{2.40}$$

where n_e is the electron density in cm^{-3}, T is the electron temperature in eV, $\ln(\Lambda)$ is the Coulomb logarithmic factor. The electron - ion collision frequency scales as $T_e^{-3/2}$ and can be neglected in the ultra-high intensity regime.

2.3.2   Brunel heating

As discussed in the previous section, resonance absorption no longer works effectively for sharp density gradients. For plasma density scale lengths less than the laser wavelength, electrons at the critical surface can be efficiently accelerated through a process termed Brunel or vacuum heating [29]. For p-polarized light the laser field pulls electrons from the sharp plasma-vacuum boundary into the vacuum in one half of the laser cycle. When the oscillating field changes directions the electrons are pushed back into the solid where the laser field can no longer penetrate and thus the electrons escape the laser's influence. This is an effective mechanism for the electrons to acquire energy directly from the laser field. Brunel showed for p-polarized, obliquely incident, electromagnetic waves that the fraction of the laser energy absorbed is [30]:

$$f_{Brunel} = \frac{\eta}{2\pi} \frac{v_{osc}^3}{v_L^2 c \cos\theta} \tag{2.41}$$

where η is obtained numerically and is an efficiency factor determining how much of the electron motion is lost to heating the plasma. When $v_{osc}/\omega > L$, where L is the plasma scale length, vacuum heating is the dominate absorption mechanism. A consequence of the vacuum heating vs. resonance absorptions is the different angular

distributions of the accelerated electrons. As the plasma scale length is increased the electron beam shifts from the target normal towards the laser axis [31]. This behavior was also observed in the 2D PIC simulations [31].

2.3.3 $\mathbf{J} \times \mathbf{B}$ heating

$\mathbf{J} \times \mathbf{B}$ heating, as originally discussed by Kruer and Estabrook [32], is associated with the oscillating component of the laser's ponderomotive force, which "pushes" the electrons away from the intensity gradients. The electrons will be accelerated from the laser field with a nearly thermal distribution which is associated to the laser's ponderomotive potential, Φ.

$$\Phi_{pond} = m_e c^2 (\gamma - 1) \tag{2.42}$$

$$= m_e c^2 (\sqrt{1 + a_0^2/2} - 1) \tag{2.43}$$

Where the time averaged relativistic factor for linearly polarized light is given by $\gamma = \sqrt{1 + a_0^2/2}$, and $\gamma = \sqrt{1 + a_0^2}$ for circular polarization. Because the amount of energy the electrons can acquire from this mechanism is the ponderomotive energy, the effective temperature for the hot electrons is given by:

$$T_{pond} \approx 0.511 MeV (\sqrt{1 + a_0^2/2} - 1) \tag{2.44}$$

This is in qualitative agreement with 2-D PIC simulations by Wilks [33] which showed the electrons have a characteristic temperature on the order of ponderomotive potential. The absorption efficiency was shown to be $\sim 10\%$ to 20% for s-polarized and p-polarized light respectively. For laser intensities $I_L = 10^{19}...10^{21}$ W/cm^2 the electron temperature according to Eq. (2.44) is $T_{pond} \approx 0.7...10.5$ MeV respectively.

2.4 Proton acceleration mechanisms

In ultra-high intensity laser solid interactions, protons have been shown exper-
imentally to be accelerated from both the front and/or rear surface [34, 35, 36].
In this section, the two main proton acceleration mechanisms will be described.
First, protons accelerated from the laser focal volume at the target front due to the
lasers ponderomotive induced charge separation. Second, the rear surface accelera-
tion mechanism due to hot electrons propagating though the target which create a
thin electrostatic sheath capable of ionizing and accelerating protons.

2.4.1 Proton acceleration from the front surface

Front surface proton acceleration is a result of the electrostatic fields created
from the ponderomotive expulsion of electrons within the laser's focal volume. The
proton source for metal targets is hydrocarbon contamination (water, oil, etc.) found
on the target surfaces. For hydrogen containing materials such as Mylar or CH, the
proton source can come from contamination or from the bulk material. Protons are
the dominant species accelerated by the electrostatic field because of the high charge
to mass ratio compared to the heavier ion species. Front surface acceleration was
studied by Y. Sentoku *et al.* using 1-D PIC code with a relativistic ($a_0 > 1$) laser
incident upon a μm- scale length preplasma [37]. At the critical surface the electrons
are expelled until the generated electrostatic potential, Φ_e, is approximately equal
to the laser's ponderomotive potential, Φ_{pond} given by

$$\Phi_{el} \approx \Phi_{pond} = m_e c^2 (\gamma - 1), \tag{2.45}$$

where Φ_{pond} and γ are the same as in Eq. (2.43). Assuming a sufficiently long pulse
duration to maintain the charge separation, a 4×10^{20} W/cm^2 intensity laser can

theoretically accelerate protons to about 4.4 MeV. However, this does not occur in experiments because the charge separation is on the order of the laser's skin depth, and PIC simulations in this thesis (chap. 5) show the accelerated protons quickly move away from the electrostatic field and therefore do not acquire the ponderomotive energy.

2.4.2 Target normal sheath acceleration (TNSA)

A second possible acceleration mechanism taking place at the rear surface was first proposed by Wilks *et al.* [38]. The hot electrons accelerated at the critical surface, through one or more of the mechanisms described above, exit the target and leave a quasi-static, target normal electric field, which accelerates the protons (or ions) from the rear surface [39, 40, 35]. Ultimately, the protons move forward reducing the accelerating field which allows the protons to propagate to the detector with constant velocity. Figure 2.3 shows a schematic of TNSA.

Proton acceleration due to the electrostatic fields at the rear of the target can be treated analytically for a sharp boundary plasma expanding into vacuum as shown by Mora [41] and Crow [42]. To do this, one first needs an estimation of the initial electric field, E_0, at the rear surface. As the model suggests only the highest energy (> 1 MeV) electrons will escape thereby charging the target and trapping the lower energy electrons in the Coulomb potential at the rear surface. The rear surface electron density n_e is assumed to have Boltzmann - like distribution given by [43],

$$n_e(z,t) = n_{e0}e^{e\Phi(z,t)/k_B T} \qquad (2.46)$$

where $k_B T$ is the electron temperature, n_{e0} is the initial electron density, and $\Phi(z,t)$ is the electrostatic potential. The electrostatic potential must satisfy Poission's equa-
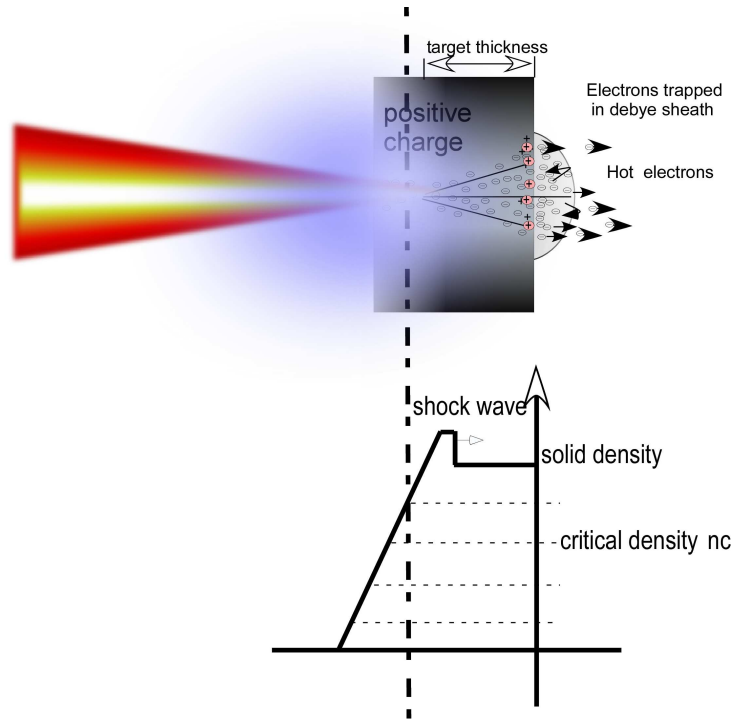
Figure 2.3: Illustration of the TNSA mechanism. The peak laser pulse propagates to the relativistic critical surface and transfers energy into hot electrons. The electrons expand as the propagate through the target becoming trapped at the rear surface, creating a thin electrostatic sheath. The field ionizes atoms and accelerates them normal to the target surface.

tion given by,

$$
\epsilon_0 \frac{\partial^2 \Phi(z,t)}{\partial z^2} =
\begin{cases}
e\big(n_{e0}e^{e\Phi(z,t)/k_B T} - n_i(z,t)\big) & \text{For } x \le 0 \\[2ex]
e\big(n_{e0}e^{e\Phi(z,t)/k_B T}\big) & \text{For } x > 0.
\end{cases}
$$

Assume at $t = 0$ the proton density is a step function equaling the initial electron density, $n_p = n_{e0}$, for $x \le 0$ and $n_p = 0$, for $x > 0$. This implies the target is charge neutral as $x \to -\infty$ and therefore $\Phi(\infty) = 0$. Equation 5.4 can be solved analytically for $x > 0$ giving

$$
\frac{e\Phi(z,t)}{k_B T} = -2\ln\big(1 + \frac{z}{\sqrt{2e_E}\lambda_D}\big) - 1 \tag{2.47}
$$

where $e_E = 2.71828...$ is the natural logarithm. From this the electric field $(E = -\frac{d\Phi}{dz})$

is easily obtained to give a value at the plasma -vacuum and takes the form,

$$E(t = 0) = \sqrt{\frac{2}{e_E} \frac{k_B T n_{e0}}{\varepsilon_0}}. \tag{2.48}$$

Equation 2.48 shows for a step function density profile the electric field strength is determined by the initial electron density and electron temperature. For an electron density $n_{e0} = 10^{21}$ cm^{-3} and a 1 MeV temperature, the peak electric field is about 10^{12} V/m

$$\left[\frac{\partial}{\partial t} + v_i(z, t)\frac{\partial}{\partial t}\right] n_i(z, t) = 0 \tag{2.49}$$

$$\left[\frac{\partial}{\partial t} + v_i(z, t)\frac{\partial}{\partial t}\right] v_i(z, t) = -\frac{e}{m_i} \frac{\partial \Phi(z, t)}{\partial z} \tag{2.50}$$

where $v_i(z, t)$ is the ion velocity. Solving Eqns. (2.50) and (2.50) the proton velocity front can be determined and can be written as, $v_f^2(t) \simeq 2c_s \ln(\tau + \sqrt{1 + \tau^2})$, where $\tau = w_{pi} t / \sqrt{2e_E}$ and w_{pi} is the ion plasma frequency. The maximum proton energy accelerated by the electric field is given by [41]

$$E_{max} = \frac{1}{2}m_i v_f^2 \simeq 2Zk_B T \left[\ln(\tau + \sqrt{1 + \tau^2})\right]^2. \tag{2.51}$$

It is often assumed that the acceleration time is the same as the laser pulse duration τ_L, because that is the time in which the electron temperature at the rear is maintained. Assuming this, the time τ is replaced with τ_L. According to this simple model the obtained ion spectrum for the highest energy protons is

$$\frac{dN}{dE} = \frac{n_i c_s t}{\sqrt{2Zk_B TE}} \exp\left(-\sqrt{\frac{eE}{Zk_B T}}\right) \tag{2.52}$$

where Z is the ion charge, E is the proton energy, and $c_s = \sqrt{Zk_B T/m_i}$ is the ion sound speed [41]. To apply this spectrum to an experimental situation the spectrum

will only extend out to the maximum proton energy front and does not follow the exponential decay indefinitely. The above model is intuitive but may oversimplify the interaction conditions causing the calculated values to deviate from experimental results. The model assumes an isothermal process which does not hold true for a highly non-equilibrium plasma. The numerical values can vary by 2 - 10 times depending on the electron temperature, number of electrons trapped at the rear surface and the acceleration time. Although Mora et $al.$ [41] assumed the laser pulse duration, Fuchs et $al.$ [44] found the experimental results could be fit using this model when the acceleration time was $1.3\tau_L$ ($\sim$ 104 fs) for laser intensities ranging from $2 - 6 \times 10^{19}$ W/cm^2. Passoni et $al.$ [45] modified the model be assuming the rear electrostatic field was generated by two electron populations with a hot and cold Boltzmann distribution. Their work shows the peak electric field strength varies depending on the ratio of the hot and cold distributions but is predominately dominated by the hot electrons. The two temperature model was shown to be more efficient and thus give a higher peak electric field. It is important to emphasize that the electron density, and acceleration time cannot be measured directly and the model may begin to break down as the laser intensity increases.

CHAPTER III

The Ultra-Intense, Ultra-high Contrast Hercules Laser System

HERCULES is an acronym for High Energy Repetitive CUos LasEr System. This chapter describes the laser system and the unique characteristics of ultrahigh intensity and ultra-high contrast which it possesses. Hercules is a ~ 40 TW laser which delivers approximately 1.1 Joule, $\tau = 30$ fs pulses with a peak wavelength of $\lambda = 800$ nm. The ASE contrast ratio, defined as the pedestal-to-peak intensity ratio, is $\sim 10^{-11}$ a few hundred ps before the peak pulse. In this chapter a general description of the laser system is given, followed by details of adaptive optics and the implemented front end pulse cleaning technique (XPW), which generated a record high 10^{-11} ASE contrast, necessary to perform the solid target experiments [46].

3.1   The HERCULES laser system

The Hercules laser system is based on chirped pulse amplification (CPA) [26]. CPA was invented by Gérard Mourou at the University of Rochester during the mid 1980's. The technique takes an ultrashort laser pulse, which has a peak power capable of damaging the gain medium, and stretches it in time with a pair of gratings. This causes the low frequency component of the laser to travel a shorter distance

than the high frequency component giving the pulse a positive chirp, i.e. the high frequency lags the low frequency. Depending on the laser system the pulse duration is increased by a factor of 10^3 to 10^5 consequently decreasing the intensity below the gain medium's damage threshold. After the stretched pulse is safely amplified, by a series of gain media, it is recompressed in time creating peak powers on the order of TW to PW.
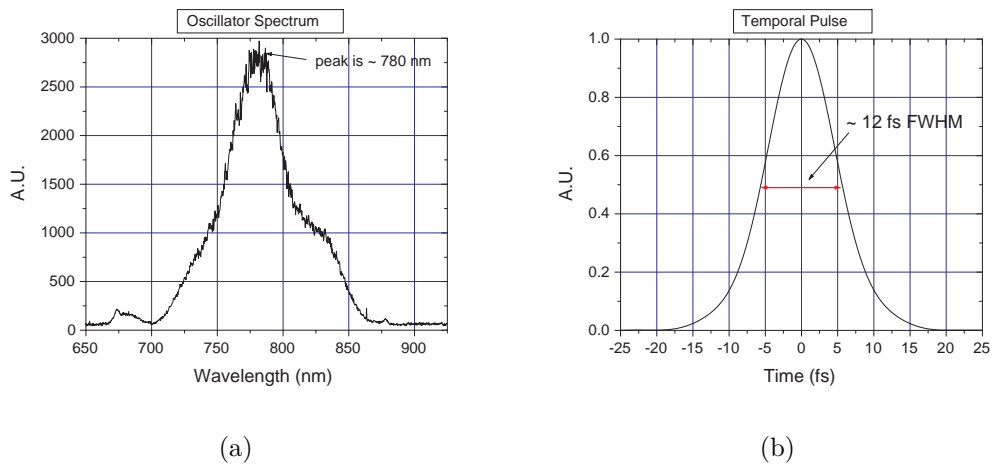
Figure 3.1: Oscillator spectrum (a) and corresponding temporal envelope (b).

The laser system starts with a Titanium:Sapphire (Ti:Sa) oscillator, which delivers 10 nJ, $\sim$ 12 fs duration pulses at an 80 MHz repetition rate. A general schematic of Hercules is given in Fig. 3.2. Ti:sapphire lasers are popular in scientific research because of the broad gain bandwidth the material can support (approximately 200 nm FWHM) allowing for the generation of ultrashort pulses. The output spectrum along with the calculated Fourier transform is shown in Fig. 3.1 showing a 12 fs pulse. The oscillator is Kerr-lens mode-locked [47, 48] which is a technique based on the non-uniform power density distribution in the Gaussian beam causing the refractive index to be maximum in the beam center and a minimum at the beam edge. Details of Kerr-lens mode-locking can be found in Ref [49, 50]. Hercules uses a

FemtoLasers/GmbH Femtosource oscillator which is pumped by a frequency doubled Nd:YAG laser from Spectra-Physics (Millenia). In order to decrease the repetition rate to 10 Hz a fast Pockels cell and polarizing beam splitter are placed after the oscillator. Pockels cells use an electro-optic effect which produces birefringence in the optical medium due to an electric field. This induces a change in the laser polarization and allows it to be used as a temporal switch.

The next step in the laser system is the temporal pulse cleaner which improves the laser contrast by approximately 3 orders of magnitude. However, in order for the cleaner to be effective, a pre-amplifier is inserted to amplify the pulses from $\sim$ nJ energy up to $\sim \mu$J. The pulse cleaner is discussed in greater detail in section 3.3.

Before the pulses can be further amplified they must be stretched in time from 12 fs to about 350 ps ($\tau_{stretched} \sim 3 \times 10^4 \ \tau$) in order to prevent damaging optical components. This is done using an all-reflective on-axis pulse stretcher introduced by Banks *et al.* [51]. The design is simple to align and introduces some aberrations affecting the fourth-order phase term, but this may be used to compensate for material dispersion. The positive dispersion introduced by the stretcher will be later compensated by the compressor system.

Next, is the first major amplification stage called the *regenerative amplifier* or *regen* for short. There are several advantages to regen amplifiers [52] as compared to multi-pass amplifiers. Regen amplifier typically provide diffraction limited beam quality where multi-pass amps are used to extract energy more efficiently. The main source of prepulse in the laser system is, leakage from the round trips in the regen amplifer, amplified spontaneous emission (ASE), and high order phase distortions due to bandwidth limitations and/or stretcher and compressor errors. Long regen cavities reduce the opening solid angle which decreases the ASE thus providing a
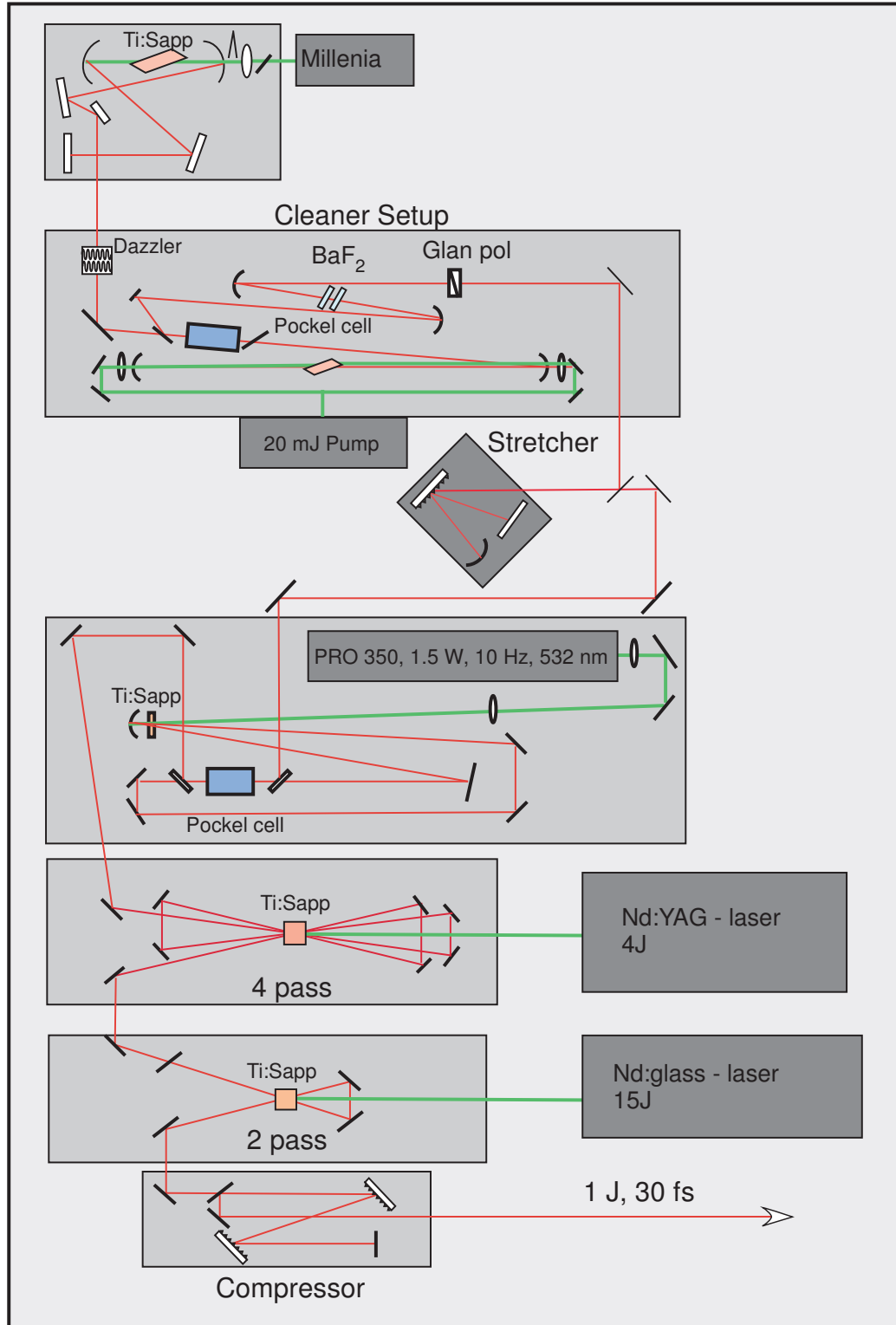
Figure 3.2: Schematic of the HERCULES laser system.

better contrast ratio. The regen is followed by a second Pockels cell which is used to cut the ASE approximately 5 ns before the peak pulse.

The next amplification stage is a *4-pass "butterfly"* amplifier which increases the pulse energy to about 300 mJ (after compression). The 4-pass amplifier is cryogenically cooled using a cryopump (under vacuum) to $-180\ ^{\circ}C$ to prevent thermal lensing. The 4-pass amplifier is pumped with a frequency doubled Nd:YAG laser. The pump laser is capable of outputting 4 J, but typically runs at 2.2 J due to parasitic generation in the Ti:sapp crystal. This stage brings the laser power to $\sim$10 TW (after compression). After the 4-pass amplifier there is a similar 2-pass amplification stage. Here the Ti:sapp crystal is pumped with a Nd:glass laser at 0.1 Hz which limits the repetition rate of the entire laser system. After the amplifier the beam energy is brought to $\sim$ 2.1 J which is then sent to the compressor chamber and from there to the experiment. The transmission efficiency of the compressor system is 55% giving approximately 1 Joule of energy on target or 30 TW of power.

3.2 Adaptive optics

As the development of high intensity lasers and table-top particle accelerators continues to progress experimental results and the verification of models is critical in understanding new regimes of particle acceleration. Current table-top systems have several advantages over large scale facilities, such as lower size, lower cost, and high repetition rate. However, in order to achieve ultra-high laser intensities great care must be taken to focus the laser into the smallest possible spot size. For an ideal top-hat spatial profile with a plane wavefront, the radius r of the first Airy disk in the focal plane is given by [53]

$$r \approx 1.22 \frac{f}{D} \lambda \approx 2 \mu m \tag{3.1}$$

where f is the focal length, D is the beam diameter, and λ is the laser wavelength and is about 2μm for an f/2 parabola. 84% of an ideal top-hat pulse is contained in the first Airy disk. Assuming a 1 Joule, 30 fs pulse with an ideal spot size it will have an average laser intensity of

$$I_{avg} = \frac{E}{\tau \pi r^2} \approx \frac{0.84 J}{30 fs \ \pi (2\mu m)^2} \approx 2.2 \times 10^{20} \ W/cm^2. \tag{3.2}$$

within the first Airy disk. The peak intensity is about 4.38 times higher than the average giving about 1×10^{21} W/cm^2 for the best case scenario. During the real experiment there are several sources of wavefront aberrations. For example, imperfections of the optical components throughout the laser system and thermal effects induced by the pump laser in the amplifiers. Shot-to-shot wavefront aberrations from the laser beam were measured to have an root mean squared (rms) value of 0.06 λ, giving the lower limit of achievable correction and demonstrating the wavefront distortions coming from the laser are "static." The critical wavefront aberration in the experiment is astigmatism from the short focal length parabola, which can decrease the laser intensity by a factor of 10. Therefore, wavefront correction is necessity in order to achieve ultrahigh intensities and was a unique experimental technique used in this thesis for the solid target experiments.

A Shack-Hartmann wavefront sensor was used during the solid target experiments to measure the shape of the laser wavefront. The detector consists of a lenslet array and a camera to record the pattern of images formed by the lenslets in the array. The local slope is directly proportional to the focal spot deviation on the detector screen [54]. After the wavefront is measured, it is fed to a computer and is used to guide the
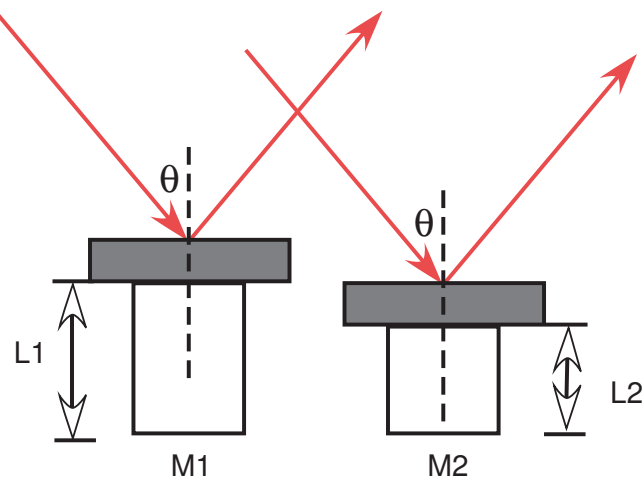
Figure 3.3: Schematic of the deformable mirror (DM). The motors behind the mirrors surface shift causing relative phase differences within the laser's wavefront and is used to create a uniform wavefront.

deformable mirror. The deformable mirror (DM) has an array of piezoelectric motors behind its surface which slightly deforms the mirror thus changing the reflecting beams wavefront. A simple schematic of the deformable mirror's actuators is shown in Fig. 3.3. For simplicity assume a plane wave of monochromatic light reflects off the deformable mirror at some angle θ. The vertical difference between the two mirrors is $L1 - L2 = \Delta L$. This results in a relative phase difference between beam 1 and beam 2 given by $\delta = \dfrac{4\pi}{\lambda}\Delta L\cos(\theta)$. As the DM motors deform the mirrors surface, the Shack-Hartmann wavefront sensor monitors the change in the wavefront. A feedback loop is created and is used to create a uniform wavefront.

Figure 3.4 shows the uncorrected wavefront measurement with the DM off and the corrected wavefront with the DM on. Without the DM the wavefront has an rms. value of 0.73 λ and a peak to valley (P.V.) ratio of 3.62 λ. This is a typical example of the laser wavefront in the focal plane after the laser pulse propagates through all of the components of the experimental setup. As a note, the P.V. ratio isn't typically as significant as the rms. in this technique. As the DM corrected
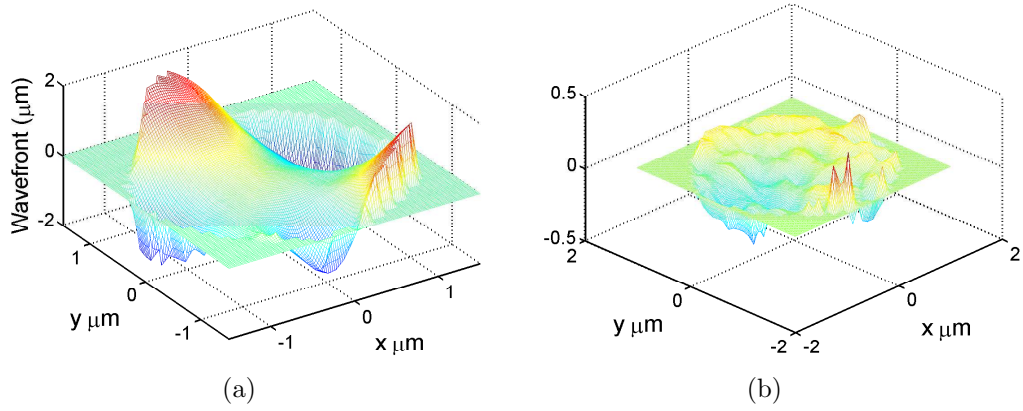
Figure 3.4: Wavefronts of the regenerative amplifier beam focused with an f/2 off-axis parabola: (a) before correction with an r.m.s. value of 0.73 λ and (b) after DM correction with an r.m.s. value 0.07 λ.

wavefront shows, there are two small peaks on the outside edge of the beam causing the P.V. value to single out such effects. Because these wavefront distortions are at the edge of the mirror they are often not correctable and do not significantly affect the final spot size. On the other hand, the DM corrected wavefront shown in Fig. 3.4(b) has an rms. of 0.07 λ and P.V. of 0.81 λ. The deformable mirror converted the rms. wavefront value from about 1λ to less than $\lambda/10$.
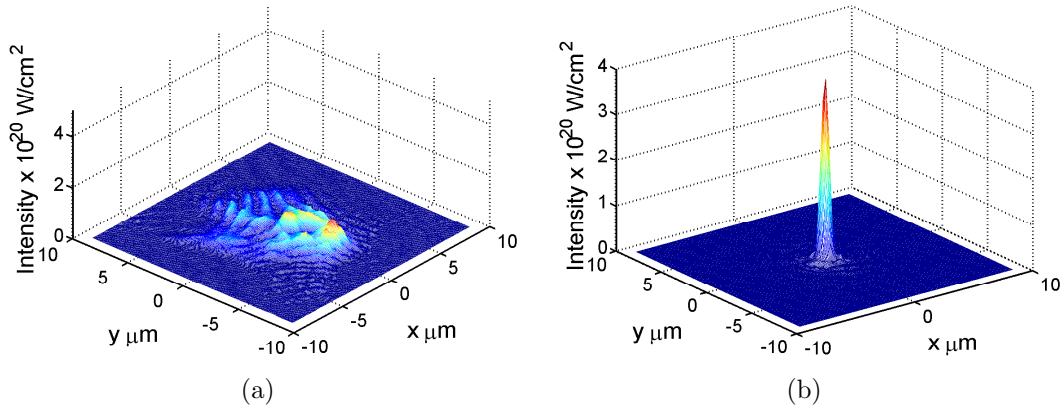
Figure 3.5: Laser focal spot of the regenerative amplifier beam focused with an f/2 off-axis parabola: (a) before wavefront correction (b) after wavefront correction.

The corresponding measured focal spots are shown in Fig. 3.5. The difference

in the peak intensity of the uncorrected (Fig. 3.5(a)) regenerative amplifier beam vs. the DM corrected beam (Fig. 3.5(b)) is approximately 4 times. It is clear from Fig. 3.5 that for the uncorrected wavefront most of the amount of energy lost is pushed out into the wings the focal spot. Apart from a decrease in laser intensity, a poor focus can complicate the dynamics of laser-plasma interactions. A poor focus creates intensity "hot spots" which may cause a non-uniform preplasma expansion at the target surface. A factor of 4 increase in laser intensity may be enough to push through a threshold in high field science. Additional correction of the wavefront at high power is not required because there are no thermal effects in the booster amplifiers due to cryogenic and water cooling of the 10 TW and 30 TW amplifiers respectively. This was experimentally tested by measuring the wavefront distortions with the 10 TW and 30 TW amplifiers engaged and showed the wavefront aberrations were below the shot-to-shot fluctuation.

3.3 Cross polarized wave generation - XPW

To achieve high energy protons from the interaction of a high intensity lasers with submicron targets requires both a high laser intensity and sufficient temporal laser contrast, defined as the ratio between the peak intensity and the amplified spontaneous emission (ASE). Inherent to high intensity laser systems is the generation of ASE, which, when above the material damage threshold, can generate a preplasma and terminate proton beam generation. Plotted in Fig. 3.6 is the laser intensity vs. time for an ideal Gaussian shape and a typical pulse with a 10^{-11} nanosecond contrast and about 10^{-6} at 5 picoseconds. The Hercules laser can deliver a 50 TW peak power, 30 fs laser pulse into a 0.8 μm spot size, giving a focused intensity of $\backsim 10^{22}$ W/cm^2 [55]. Such high intensity lasers require a contrast ratio of 10^{-11} to

avoid material breakdown and preplasma formation.
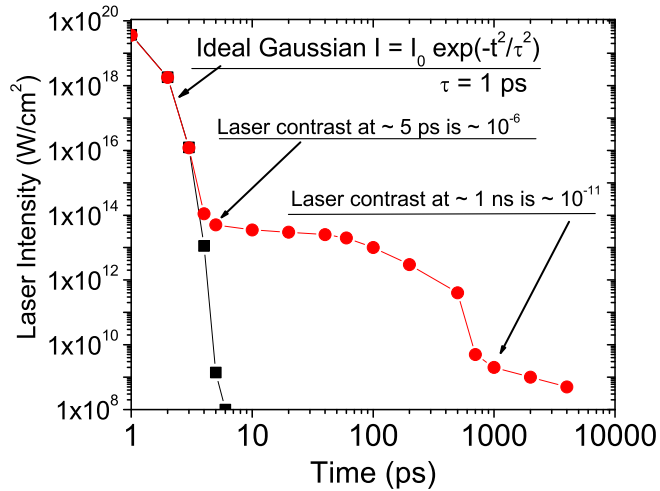
Figure 3.6: Laser intensity as a function of time for two different temporal pulse profiles. The black squares show an ideal Gaussian profile with a 1 ps FWHM duration. And the red circles plot a typical laser profile with varying degrees of laser contrast at different times.

Several techniques have been introduced to increase the laser contrast such as a saturable absorber [56], fast Pockels cells or plasma mirrors [57]. Saturable absorbers are convenient to align but typically increase the contrast by 1-2 orders which is inadequate for ultrahigh intensity lasers. Fast Pockels cells are limited to about 300 ps before the peak pulse (they are used on the stretched pulse before compression causing 300 ps ASE after compression) and plasma mirrors are a single shot technique and has to be replenished after every shot.

As part of this thesis, an alternative pulse cleaning technique based on Cross Polarized Wave (XPW) generation in BaF_2 crystals [58] which was implemented at the front end of the Hercules laser [46]. XPW generation is an intensity dependent process where a portion of the linearly polarized input amplitude is converted into an orthogonally polarized component. After the BaF_2 crystal the laser is passed

through a Glan polarizer, which is used to separate the unchanged low intensity portion from the high intensity peak. This allows only the high intensity portion of the laser to move into the amplification stage while the low intensity prepulses are rejected thus increasing the contrast ratio (Fig. 3.7). Cross Polarized Wave (XPW) generation has been demonstrated on the Hercules laser generating a total contrast ratio of 10^{-11}. The Hercules laser without XPW in place has a contrast ratio of 10^{-8}, showing XPW generates three orders of magnitude enhancement.
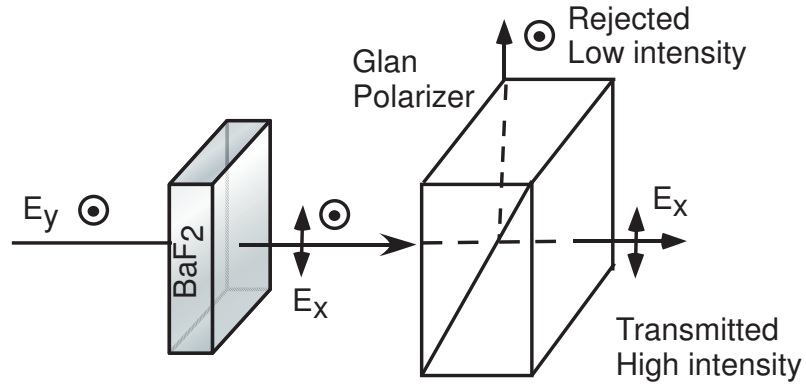
Figure 3.7: Schematic of cross polarized wave generation (XPW)

To gain insight into XPW generation it is instructive to write down a simple model describing the evolution of the fundamental wave amplitude (A) and the cross polarized generated wave amplitude (B). The set of equations below are used assuming $|B| \ll |A|$ and no pump depletion which are reasonable assumptions because the conversion efficiency is below 10%. This assumption allows one to neglect cross-phase modulation of wave A caused by wave B and self-phase modulation of wave B. The following set of equations are used to calculate the XPW efficiency,

$$\frac{dA}{dz} = i\gamma_{||} |A|^2 A, \quad \frac{dB}{dz} = i\gamma_{\perp} |A|^2 A \tag{3.3}$$

where $\gamma_{||} = \gamma_0[1 - (\sigma/2)\sin^2(2\beta)]$, $\gamma_{\perp} = -\gamma_o(\sigma/4)\sin(4\beta)$, $\gamma_0 = (6\pi/8\lambda n)\chi_{xxxx}^{(3)}$, σ is

the anisotropy of the $\chi^{(3)}$ tensor given by $\sigma = (\chi_{xxxx}^{(3)} - 2\chi_{xyyx}^{(3)} - \chi_{xxyy}^{(3)})$ and β is the angle between the input polarization direction and the [100] axis of the crystal. A more detailed analysis can be found in Ref [58, 59]. The solution to these equations with the initial conditions $A(0) = A_0$ and $B(0) = 0$, where $|A_0|^2 = 2I_0/c\varepsilon_0 n$ and I_0 is the input intensity, is

$$A = A_0 \exp(i\gamma_{||} A_0^2 L), \tag{3.4}$$

$$B = A_0(\gamma_\perp/\gamma_{||})[\exp(i\gamma_{||} A_0^2 L) - 1]. \tag{3.5}$$

The theoretical conversion efficiency is defined as the square of the ratio of the input field A_0 and the orthogonally polarized component B given by

$$\eta = \frac{I_{out}}{I_{in}} = \left|\frac{B}{A_0}\right|^2 = \left(\frac{\gamma_\perp}{\gamma_{||}}\right) \sin^2(\gamma_{||} |A_0|^2 L/2). \tag{3.6}$$

As shown in Ref. [60] the anisotropy of the $\chi^{(3)}$ tensor for BaF$_2$ is $\sigma = $ -1.2, and $\chi_{xxxx}^{(3)}$ is around $1.59 \times 10^{-22} m^2 V^{-2}$ causing $\gamma_\perp$ to be very small. Assuming $\left|\gamma_{||} A_0^2 L\right| \ll 1$ then Eqn.3.6 becomes $\eta \sim |\gamma_\perp|^2 A_0^4 L^2$, showing that the conversion efficiency depends on the square of the laser intensity. Therefore, early experiments by Jullien *et al.* [58] required milli-Joule energy input pulses to get about 10% conversion efficiency. Such high energy is not easily obtainable at the front end of CPA laser systems. This presents an major barrier and therefore a separate CPA system would be necessary just to generate the input pulse for XPW.

Eqn. 3.6 shows the periodic nature of the conversion efficiency, η, which is dependant on the input intensity and crystal length. The oscillating function prevents the growth of the XPW along the whole length of the BaF$_2$ crystal due to saturation. In other words, increasing the crystal length will not increase the efficiency

and increasing the input intensity above 10^{12} W/cm^2 will damage the crystal. Also, the conversion efficiency of the peak intensity into the orthogonally polarized output component depends on the input polarization angle with respect to the [100] axis of the crystal and may deviate as the pulse propagates through the material thus decreasing the nonlinear transmission. Lastly, direct pulse amplification after the oscillator can increase the laser pulse energy to several mirco-Joules but not to milli-Joules. In other words, a single BaF$_2$ crystal is simply not compatible with the input conditions of a CPA laser.

Therefore, to improve the conversion efficiency, two BaF$_2$ crystals are placed in series, rotating the second crystal's axes to compensate for the polarization rotation in the first crystal. This allowed the measured transmission efficiency to increase to 25%. In order to achieve a 10^{-11} contrast 50 TW pulse, two developments must be realized. First, XPW generation was demonstrated using micro-Joule pulses, which are directly amplified from the oscillator output incident upon two BaF$_2$ crystals. A programmable acousto-optical filter (Dazzler) was used to compensate for amplifier dispersion in order to preserve the short pulse duration (12 fs). The combination of a short pulse duration with micro-Joule energy allowed for sufficient focused intensity to drive XPW generation and consequently reduce the ASE [46]. Second, the Hercules laser system uses a long cavity ring-resonator regenerative amplifier [52], allowing for a contrast level of 10^{-8} with nano-Joule pulses injected into the regenerative amplifier [61]. However, after direct amplification to drive XPW, one can further reduce the ASE by injecting micro-Joule energy pulses, rather than of nano-Joule, into the regenerative cavity, allowing for a lower pump fluence of the regenerative amplifier to achieve the same energy output.

The contrast was measured at the laser output using a third-order autocorrelator
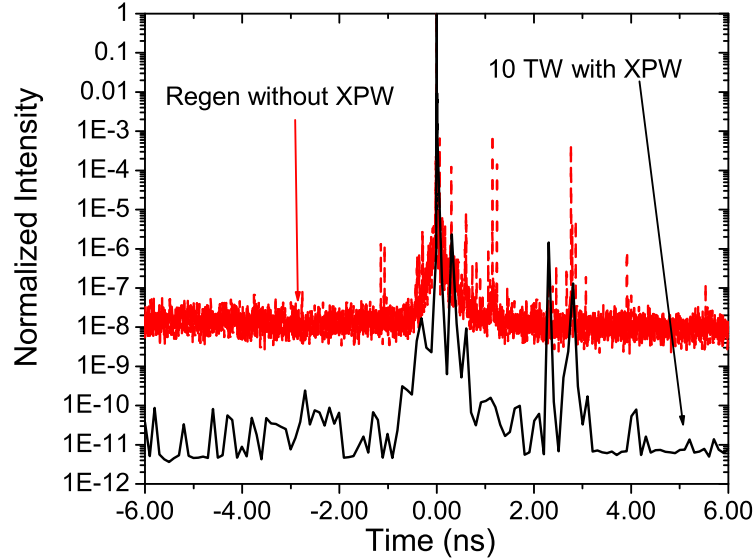
Figure 3.8: Third-order autocorrelation without (top red curve - regenerative amplifier only) and with (bottom black curve - 10 TW power) the XPW cleaner.

with and without the cleaner in place (Fig. 3.8). The top red curve represents the contrast measurement of 5×10^{-7} without the XPW cleaner, and with only the regenerative amplifier engaged, giving an output energy of 10 mJ. A contrast measurement of 10^{-11} with the XPW cleaner in place is shown with a single booster amplifier engaged (bottom black curve) giving 10 TW output power. Additionally, several points were plotted with both booster amplifiers engaged, outputting 50 TW pulse power. The resulting contrast ratio of 10^{-11} demonstrates that the XPW cleaner improves the laser ASE contrast by at least 3 orders of magnitude.

CHAPTER IV

Photonuclear Processes with Quasi-Monoenergetic Electron Beams from Laser Wakefields

Laser driven plasma wave electron acceleration was first proposed by Tajima and Dawson [20]. An ultrahigh intensity, short pulse pump laser, propagating through the underdense plasma, excites a plasma wave traveling with a phase velocity equal to the pump lasers group velocity. This new breed of accelerators can support large acceleration gradients, on the order of several hundred GV/m, due to the plasmas immunity to electrical breakdown. Wave-breaking governs the maximum electrostatic field the plasma wave can support and causes electrons, which are no longer a part of the plasma wave, to become trapped and continuously accelerated by the wave. Several groups have produced quasi-monoenergetic electron beams with energy ranging between 10-170 MeV using short pulse TW laser systems [1, 2, 3].

This chapter reports on the production of quasi-monoenergetic electron beams in the energy range of 100-300 MeV with a 40 TW laser [62, 4], and on the application of quasi-monoenergetic electron beams for the efficient initiation of photonuclear reactions of ^{12}C(γ,n)^{11}C, ^{63}Cu(γ,n)^{62}Cu, and ^{238}U(γ,fission)^{134}I and ^{92}Sr [63]. From our results and comparison with Monte Carlo modeling of the electromagnetic cascades produced, we infer characteristics of the high energy electrons striking the targets,

including their total number per laser pulse. As described further below, we have obtained between 10 and 100 times the photonuclear yields per Joule of laser energy compared to earlier experiments.

4.1 Experimental setup

The experiment was performed using the Hercules laser system. The 30 fs, 800 nm, 40 TW laser pulse was focused to a 17 μm FWHM spot size using a 1 meter focal length, F/13.3 parabolic mirror giving a peak intensity of 10^{19} W/cm^2. Approximately 50% of the laser energy was within the FWHM region. The laser energy was measured on every shot using a calibrated CCD camera which showed a $\pm 10\%$ shot-to-shot energy fluctuation. The laser was focused on the front edge of a 2 mm wide supersonic, cylindrical He gas jet. A 90-10 percent laser beam splitter was inserted before the compressor chamber, separating the laser pulse into pump and probe beams. The transverse probe beam was sent to a modified Mach-Zehnder interferometer, where Abel inversion of the phase information was used to calculate the electron density during the interaction. Interferometric analysis showed that the 2 mm gas jet produced a 1.5 mm flat top gas profile, where the gas density decreased by 50% over a 300 μm range on both sides.

The spatial distribution and position of the electron beam was detected using a LANEX phosphor screen located 80 cm behind the gas jet, imaged onto a 12-bit Cool Snap CCD camera. Thin aluminum foil protected the LANEX screen from transmitted and scattered laser light within the interaction chamber. An integrating current transformer (ICT) was used to measure the total electron beam charge exiting the gas target in the forward direction, with a maximum charge of about 0.5 nC for plasma electron densities ranging between 2×10^{19} cm^{-3} to 4×10^{19} cm^{-3}, however,

as shown below the ICT measurements may over estimate the charge. The laser was fired approximately once every 60 seconds. The repetition rate was limited by the speed with which the vacuum pumping system could re-evacuate the target chamber to 10^{-4} Torr.

4.2 Experimental results

A narrow beam of electrons with a 10 mrad divergence was observed using a background electron density between 1.5×10^{19} and 3×10^{19} cm^{-3} as shown in Fig. 4.1. As the background electron density increases larger diameter electron beams with more complex structure appear (Fig. 4.1b) and periodically lead to electron beam breakup. The electron beam pointing stability strongly depends on the plasma electron density and showed ± 10 mrad (Fig. 4.1c) at densities between 1.5×10^{19} and 1.8×10^{19} cm^{-3}. For plasma electron densities below 1.5×10^{19} cm^{-3} no electron beams were detected. The higher plasma density leads to stronger nonlinearities and gives more curvature to the wakefield [64], which can cause larger beam divergence and angular fluctuation.

The forward emitted electron momentum distribution was measured using the LANEX screen and a 5 cm thick 0.24 Tesla dipole magnetic spectrometer located 17 cm behind the gas jet. A 0.8 mm thick wedged lead slit was placed before the magnet to increase the energy spectral resolution by filtering laser beam shot-to-shot fluctuations. The angular width of the slit was 5 mrad, which was two times smaller than the narrowest electron beam observed in the experiment. Due to the nonlinear dispersion of the dipole magnet and the electron beams shot-to-shot fluctuations and angular divergence, the energy resolution was ± 15 MeV for 150 MeV electrons, and ± 50 MeV for 350 MeV electrons. The quasi-monoenergetic nature of the electron
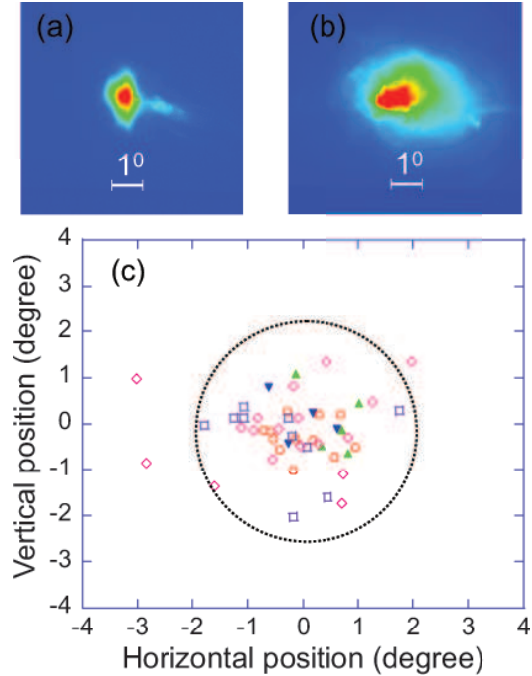
Figure 4.1: Spatial distribution of the electron beam imaged onto a LANEX screen for a given electron density (a) 2.0×10^{19} cm^{-3}, (b) 3.5×10^{19} cm^{-3}, (c) Beam pointing stability from electron densities between 1.5×10^{19} cm^{-3} and 3.5×10^{19} cm^{-3}. Varying electron densities are given by the corresponding symbol: Inverse triangles - 1.5×10^{19} cm^{-3}, triangles - 1.8×10^{19} cm^{-3}, circles - 2.0×10^{19} cm^{-3}, squares - 3.0×10^{19} cm^{-3}, diamonds - 3.5×10^{19} cm^{-3}. The large dotted circle represents the laser diameter on the LANEX screen.

beam is shown in Fig. 4.2 where the majority of laser shots exhibited one peak in the energy spectrum.

The maximum electron energy showed a strong dependence on the backing electron density in the gas jet as shown in Fig. 4.3. For plasma densities ranging between 2×10^{19} to 4×10^{19} cm^{-3} the maximum electron energy was shown to be lower ranging from 70 to 160 MeV. For lower plasma density below 2×10^{19} cm^{-3} the electron beam energy was consistently higher with a maximum electron energy of 320 ± 50 MeV. As the backing pressure of the gas jet is reduced, the integrity of the generated electron beam exhibits a more stable angular divergence with improved emittance, however the electron beams total charge is significantly reduced.
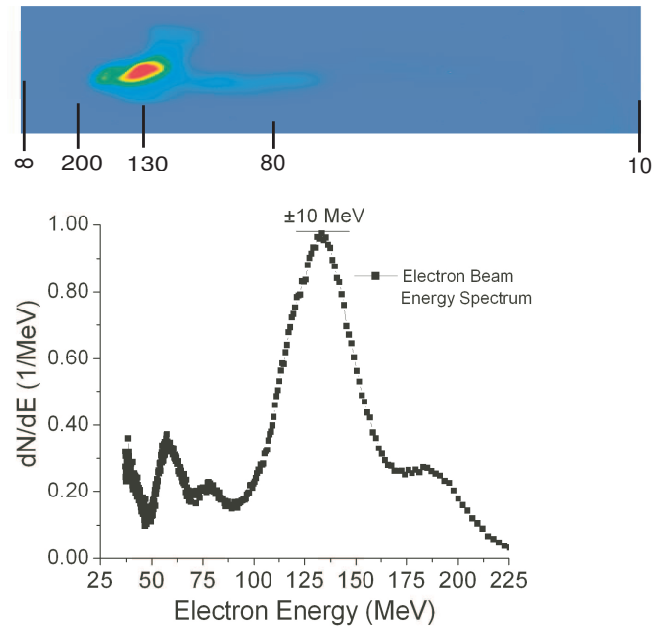
Figure 4.2: Lineout of the electron energy spectrum for plasma density 2.5×10^{19} cm^{-3} showing ~130 MeV electron energy.
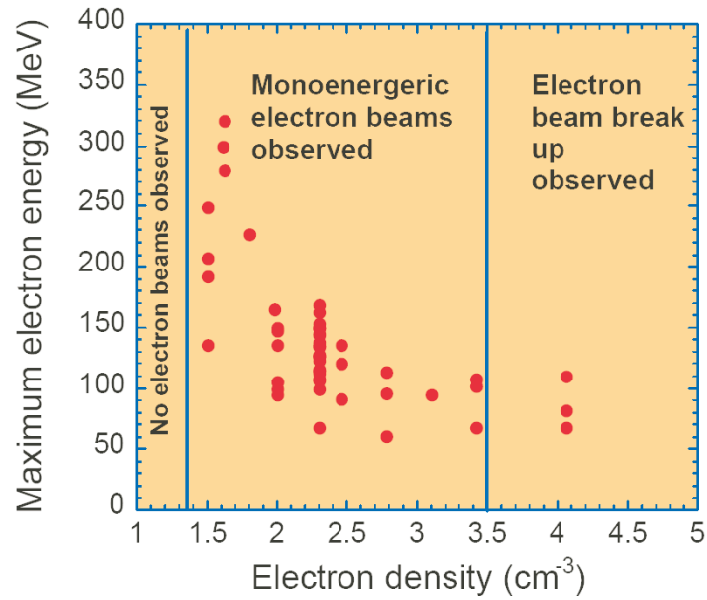
Figure 4.3: The maximum electron energy as a function of plasma density.

After tuning for optimum electron beam production with the highest bunch charge, a 3 mm thick, 11 mm diameter tantalum metal slab was placed ∼13 cm downstream from the gas nozzle. This converter target was used to generate energetic bremsstrahlung photons with energies up to the maximum electron energy (i.e., ∼150 MeV). The bremsstrahlung photons were then intercepted immediately by sample isotope production targets of carbon or copper. A natural uranium target was also exposed without the tantalum; the high-Z uranium being its own effective bremsstrahlung converter. A schematic is shown in fig. 4.4.
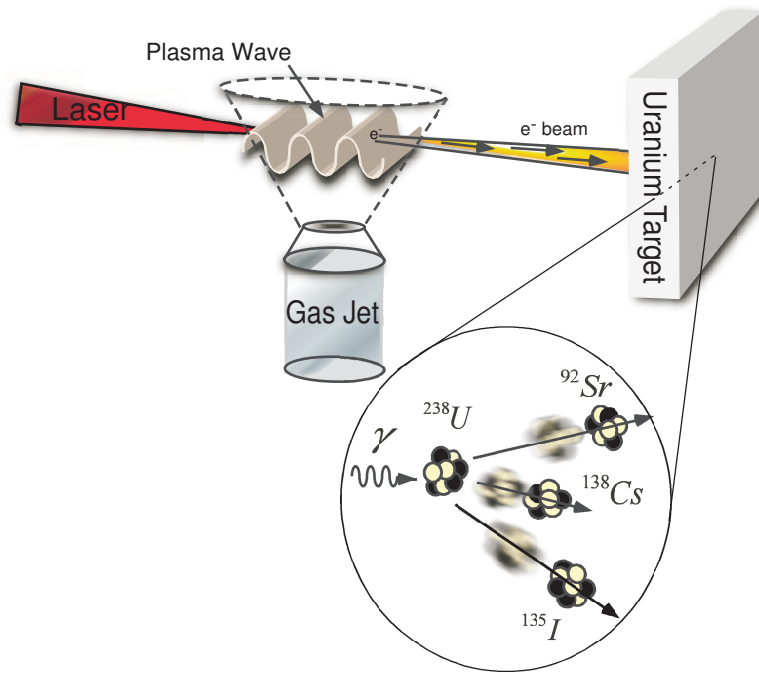
Figure 4.4: Schematic of a laser plasma interaction. The high intensity laser propagates through the gas target accelerating electrons to several hundred MeV. The generated bremmsstrahlung is used to initiate photo-nuclear reactions.

The resulting photonuclear processes occurring in the exposed targets were identified and measured via standard calibrated γ-spectroscopy techniques. Because the efficiency of the bremsstrahlung process increases dramatically with increasing nuclear charge, the Ta sheet acts as a more efficient γ-ray converter than the C and

Cu blocks alone. The Ta thickness was chosen to optimize bremsstrahlung above the ^{12}C(γ,n)^{11}C threshold ($\sim$20 MeV) with minimum radiation self absorption.

The carbon nuclear excitation measurements used a 16.7 mm thick block of ^{12}C, (density = 2.25 g/cm^3) placed 150 mm downstream from the center of the gas jet, immediately behind the Ta convertor target [63]. The high energy photons produced primarily in the Ta converter induced (γ,n) reactions in the carbon target. The target thickness was chosen to optimize absorption of the incident γ-rays while limiting absorption of subsequently emitted 0.511 MeV positron annihilation photons from the beta decay of the product ^{11}C atoms.

Buildup of photo-excited ^{11}C activity in the target was constrained because of the competition between the rates of ^{11}C production and its radioactive decay. For a given constant laser pulse repetition rate only a limited number of shots will produce a significant growth in the observed activity of the isotope target, since immediately after each laser shot, the number of ^{11}C nuclei produced begins to decay. To efficiently balance exposure and counting times, the laser was fired approximately once per minute for a total time of about one half-life of ^{11}C (1225 seconds). After accumulating shots for twenty minutes, the irradiated C target was removed from the chamber, transported to a lead shielded counting area, and placed in front of a lithium-drifted germanium γ-ray detector. There was a thirteen minute delay between the time of the last laser shot and the start of γ-ray counting due to the target removal and relocation time. Counting was done "off-line" in order to suppress substantial electronic backgrounds from the electromagnetic pulse noise occurring during subsequent continuing laser shots.

The γ-ray detector used was a liquid nitrogen cooled, ORTEC GAMMX Ge(Li) detector with a thin (0.5 mm) Be window. The analog output signal was amplified

and digitized using standard pulse counting electronics; the final pulse height spectral data were stored on a PC as a function of clock time for later analysis. The sample being counted and the Ge(Li) detector head were placed inside a 5 cm thick Pb shield enclosure reducing background counts to less than 10% of the unshielded value. The spectral energy scale and detector efficiency were calibrated immediately before γ-ray counting using ^{22}Na (511 and 1274.5 keV) and ^{60}Co (1173.2 and 1332.5 keV) radioisotope standard sources. Background data were established by accumulating calibrated spectra without any radioactive sample present. The background consisted of a number of lines from expected decays present in typical concrete found in buildings. Near 0.511 MeV, about 0.1 background counts per second were recorded. Count rate dependent dead time corrections were also made, but these never exceeded more than a few percent. Measurements were also performed in a similar manner for Cu and for natural U as described below.

4.3 Photonuclear activation

The γ-spectrum from the activated C sample was measured for 110 minutes, or a little over five half-lives. The accumulated spectrum was stored on a PC, with intermediate spectra being stored every four minutes during the first two half-lives and then less frequently afterwards. This allowed the ^{11}C decay curve to be determined by the rate of 0.511 MeV photon counting as a function of time. Figure 4.5 shows the background-subtracted positron annihilation γ-ray count rate data for the carbon target as a function of time after the last laser shot. The decay curve gives both an unambiguous identification of the generated reaction from the well-known half-life of the ^{12}C(γ,n)^{11}C reaction, and also a measure of the production rate. A fit to the resulting decay curve yielded a half-life of 20.5 $\pm$ 0.2 minutes (1230 s), in

close agreement with the literature value of 20.4 minutes (1225 s) [65]. Fitting of the data indicates that a peak 'detected' gamma activity of 76 counts/s was achieved at the last laser shot. After correcting for the measured detection efficiency and self absorption in the carbon target (~ 18 % correction), a total activity of 0.511 γ-ray emission at that time was estimated to be $2.1 \times 10^3/s$. Thus, during the 21 laser shots taken over a period of about one half-life, 1.9×10^6 ^{12}C nuclei were created, which translates to an average of $\sim 1.2 \times 10^5$ ^{11}C produced per shot, after correcting for loss due to decay between laser shots and after the last shot. The average laser energy on target was $\sim$1.1 Joule per shot for the carbon target excitation.

The same reaction was also studied previously by the group at LOA in France [67] using pulses from the 2 J, 30 fs, 800 nm, 4×10^{19} W/cm^2 "Salle Jaune" laser
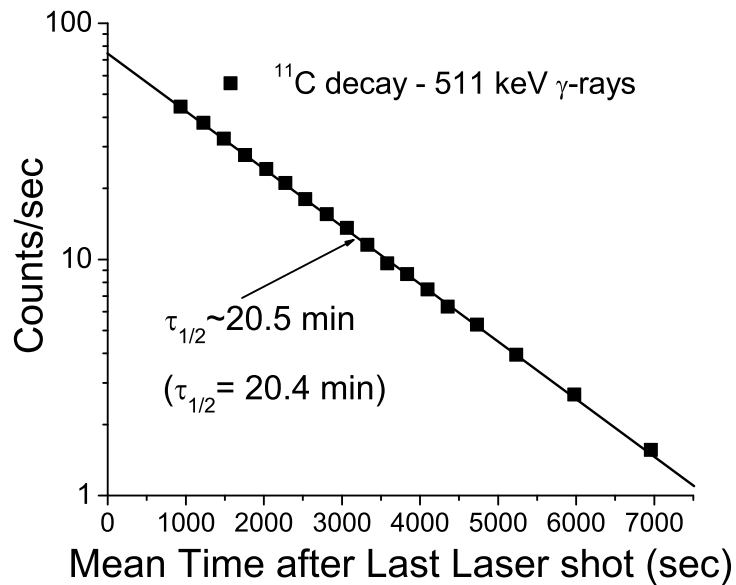
Figure 4.5: The measured count rate of 0.511 MeV γ-rays detected, with the background subtracted, as a function of elapsed time after the last laser shot for the C target. The solid line represents a single exponential fit to the data, with fitted half-life of 20.5 minutes compared to the established half-life of 20.4 minutes for ^{11}C beta decay.

in interactions with thin film targets. Electrons were produced from a 6 μm thick CH foil target generating peak electron energies of about 60 MeV with a 15 degree angular divergence. Analysis of activation results indicated production of about 1.4×10^3 ^{11}C nuclei per shot, with an estimated 5×10^9 electrons per laser shot lying above 5 MeV. To match the number of ^{11}C nuclei produced per shot in our experiment, simulations using the GEANT3 code [68] indicate a production rate of about $\sim 1 \times 10^9$ electrons/shot at 100-150 MeV. The much higher average energy of the accelerated electrons, and the consequent higher yield of bremsstrahlung photons generated above the ^{12}C(γ,n)^{11}C threshold is what led to the approximately 85-fold increased rate of activation observed per shot in the present experiments over previous experiments.

A 4.5 mm thick Cu target (natural abundance - 69% ^{63}Cu) was also exposed, placed at the same location as the C target, again with a 3 mm thick Ta converter inserted on the Cu surface facing the electron bursts [63]. The activation threshold

(a) ^{12}C(γ,n)^{11}C Cross Section

(b) ^{63}Cu(γ,n)^{62}Cu Cross Section
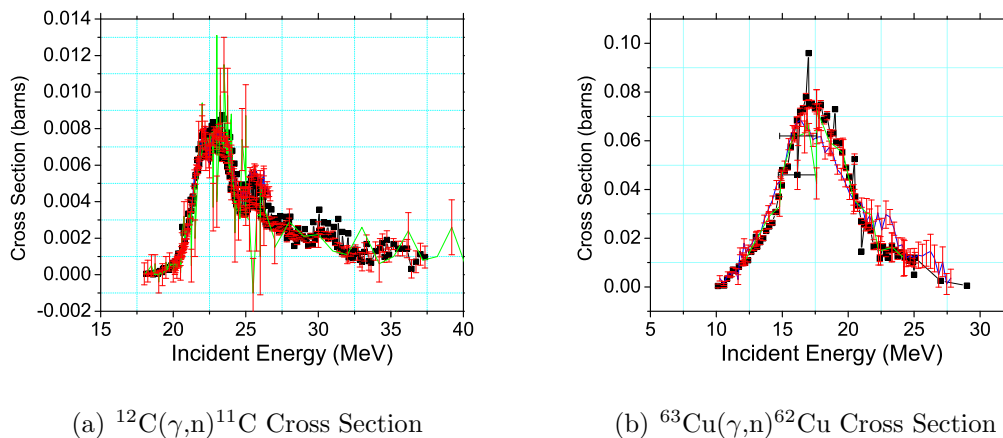
Figure 4.6: The number of fission events dramatically improves as a larger percent of the bremsstrahlung γ-rays lie within the giant dipole resonance (GDR) range. These plots show the (γ,n) reaction cross section for (a) C and (b) Cu in barns as a function of γ-ray energy - Data from the EXFOR database [66].
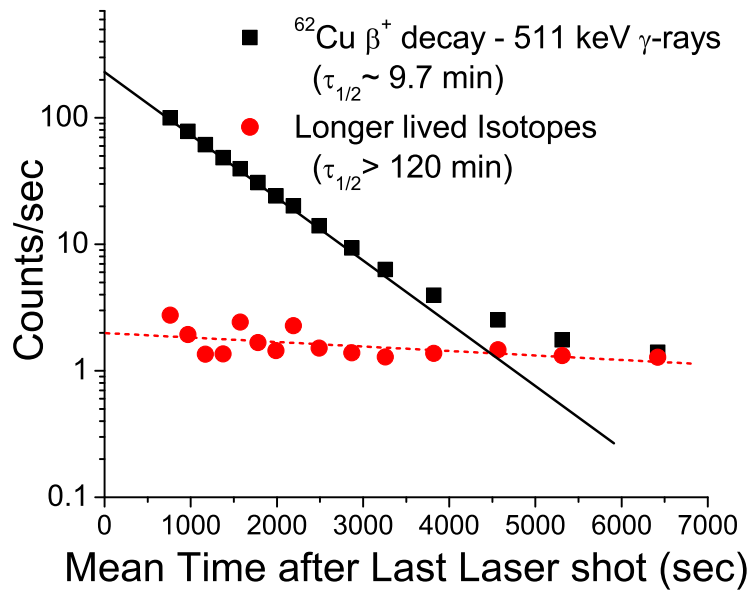
Figure 4.7: The measured count rate of 0.511 MeV γ-rays detected as a function of elapsed time after the last laser shot for the Cu target. The two curves indicate results of exponential fits to short- and long-lived components, representing γ-rays arising from decay of beta particles stopping in the target from beta decay of 62Cu from ^{63}Cu(γ,n)^{62}Cu (half-life 9.7 minutes) and from much longer-lived isotopes arising from more complex transitions, e.g., from ^{63}Cu(γ,2n)^{61}Cu.

for ^{63}Cu(γ,n)^{62}Cu is about 13 MeV as shown in Fig. 4.6(b) [69]. For ^{63}Cu(γ,n)^{62}Cu one expects strong 0.511 MeV γ-ray line emission from positron decay of the product nuclei. However, annihilation γ-rays also arise from production of longer-lived ^{64}Cu and ^{61}Cu isotopes through the ^{65}Cu(γ,n)^{64}Cu reaction (half-life of 12.4 hours), as well as through the ^{63}Cu(γ,2n)^{61}Cu reaction (half-life of 3.3 hours). The ^{65}Cu component constitutes 31 % in natural abundance copper. Thus, a laser shot accumulation time period was chosen that was about twice as long as the dominant decay ^{62}Cu half-life, but shorter than that of the longer lived product(s). Specifically, fifteen shots with an average energy of $\sim$1 J/shot were accumulated over approximately 18 minutes. The Cu target was then removed and γ-ray counting was begun within twelve minutes

of the last laser shot. Figure 4.7 shows the measured background-subtracted count rate of the 0.511 MeV γ-ray line as a function of time after the last shot. Short-lived and longer-lived components were separated through multi-exponential fitting of the decay curve. The short-lived component, exhibiting a half-life of 9.7 minutes, is attributed to beta decay of photo-produced ^{62}Cu. Using the same analysis as for C, we deduce a produced activity rate of about $5.2 \times 10^3/s$ 0.511 MeV γ-rays emitted at zero time after the last shot, arising from $\sim 2.3 \times 10^6$ ^{62}Cu nuclei produced during the fifteen laser shots, or a production yield of $\sim 2.5 \times 10^5$ ^{63}Cu$(\gamma,n)^{62}$Cu reactions per laser shot, after correcting for decay between shots. Compared to previous reported experiments by the LOA group [67] this is an increase of about a factor of twenty in production rate ((γ,n)'s per shot). The reduced enhancement in this experiment compared to carbon excitation is attributed mainly to the lower average laser energy/shot employed in excitation of the copper target. This reaction was also investigated by the LBNL group [70], using 10 TW, 50 fs pulses at 10 Hz interacting with a helium gas target, in which a near Boltzmann distribution electron energy spectrum was produced. They found about 1.6×10^3 reactions per second were induced by 4 to 5 nC of electrons per pulse with a measured low-energy peak electron energy distribution that extended beyond 25 MeV. To match the number of ^{62}Cu nuclei produced per shot in the present experiment, simulations using the GEANT3 code [68] indicate a production rate of about $\sim 3 \times 10^8$ electrons/shot at 100-150 MeV.

4.4   Photonuclear fission

Finally, we performed an experiment on photofission in a 2.9 mm thick, ^{238}U sample [71]. In this case, owing to the high nuclear charge of the target, no Ta converter

was necessary, as the sample itself was efficient in producing the bremsstrahlung γ-rays. For the very high-energy electrons produced in these experiments, a somewhat thicker U target would have more nearly optimized the rate of fission production because many of the high-energy bremsstrahlung photons escaped the present thin U target. For ^{238}U, we sought to analyze the products of ^{238}U(γ,fission)^{134}I, and ^{238}U(γ,fission)^{92}Sr having half-lifes of 53 minutes and 2.7 hours, respectively. The activation threshold for ^{238}U(γ,fission) is about 5.8 MeV as shown in Fig. 4.8 [66]. Thus, 72 laser shots with an average energy of 1 J/shot were accumulated during approximately 75 minutes and target γ-ray counting began within approximately 14 minutes after the last shot. The γ-spectrum was recorded every 10 minutes for the first 1.5 hours, every 20 minutes for the next hour, and every 60 minutes for the next 7 hours.
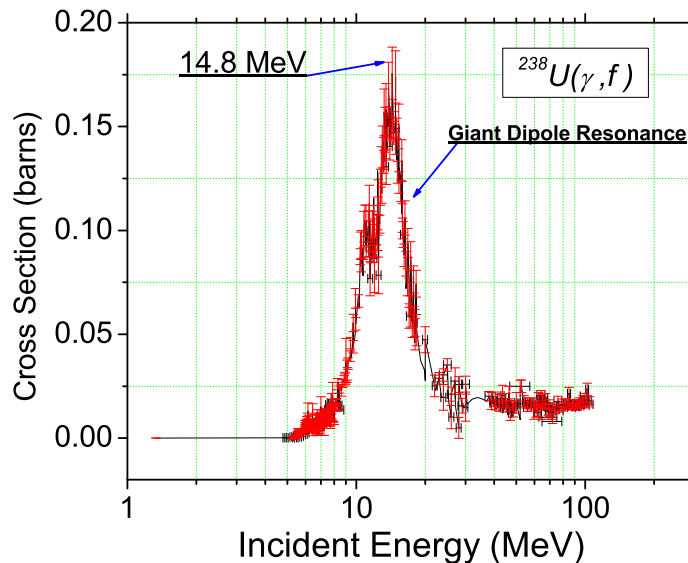
Figure 4.8: (γ,f) cross section for ^{238}U in barns as a function of γ-ray energy - Data from the EXFOR database [66].

The ^{134}I and ^{92}Sr fission products were identified, using an ORTEC GAMMX

Ge(Li) γ-ray detector, through their signature γ-decay of 0.847 MeV and 1.384 MeV γ-rays, as shown in Figure 4.9.
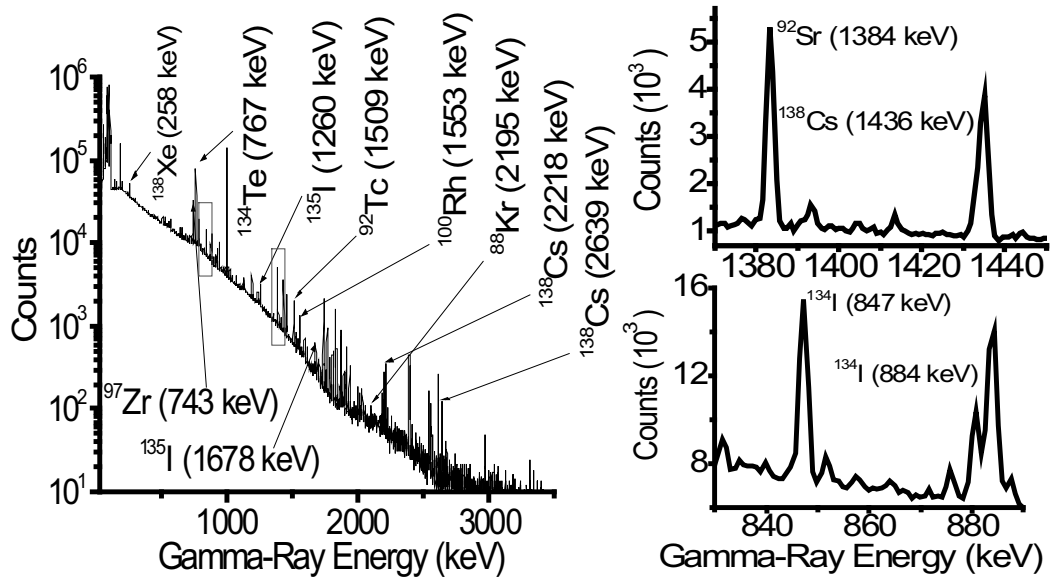
Figure 4.9: The measured count rates for the 847 keV γ-rays detected, as a function of time after the last laser shot for the ^{238}U(γ,fission)^{134}I process and for the 1384 keV γ-rays detected, with the background subtracted, as a function of time after the last laser shot for ^{238}U(γ,fission) ^{92}Sr.

The background-subtracted number of gamma counts was measured as a function of time for the principal 0.847 MeV γ-ray from the decay of the ^{134}I fission product, and is shown in Figure 4.10. The deviation from the exponential decay seen during the first two hours arises from feeding of the ^{134}I population by decay of heavier, relatively short-lived fission products to ^{134}I. Fractional primary fragment yields and isotope lifetimes for photofission of ^{238}U by 15 MeV photons are given in Table 4.1. Fragments heavier than ^{134}I (and ^{92}Sr) typically cascade via beta decay with the lifetimes given, and contribute to the observed γ-ray emission from ^{134}I (and ^{92}Sr). The overall contribution to the ^{134}I population from these cascade channels is approximately three times the direct fission production yield. Feeding of ^{134}I via beta-decay of ^{134}Te proceeds with a 42 minute half-life, which significantly affects the

observed time dependence of 0.847 MeV γ-ray emission during the initial few half-lives, after which the observed decay reverts to an approximately single exponential with the half-life of ^{134}I i.e., 53 minutes. The dashed curve in Fig. 4.10 shows the results of a relatively simple multi-exponential feeding decay model calculation using the relative primary fission fragment intensities and lifetimes relevant to ^{134}I given in Table 4.1.
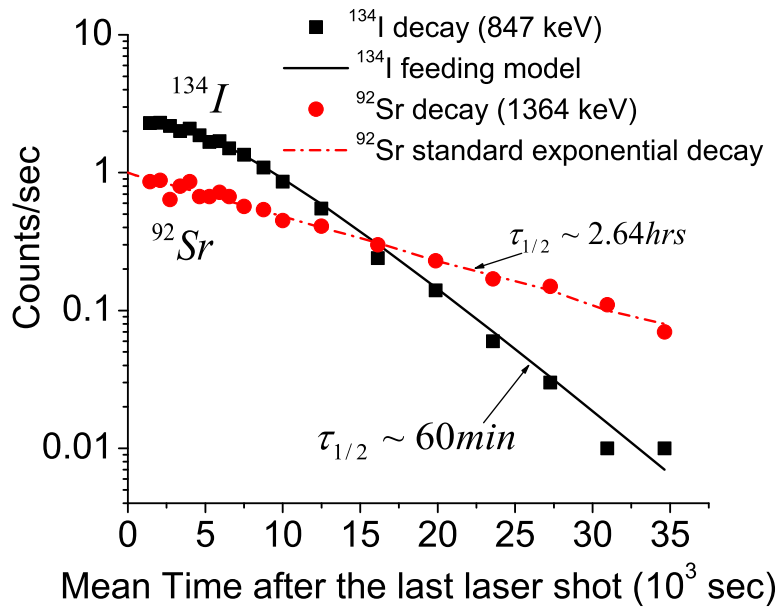
Figure 4.10: The γ-spectra taken from the irradiated uranium target. The signature γ-emission peaks from ^{134}I (847 keV) and ^{92}Sr (1384 keV) decay are present.

The measured decay curve for 1.384 MeV gammas from decay of ^{92}Sr fission products is shown in Fig. 4.10. Feeding of the ^{92}Sr population from other higher mass fission channels proceeds through beta decay more rapidly, so that virtually all of these contributions had decayed prior to counting of the sample, thus leading to the appearance of a single-exponential decay. Fits to the data for the 0.847 and 1.384 MeV γ-ray curves yield half-lives of 1.0 and 2.6 hours, compared to well-established

Table 4.1:
Fractional primary fragment yields and lifetimes for ^{238}U$(\gamma,$F$)$ fission at a gamma energy of 15 MeV for fragment isotopes significantly contributing in cascades to ^{92}Sr and ^{134}I used in calculations of fission yields from measured gamma activities.

		A = 92				A = 134	
Z_{frag}	Element	Fraction	Lifetimes(s)	Z_{frag}	Element	Fraction	Lifetimes(s)
35	Br	9.60×10^{-4}	3.40×10^{-1}	50	As	1.68×10^{-4}	1.00×10^{-0}
36	Kr	1.50×10^{-2}	1.84×10^{-0}	51	Sb	9.60×10^{-3}	1.04×10^{-0}
37	Rb	2.02×10^{-2}	4.48×10^{-0}	52	Te	3.84×10^{-2}	$2.52 \times 10^{+3}$
38	Sr	5.65×10^{-3}	$9.76 \times 10^{+3}$	53	I	1.33×10^{-2}	$3.16 \times 10^{+3}$

literature values of 53 minutes and 2.7 hours for ^{134}I and ^{92}Sr, respectively 16. Analyses and fitting of the time-dependent spectra indicate creation of approximately 2×10^7 of both ^{134}I and ^{92}Sr fission products, and therefore, $\sim 3.3 \times 10^5$ fissions per laser shot, assuming integrated fission yields of $4-5\%$ for each of these two channels [72].

This reaction was also explored previously by the LOA group [67] and they found a fission rate of about 10^4 per shot. Another group at Jena [73] also measured U-fission produced by bremsstrahlung from high energy electrons using 15 TW, 80 fs, 10 Hz laser pulses on a solid tantalum target, with the laser focused to a peak intensity of 10^{20} W/cm^2. They observed a laser plasma regime in which the electron energy distribution rapidly falls off with energy, and obtained about 7×10^3 ^{238}U$(\gamma,$f$)$ fissions per shot. Thus, the present result represents an enhancement of 33 to 47 times greater fission yield than the earlier experiments. To match the number of uranium fissions induced per shot in our experiment, simulations using the GEANT3 code [68] indicate a production rate of about 4×10^8 electrons/shot ($\sim$64 pC) at 100-150 MeV.

While the present table-top terawatt laser experiments, as well as others referred

Table 4.2:
Comparison of the laser systems and ^{238}U photofission rates achieved. The laser systems are the LLNL Nova Petawatt, the RAL Vulcan, the LOA "Salle Jaune", the Jena 15 TW laser, and the University of Michigan Hercules (present work). The first two of these employ doped glass amplifiers and therefore operate in essentially single shot mode, whereas the others use Ti:Sapp and operate at up to 10 Hz repetition rate. The present repetition rate was limited primarily by the ability to pump the residual gas from the target vacuum chamber (see text). Also listed here are the approximate peak laser intensities, pulse energies and durations, and the number of fissions inferred per Joule of laser energy and per laser pulse.

Laser	Rep. Rate (Hz)	Peak Int (W/cm^2)	Pulse Energy (J)	Pulse duration (fs)	Fission per J	Fission per shot
LLNL PW	10^{-4}	10^{20}	260	450	7×10^4	1.82×10^7
Vulcan	10^{-3}	10^{19}	50	1000	2×10^4	10^6
LOA	10	4×10^{19}	2	30	10^4	2×10^4
Jena	10	10^{20}	0.5	80	10^4	5×10^3
Hercules	0.017	10^{19}	1.2	30	3×10^5	3×10^5

to here, have aimed at demonstrating nuclear reaction rates that can be obtained with compact, relatively inexpensive, high repetition rate laser systems, laser driven photofission in uranium has also been produced previously by very high power, ps pulse lasers, namely RAL's Vulcan laser [69, 74] and LLNL's Nova Petawatt laser [75, 76]. Even with much greater energy per pulse, those single-shot experiments induced only somewhat greater rates of fission than found in the present experiment. For completeness, we summarize in the accompanying table 4.2 the characteristics of the laser systems and uranium fission rates for this full range of experiments.

As noted above, the photo-initiated radioisotope production yields obtained experimentally have been compared with Monte Carlo simulation results employing the GEANT3 code applied to the three targets exposed here to derive the numbers of high energy electrons striking the bremsstrahlung conversion targets. The simulation tracks the propagating electromagnetic shower through the target ma-
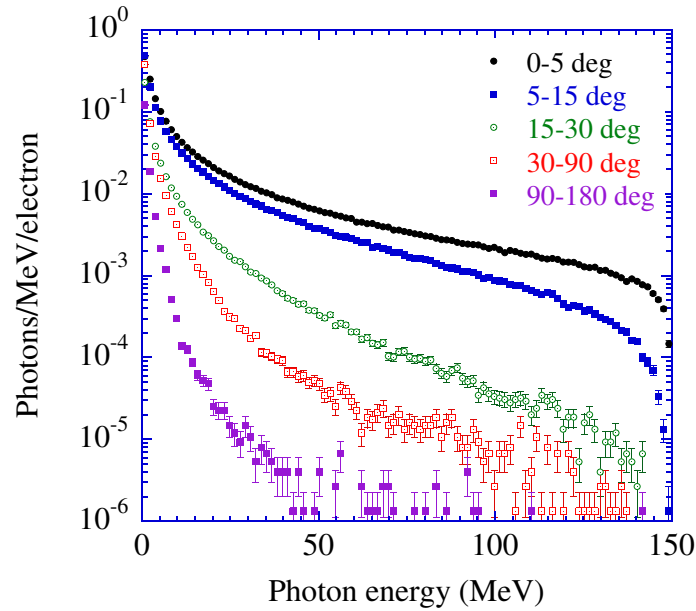
Figure 4.11: Monte-Carlo simulation showing the bremsstrahlung photon differential yield generated by 150 MeV electrons incident normally on a cylindrical target of ^{238}U - 2.9 mm thick and 11 mm in diameter. Plots show spectral distribution yields for different angular cones of bremsstrahlung emission

terial taking into account the bremsstrahlung and photofission resulting from the

bremsstrahlung γ-rays, as well as other photon and electrons interactions relevant to

the shower development. For example, using photofission cross sections from refer-

ences [77, 78] calculations were performed to derive the energy spectra for photons incident on U nuclei and the resulting fission yields. For the 2.9 mm thick sample used in the present measurements, the total yield of angle-integrated photons in the calculated spectrum above 1 MeV is 4.53 photons per incident electron, and the total yield above the 5.8 MeV fission threshold in ^{238}U is 2.16 photons per incident electron (Fig. 4.11). The uncertainty in these quantities due to Monte Carlo counting statistics is less than 0.1%. The uranium photofission cross section reflects the Giant Dipole Resonance (GDR) strength function [69]. It rises from its threshold at 5.8 MeV to a peak of 180 mb at 14.8 MeV, and then falls with increasing energy to 15 mb at 40 MeV as shown in 4.8. The cross section is roughly constant from 40 MeV to above 100 MeV. The photofission yield from photons above 25 MeV is small. The simulation shows that $70 - 75\%$ of the γ-radiation in the relevant energy range (6-25 MeV) is contained within a half angle of approximately 9 degrees with respect to the incident electron direction.

Table 4.3 gives the results of the GEANT3 calculations in terms of the expected yields per electron striking the Ta converter and isotope-production target combination, or the U target alone as functions of incident electron energy. The statistical uncertainties are less than $\sim 10\%$ in most cases. A comparison with the radioisotope yields derived from the experimental gamma intensity measurements indicates, as noted in the text, that on average 0.06 to 0.2 nC of 100-150 MeV electrons were accelerated and struck the converter targets per laser shot. The average charge differences for the different targets can be attributed to the electron beam's shot-to-shot angular and energy fluctuations which may be caused from variations in the laser parameters (i.e. energy, spot size, pulse duration) or plasma conditions. It is important to point out the charge discrepancy based on the ICT measurement,

Table 4.3:
Calculated photonuclear events per electron as a function of electron energy for the measured target combinations. GEANT3 Monte Carlo simulations were performed as described in the text.

E_{e^-}(MeV)	$Ta + C$	$Ta + Cu$	U
10	$----$	$----$	1.15×10^{-5}
15	$----$	$----$	1.42×10^{-4}
20	$----$	4.15×10^{-5}	2.84×10^{-4}
40	4.40×10^{-5}	2.93×10^{-4}	5.06×10^{-4}
80	9.40×10^{-5}	4.90×10^{-4}	6.34×10^{-4}
100	1.18×10^{-4}	5.07×10^{-4}	6.36×10^{-4}
150	9.00×10^{-4}	6.92×10^{-4}	6.40×10^{-4}

which shows about 300 pC-500 pC, and the accurate activation experiments, showing $\sim$100 pC. High electronic noise levels and low energy electrons not detected by the spectrometer can influence the ICT measurements as shown in [79].

4.5   Conclusions

In summary, the generation of quasi-monoenergetic electron beams with energies above 300 MeV and with $\sim$10 mrad angular divergence was reported. It was shown that by changing the plasma density from $n_e = 3.5 \times 10^{19}$ to 2×10^{19} cm^{-3} the corresponding electron beam energy steady increases from 80 MeV to 120 MeV. As the plasma density was further decreased between 1.8×10^{19} to 1.5×10^{19} cm^{-3} a pronounced rise in electron beam energy, up to 320 MeV and greater beam stability was observed.

Radioisotope production by laser wakefield acceleration of electrons and subsequent photonuclear processes were measured and showed significantly enhanced rates over previous measurements for several target species. These enhanced results were made possible because of the new regimes of nearly monoenergetic electron acceleration. By using the laser/target parameters necessary to reach the quasi-

monoenergetic electron regime, (γ,n) reaction rates in C were obtained that were about 85 times greater than in previous experiments and (γ,n) rates in Cu were about 20 times greater than in previous experiments. Regarding (γ,fission) in ^{238}U, fission rates about 30 to 45 times greater than in previous experiments were obtained, that are comparable to results from 50-260 J/pulse single shot large-scale glass lasers at the Vulcan and the Livermore Nova Petawatt facilities.

CHAPTER V

Two-Stage Proton Acceleration from Hydrogen Containing Ultrathin Targets

The generation of multi-MeV protons from the interaction of a high intensity laser incident on thin foil is an exciting area of research with several potential applications such as fast ignition [11], charged particle radiography [80] and proton therapy [81]. Gitomer *et al.* [82] and Davies [83] showed the maximum proton energy scales with the laser irradiance $I\lambda^2$, and can be fit by a function of the form $(I\lambda^2)^\alpha$, where α is between 0.3-0.5. For ultra-thin foils and sufficiently high laser contrast, simulations show ultra-short lasers can accelerate protons to tens of MeV from a 30 TW laser and even to 100 MeV for intensities greater than 10^{22} W/cm^2 [84].

However, the source of the highest energy protons from laser interactions with thin foils is still debated. Two possible origins are the front or rear target surface. In the first case, the laser's ponderomotive force creates a charge separation occurring at the front surface strong enough to accelerate protons through the target with several MeV energies [34, 35, 39, 85]. In the second case, target normal sheath acceleration (TNSA) describes an electrostatic sheath normal to the target's rear surface due to relativistic electrons accelerated at the laser plasma interface [40, 36]. These electrons propagate through the material and are trapped by the charged target. The electric

field ionizes and accelerates the hydrogen containing contaminants to several MeV energies. Particle-in-cell simulations presented by Pukhov [86] and d'Humieres *et al.* [87] show proton generation due to both of these acceleration mechanisms. Because of the difficulty of independently measuring these potentially coupled acceleration mechanisms, the influence and contributions of each are still unknown experimentally.

In this chapter, the maximum proton energy generated from submicron thick targets using ultrahigh intensity (4×10^{20} W/cm^2), high contrast (10^{-11}) laser pulses is explored as a function of target material and hydrogen content. It is shown for the first time experimentally that protons initially accelerated from the laser's focal volume receive an additional acceleration from the rear sheath. The two stages of acceleration have been experimentally distinguished through target selection. It was observed that the maximum proton energy for hydrogen containing targets such as Mylar and CH was two times higher than for non-hydrogen containing targets such as Si$_3$N$_4$. This is because when hydrogen is in the focal volume, the protons are accelerated first by the pondermotive potential, propagate through the target body and receive additional acceleration due to the rear sheath, whereas Si$_3$N$_4$ only receives TNSA thus yielding lower proton energy. Hydrodynamic simulations are used to study the ultra-thin foil expansion due to the influence of the laser prepulse. Additionally, PIC simulations are used to study the mechanism of the laser plasma interaction and proton acceleration.

5.1 Experimental setup

The experiment was performed with the Hercules laser which delivered 4×10^{20} W/cm^2 intensity and 30 fs pulse duration corresponding to a normalized vector potential a_0 of 13.6. The experimental setup is shown in Fig. 5.1.
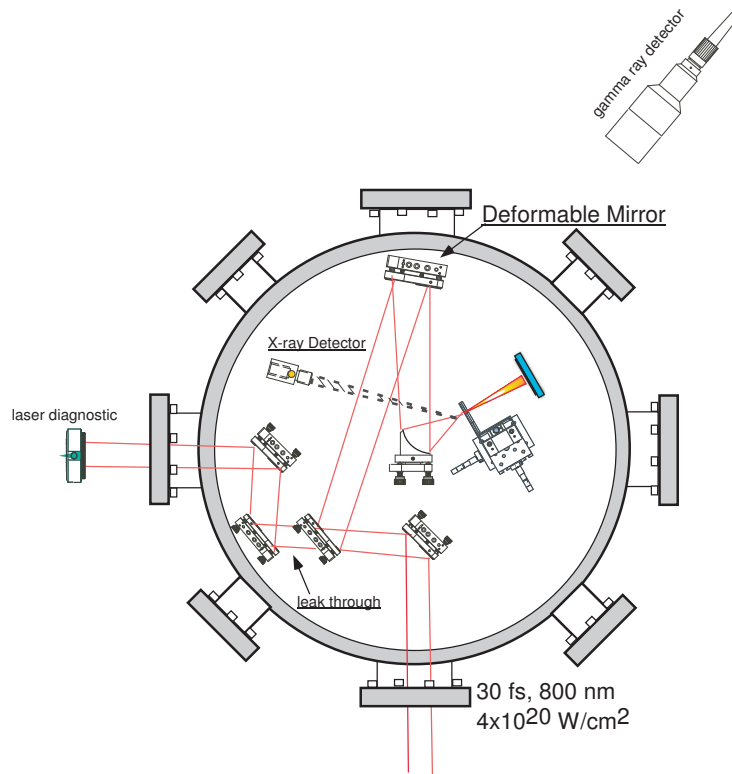
Figure 5.1: Solid target experimental setup. The laser pulse is focused to an intensity of $\sim 4 \times 10^{20}$ W/cm^2.

The energy on target was 1 Joule with a relative standard deviation of $\pm$ 10% shot-to-shot fluctuation. Amplified spontaneous emission (ASE), as measured by a third order autocorrelation, began roughly 5 ns before the peak pulse at a contrast level of 10^{-11}. Then the contrast was measured to be 10^{-8} $\sim$30 ps before the laser peak. The wavefront-corrected beam was focused by an f/2 off-axis parabolic mirror to a 3 μm spot size (FWHM), giving a Strehl ratio greater than 0.7 on every shot. The p-polarized laser was focused at a 20° angle of incidence upon varying target materials.

The maximum proton energy and spatial distribution were measured by placing 2 x 2 inch CR-39 track detectors 6.0 cm behind the target. CR-39 was chosen for its insensitivity to laser light, x-rays, γ-rays and electrons when shielded with a

thin Al foil. Heavy particles, such as protons and ions, leave a trail of damage and pits are formed by soaking CR-39 in a high temperature, 6.25 N, NaOH solution between 1 to 8 hours. After soaking, the pits can easily be observed under a light microscope. Stacks of Mylar filters were used as a stopping material which takes advantage of the sharp Bragg peak to precisely measure the maximum proton energy. The proton spectrum was measured with three 0.45 T, 2.5 cm permanent magnetic ion spectrometers mounted 2 cm away from the target.

The proton spectrum was measured along the target normal (0°), laser axis (20°) and at 10° through a 120 μm aperture covering a solid angle of 1.1×10^{-6} steradians. The hot electron divergence, maximum energy, temperature, and pointing stability were measured 6 cm behind the target by imaging a Kodak Regular LANEX screen with a 12-bit CCD camera. A one inch diameter, f/2 lens was placed $\sim 10^o$ degrees off the specular direction to measure the second and three-halves harmonic generation as a laser plasma diagnostic. The target was positioned to within ± 5 μm of the laser focus. This was done by simultaneously irradiating a thick aluminum plate scanned through focus and maximizing the generated x-rays and γ-ray signals. The ± 5 μm resolution is much smaller than the laser's ~ 25 μm Rayleigh range. The laser contrast was measured on every shot by focusing laser light leakage through a dielectric turning mirror onto a fast photodiode. Plastic (Mylar, CH), silicon nitride, and aluminum targets were used in the experiments.

5.2   Experimental results

5.2.1   Proton energy as a function of target thickness and material

The maximum proton energy for dielectric targets (Mylar, CH, silicon nitride) of varying thicknesses is shown in Fig. 5.2. The experiments consistently showed

the maximum proton energy from transparent dielectrics targets was independent of target thickness, with the exception of 100 nm CH. When comparing silicon nitride to CH targets a sharp drop in proton energy from 4 MeV (CH) to $\sim$2.0 MeV (Si$_3$N$_4$) was observed. Although the dielectrics are comparable in target thickness and have a damage threshold above the laser ASE intensity, they differ in hydrogen content. CH, Mylar, Si$_3$N$_4$ contain 67%, 36%, and 0% hydrogen respectively, although Si$_3$N$_4$ does have hydrogen containing impurities on its surface. Silicon nitride foils from 500 to 50 nm yielded roughly the same maximum proton energy, however for target thicknesses below 50 nm no protons, x-rays, or γ-rays were observed.
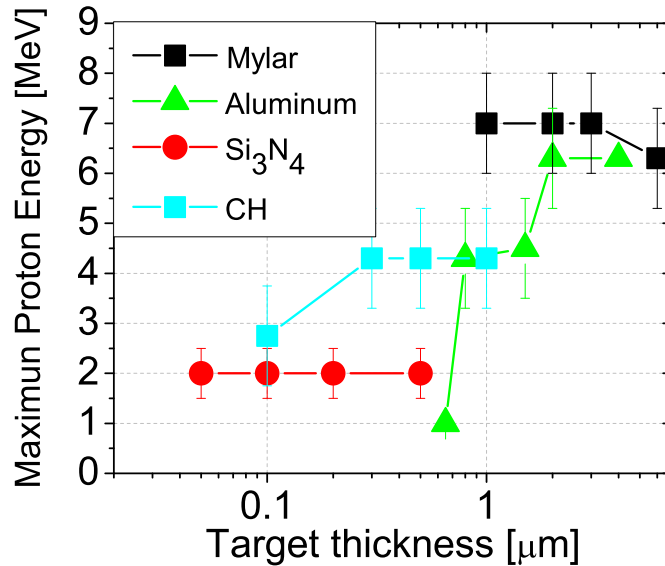
Figure 5.2: Maximum proton energy as a function of target thickness for CH, Mylar, Si$_3$N$_4$ and Al.

In the past, thin Al targets have been the target of choice for proton acceleration experiments because of their low cost and availability. The highest number of hot electron is expected at the rear surface for conducting targets, thus creating a stronger sheath and higher proton energy [88, 89]. The transport of hot electrons though

an overdense plasma strongly depends on the cold return shielding current. It is shown in Ref. [88, 89] that the return current in conductors is stronger, so more electrons can propagate through the target and create a stronger sheath. However, this was not directly observed for the presented experimental results. For Al target thicknesses less than 2 μm the proton energy dropped quickly from $\sim$6 MeV to 1 MeV. The observed drop can be explained by the laser ASE intensity. The third order autocorrelation showed a $\sim$30 ps pulse foot with an intensity greater than 10^{12} W/cm^2, which is above the damage threshold for metal targets but below the damage threshold for dielectric materials.

5.2.2 Proton spectra

Figure 5.3 shows typical proton spectra measured at three different angles: 0°, 10°, and 20° to the normal for two different types of targets, hydrogen containing Mylar and CH and non-hydrogen containing Si$_3$N$_4$. Proton spectrum for a single thickness (100 nm Si$_3$N$_4$, 300 nm CH, 1 μm Mylar) is shown and represents a typical spectrum from that material type.

The spectra differ in that the maximum proton energy is higher for the hydrogen containing materials. As described in more detail in section 5.5, for very thin foils, the protons accelerated from hydrogen targets receive strong acceleration at the front and rear target surface giving them higher energy than from protons from Si$_3$N$_4$ targets, which only receive acceleration at the rear. The total proton number at the maximum energy is the same order of magnitude for both hydrogen and non-hydrogen containing targets. The highest energy protons are accelerated normal to the target and the proton number and energy decrease as the observation angle approaches the laser axis. These characteristics are consistent with target normal

(a) 100 nm Si_3N_4

(b) 300 nm CH

(c) 1 μm Mylar
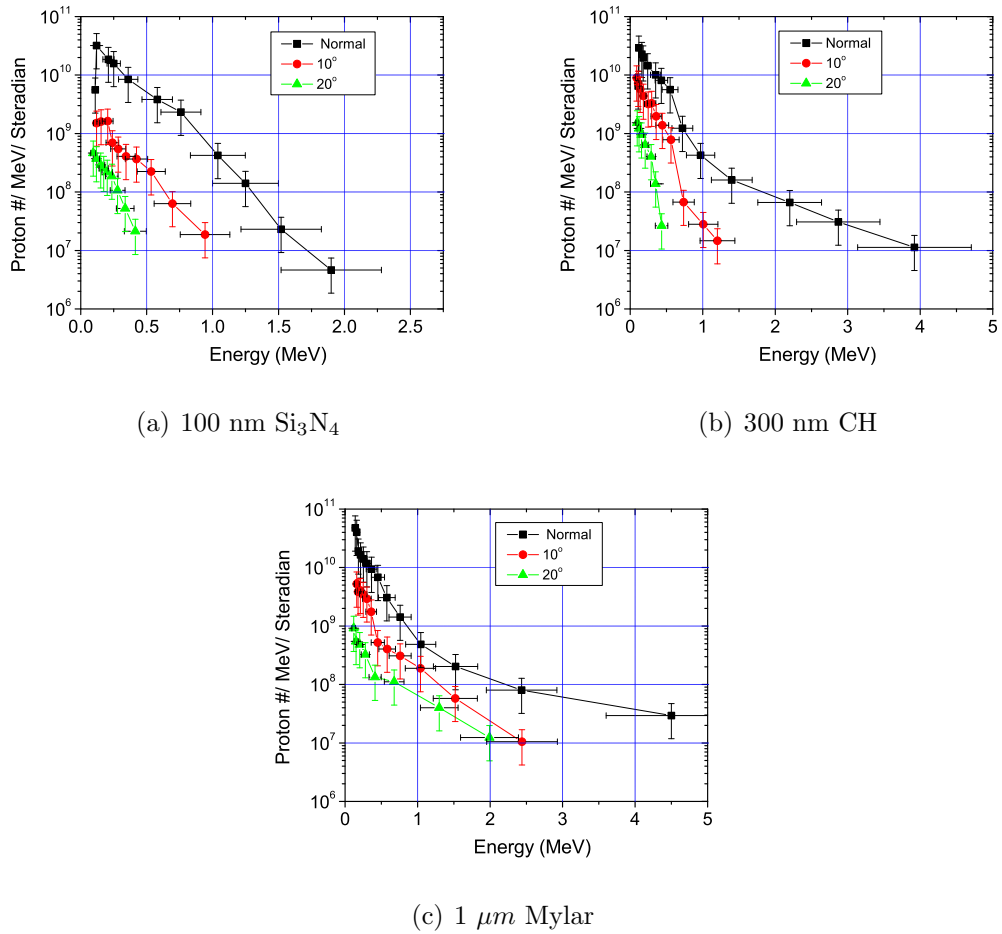
Figure 5.3: Proton spectra measured with a 0.45 T magnetic spectrometer at three different angles, 0°, 10°, and 20° to the normal.

sheath acceleration (TNSA) [38, 90]. For all targets, the direction of the proton beams was in the normal or slightly shifted toward the laser axis.

For 100 nm Si_3N_4 targets, the proton spectrum along the target normal axis shows a maximum proton energy of 1.8 MeV and a single temperature of $\sim$215 keV, fit using a Boltzmann distribution, $f(E) \sim \exp(-E/T)$, where E and T are the proton energy and temperature in MeV. However, for the hydrogen containing targets the maximum proton energy is approximately 4 MeV (2 x higher) and there are two proton populations with different Boltzmann-like distributions allowing one to identify a T_{Hot} and T_{Cold} component. One μm Mylar has a hot component with a

temperature of $T_{Hot} = 1.32$ MeV and a cold temperature of $T_{Cold} = 192$ keV. 300 nm CH has a similar two temperature spectrum with $T_{Hot} = 0.95$ MeV and $T_{Cold} = 233$ keV.

The cold temperature component from hydrogen containing targets ($\sim$200 keV) is similar to the single temperature distribution in Si_3N_4 ($\sim$200 keV). The two temperature spectrum is a large distinction between hydrogen and non-hydrogen containing targets and can be attributed to protons being accelerated at different locations and times during the interaction. In hydrogen containing targets protons may originate from the front, middle or rear of the target. The protons within the bulk material and rear surface are accelerated from different locations and appear to make up the cold component of the spectrum. The hot component is made up of protons which experience both front and rear target acceleration.

As shown in PIC simulations of high Z targets and simple numerical models of proton behavior described by a freely expanding plasma into vacuum [41, 91, 92], the protons exhibit a single exponential decay in number as the proton energy increases. The additional structure in the spectra for hydrogen containing targets *was* observed in the hydrogen PIC simulations where the low energy protons were observed to come from multiple locations and times but did not affect the mechanism of the high energy protons. The hot component, is the small fraction of protons which experience the full strength of the accelerating fields. In other words, a small fraction of protons in a hydrogen target are accelerated from the front and rear where the field strengths are maximum. In the experiments, approximately 3×10^7 protons/MeV/str were generated at 4.5 MeV in 1 μm Mylar. 1 steradian is $(180/\pi)^2$ or 3282.8 square degrees. Assuming a 3° divergence angle for the 4.5 MeV protons gives approximately 6×10^4 protons out of a total of $\sim 1 \times 10^{11}$ protons or ~ 0.0001 % were accelerated

along the strongest fields.

5.2.3 Spatial profile of the proton beam

The spatial profile of the generated proton beam was measured in order to compare the proton divergence for different target materials and thicknesses. The CR-39 detector consisted of strips of Mylar filters. By using stacks of filters with different thickness, the ions with energies above the stopping range deposit their energy in the CR-39 [93]. Therefore, the proton signal on the CR-39 is due to protons within a narrow energy range allowing one to measure the spatial distribution of the maximum proton energies.
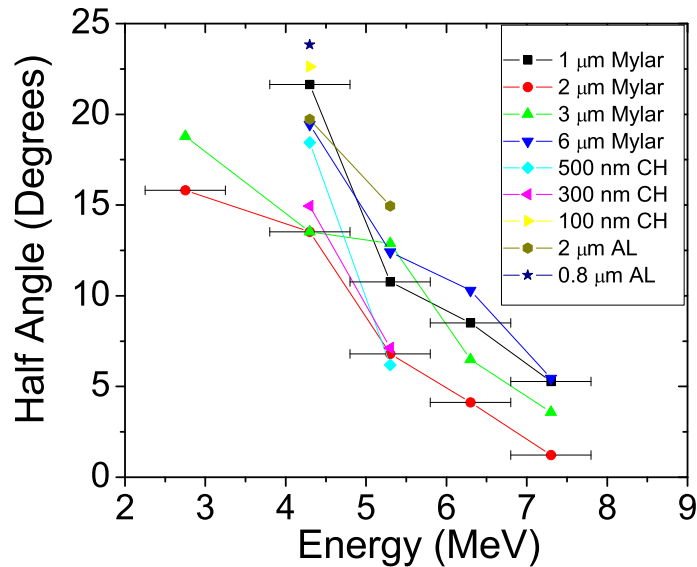
Figure 5.4: Half angle energy steps for Si_3N_4, CH, Mylar, and Al for varying target thicknesses. The plot was taken from the CR-39 raw data and shows that the divergence angle decreases as the proton energy increases. The divergence angle shows a similar trend for all the targets materials and thicknesses.

Fig. 5.4 shows that the proton beam half-angle divergence increases linearly from $\sim 3^o$ to $\sim 20^o$ when the proton energy drops from $\sim$7 MeV to about $\sim$3

MeV. Therefore, laser accelerated protons are highly directed with a small transverse emittance. The proton beams source size can be measured by placing a mesh screen in the beam path [94]. By knowing the properties of the mesh screen and the geometric setup the virtual proton source can be calculated with the following expression, $lvs = (L-lmD/dm)/(D/dm-1)$, where lvs is the distance of the virtual source to the target, lm is the mesh distance behind the target, L is the CR-39 distance from the target, and D is the diameter of the mesh image on the CR-39. Once lvs is calculated the proton source size at the rear of the target is given by $ds = D * lvs/(lvs + L)$. An example of the experimental setup and mesh image are shown in Fig. 5.5(a) and Fig. 5.5(b) respectively.

The mesh image shows the protons are accelerated from $\sim 150 \ \mu$m diameter region the back surface of the target. Assuming a $\sim 1^0$ divergence was measured for 7 MeV

(a)

(b)
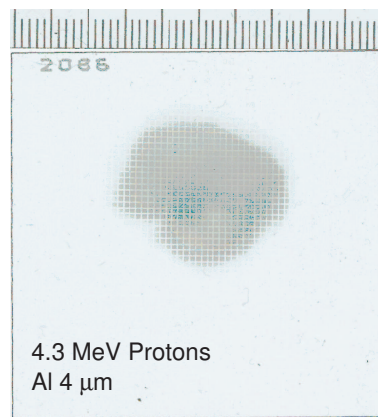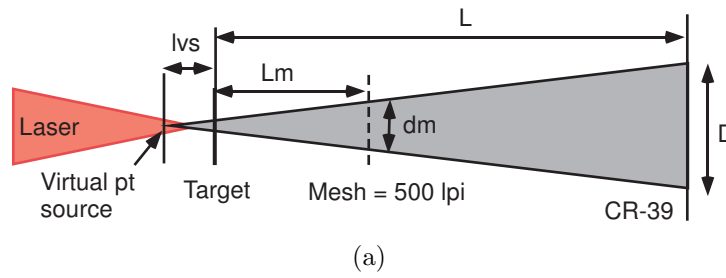
Figure 5.5: (a) Schematic of virtual proton source. (b) Shadow of the mesh grid imprinted in the proton beam profile.

energy, this yields a normalized transverse emittance [94], given by $\varepsilon \sim \beta r_o \Delta\theta$, of 0.05π mm mrad, where r_o is the transverse radial size, β is the ratio of the proton velocity to the speed of light, and $\Delta\theta$ is the divergence angle.

The observed energy cones can be explained by the following. During the rear sheath acceleration process, a Coulomb repulsion among the protons early in the acceleration stage gives them some transverse momentum [95, 96]. The low energy, slow moving protons take a longer time to accelerate through and thus have more time to propagate in the transverse direction. This leads to the observed energy emission cones as illustrated in in Fig.5.6.
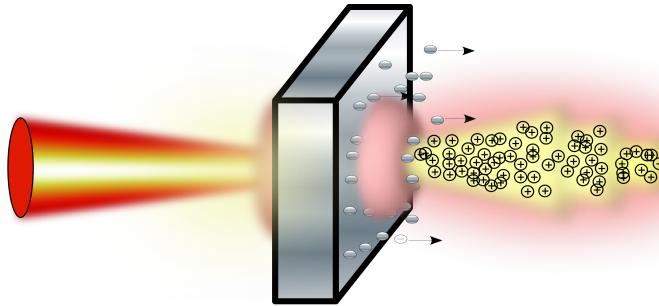
Figure 5.6: Simple schematic of the proton energy cones observed in the experiment. The highest energy protons have the smallest divergence angle.

5.2.4   Electron beam characteristics

Hot electrons produced during the laser plasma interaction play a critical role in determining the maximum proton energy in the TNSA regime [36]. As the incident laser propagates through the preplasma it accelerates electrons near the critical surface to several MeV energy/temperature [97]. These hot electrons exit the material, charging the target and creating an electrostatic sheath. Because the rear field strength is linearly dependant upon the number of electrons which make up the sheath, high Z, conducting materials will provide a large number of electrons.
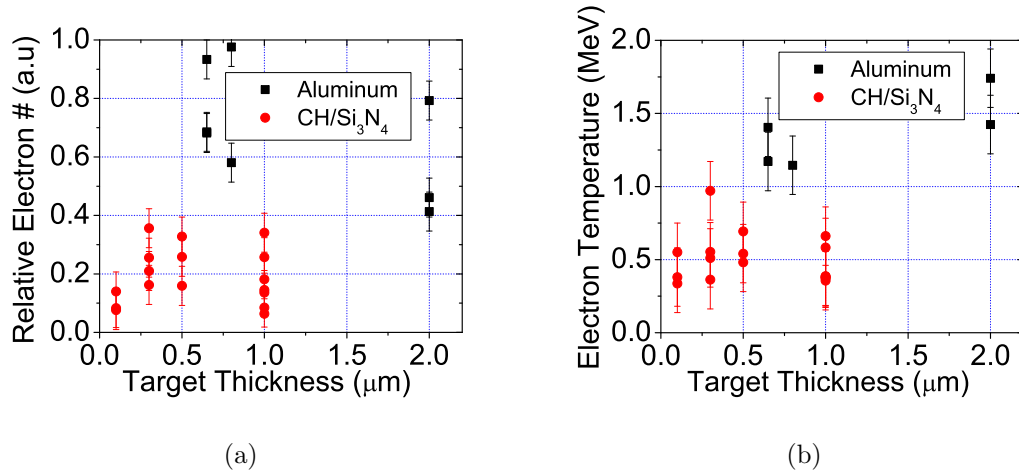
Figure 5.7: (a) Relative number of hot electrons as a function of target thickness and (b) Comparison of the electron temperature of Al vs CH

Fig. 5.7(a) shows the relative number of electrons as a function of target thicknesses. The relative number of electrons was measured by background subtracting the total integrated number of counts imaged from a Kodak Regular LANEX screen with a 12 bit CCD camera. A 200 μm aluminum shield enclosed the Lanex screen passing $\sim$180 keV electrons and above. Aluminum targets show roughly 3 times more hot electrons than dielectric targets. It was observed that the number of hot electrons is independent of the target density. Although silicon nitride is the most dense target, it yields approximately the same number of electrons as the CH and Mylar targets, while Al yields the most electrons. However, the number of electrons which escape does depend on conductivity of the plasma. In order for the hot electrons to efficiently propagate through the target a return current has to be generated. Because the return current is carried by the cold background electron population with a slow drift velocity it is affected by the target conductivity [89, 98, 99]. The electron temperature (Fig. 5.7(b)) was measured using aluminum step filters and fitting a Maxwellian-like distribution. The Al targets create a plasma temperature

~2x higher than dielectrics which may allow Al to create a stronger rear sheath. The hot electron temperature was measured to be ~1.3 MeV for Al and ~0.6 MeV for dielectrics. The electron beam divergence was roughly 30^0 full angle and showed a maximum energy of ~5.0 MeV (based on electron stopping range in Al from the NIST webpage [100]) for both metals and dielectrics. The electron beam was centered $\sim 10^o$ from the target normal toward the laser axis with $\pm 5^o$ shot-to-shot pointing stability.

5.3   Hydrodynamic simulations

In order to obtain the plasma conditions due to the prepulse, which the main laser will interact with, the 1-D radiation hydrodynamic code Hyades [101] was used. Hyades is a Lagrangian, 1-D, three-temperature, radiation hydrodynamic code. Radiation hydrodynamics and plasma properties are required to treat laser ablation processes and shock propagation. The radiation temperature, electron and ion temperature are calculated and tracked separately. A Lagrangian code assigns parcels of material to zones, and the mass remains in the zone during the simulation. As the simulation evolves, the zones expand or compress as the material density changes. Radiative energy transport in Hyades is treated in a multi-group prescription meaning the photons are divided by wavelength into groups. The opacities for each group of energy are calculated. The degree of ionization can be determined by one of the following models: Saha, Thomas-Fermi, LTE average-atom, time dependant or steady-state non-LTE average-atom, or fully ionized model. The response of the material is defined by thermo-mechanical and transport models. For sufficiently long time scales, where non-equilibrium effects are ignored, the material response depends on the mass density ρ, temperature T and material composition. The material's ther-

modynamic and equation of state properties are derived from realistic (SESAME or other theoretical models) tables, quotidian equation of state (QEOS), or an ideal gas model.

The laser in the hydrodynamic simulation is incident from the right and the front edge of the targets start at position zero. In the simulations the targets were irradiated with an 800 nm, 1 mJ pulse ramping from 10^9 W/cm^2 to 10^{15} W/cm^2 over 30 ps, coming in at a 30 degree angle of incidence which models the Hercules laser prepulse interacting with the target. The Thomas-Fermi ionization model was used in the plots below to calculate the laser deposition and heat condition.
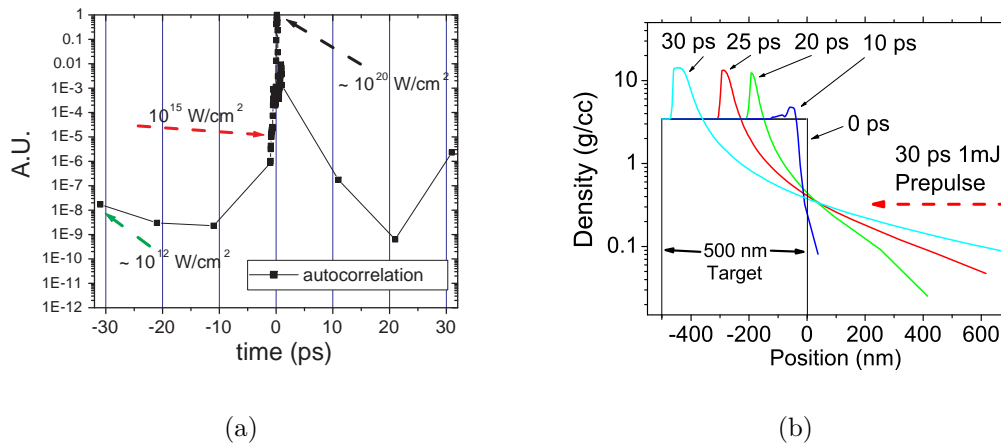
Figure 5.8: (a) 3ω autocorrelation. (b) Hyades simulation: Evolution of the density structure of a 30 ps, 1 mJ prepulse incident upon a 500 nm Si$_3$N$_4$ target.

Fig. 5.8(a) shows a 3rd order autocorrelation of the HERCULES laser. This was referenced in order to create the simulation prepulse. Fig. 5.8(b) shows the results of a simulation of a 500 nm Si$_3$N$_4$ target irradiated with a laser prepulse and the corresponding preplasma conditions at 10, 20, 25, and 30 ps. The simulation shows a laser generated shock wave propagating through the target and the relativistic critical surface, defined for the main pulse (4×10^{20} W/cm^2), expands out approximately 1 μm in front of the target. For "thick" targets, such as 500 nm, the rear surface is

still maintained after the 30 ps run time which is when the peak pulse arrives.
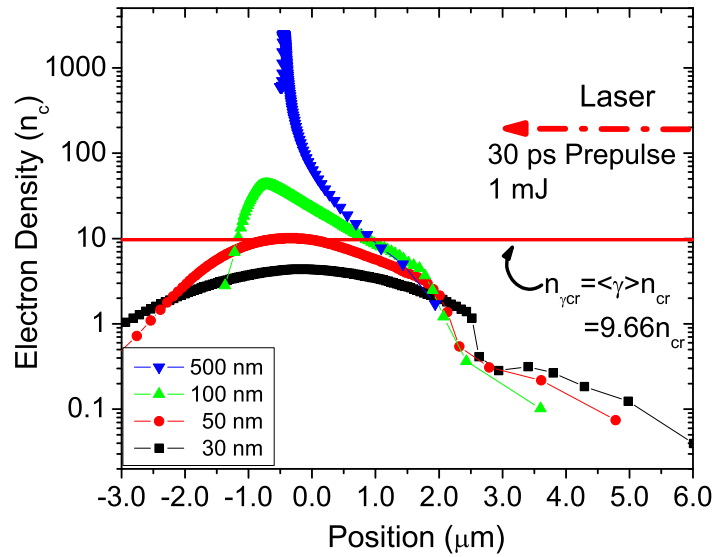
Figure 5.9: Hyades simulations of the interaction of a 1 mJ pulse ramping from 10^9 W/cm^2 to 10^{15} W/cm^2 over 30 ps, coming in at a 30 degree angle of incidence upon 4 different target thicknesses. 500 nm, 100 nm, 50 nm, 30 nm Si$_3$N$_4$. The simulations show the target heats up and expands several microns in both the forward and rear directions. The rear plasma expansion causes a weakening of the target rear sheath which accelerates protons in the TNSA regime.

Fig. 5.9 shows hydro-simulations for 4 Si$_3$N$_4$ targets with different thicknesses (500 nm, 100 nm, 50 nm, and 30 nm) at 30 ps where the y-axis is electron density in units of the non-relativistic n_c. A red line is drawn at 9.66 n_c representing the relativistic critical density where the peak laser pulse will strongly interact. As the laser arrives the target quickly ionizes and the plasma expands into vacuum. Although the preplasma expands several microns for all 4 targets (500 nm, 100 nm, 50 nm, 30 nm), the scale length increases while the peak electron density decreases as the target thickness is reduced. This can dramatically change the dominant mechanism in how the laser energy is coupled to the target - for example, resonance absorption for short

scale length or Brunel heating for sub-wavelength scale length. The plasma density scale length at the relativistic critical surface ($n_{c\gamma} = 9.66n_c$) are $0.6\lambda, 1.2\lambda, 4.3\lambda$ for 500 nm, 100 nm, and 50 nm respectively, noting that 30 nm is below $n_{c\gamma}$. The 30 nm target creates a 10 μm thick plasma with a peak electron density ($\sim 3n_c$) below the relativistic n_c allowing the main laser to propagate through, but not allowing protons to be accelerated efficiently as shown experimentally. This is consistent with the measured proton data where no protons were observed for 30 nm targets. When the high intensity pulse arrives upon the 50 nm target the peak electron density is ~ 10 n_c, almost matching the relativistic n_c of 9.66 n_c, suggesting that the laser transmission can change drastically due to laser shot to shot fluctuations and may or may not produce a strong proton beam. The laser generated shock wave, observed for thick targets, appears to lose energy and doesn't have a significant effect on thin targets. The important result of these simulations is the long scale length observed at the rear of the target. Because the rear of the target is completely deformed a strong rear sheath cannot be created thus effecting the accelerated proton energy.

The results of these HYADES simulations may have important implications for ultrahigh intensity thin target experiments. In this section Hyades was used to simulate the profile of the plasma generated by the Hercules laser prepulse in order to understand the conditions the main pulse will interact with and its effects on the generation of protons. The simulations showed a significant rear side plasma density gradient for targets thinner than 500 nm. The simulations showed that a 50 nm thick target was converted to near critical density plasma which expanded several microns in thickness at both the front and rear surface. In the next section, numerical and analytical arguments show that an initial proton density scale length at the rear surface of the target will dramatically reduce the proton energy due to a

poorly formed rear sheath.

5.4 Numerical solutions and the influence of a rear side density gradient

In the previous section, HYADES was used to model the effect of the laser pre-pulse. The simulations showed the proton/ion density at the rear side of the ultra-thin target can extend several microns completely altering the rear surface integrity. This section uses a one dimensional simulation for the rear side acceleration of protons to quantify the influence of the initial proton density gradient caused by the prepulse. This sections uses the analytical formulas derived in chapter 2 which are based on the 1-D model originally developed by Mora *et al.* [41] and Crow *et al.* [42].

As discussed in chapter 2 the target normal sheath acceleration mechanism strongly depends on the electron density and temperature which make up the rear sheath. An equally important parameter is the initial density distribution of the protons at the rear surface. The analytical solutions in chapter 2 are only valid for step-like distributions and cannot account for a preformed density gradient. In order to analyze this effect the Poisson equation, the equation of motion and the continuity equation given below must be solved numerically. The acceleration mechanism model is described by the following equations

$$\epsilon_0 \frac{\partial^2 \Phi(z,t)}{\partial z^2} = e(n_e(z,t)) - n_i(z,t)) \tag{5.1}$$

$$\left[\frac{\partial}{\partial t} + v_i(z,t)\frac{\partial}{\partial t}\right] n_i(z,t) = 0 \tag{5.2}$$

$$\left[\frac{\partial}{\partial t} + v_i(z,t)\frac{\partial}{\partial t}\right] v_i(z,t) = -\frac{e}{m_i}\frac{\partial \Phi(z,t)}{\partial z} \tag{5.3}$$

where $n_e(z,t)$ and $n_i(z,t)$ are given by,

$$n_e(z,t) = n_{e0} \exp\left[\frac{e\Phi(z,t)}{k_B T}\right] \tag{5.4}$$

$$n_i(z,0) = \begin{cases} n_{e0} & \text{For } x \leq 0 \\ n_{e0}\exp(-x/L_p) & \text{For } x > 0 \\ 0 & \text{For } x > x_{max} \end{cases}$$

The electron density $n_e(z,t)$ has an initial value of n_{e0}, and a Boltzmann-like temperature distribution. The electron distribution is assumed to be in thermal equilibrium with the electrostatic potential for all times throughout the process. This is reasonable because the protons move slowly and the electrons can quickly rearrange themselves before the next time step. The initial proton distribution is given by n_{e0} inside the target ($x \leq 0$) implying charge neutrality which decays exponentially with a characteristic scale length, $L_p, (x > 0)$ and is zero beyond some chosen distance x_{max}. The exponential profile can be changed to a step-like profile, or have the HYADES rear scale length directly fed into the simulations. The protons are assumed to be at rest for all the density profiles at t = 0 (the start of the simulation).

Figure 5.10(a) shows the initial proton step density (dashed line) distribution at $t = 0$ and the calculated proton distribution (solid line). The energy as a function of distance at time $t = 150$ fs is given in Fig. 5.10(b). The initial electron and proton density was $n_e(t = 0) = n_p(t = 0) = 1 \times 10^{21} cm^{-3}$ with an electron temperature of $T_e = 1$ MeV. This electrostatic field accelerates protons from the undisturbed rear surface to a maximum proton energy of approximately 11 MeV. Typically, the ponderomotive potential is used to obtain the electron temperature, $k_B T = m_e c^2(\sqrt{1 + a_0^2/2} - 1) \cong 5.5$ MeV and the run time for the simulation, t, equals
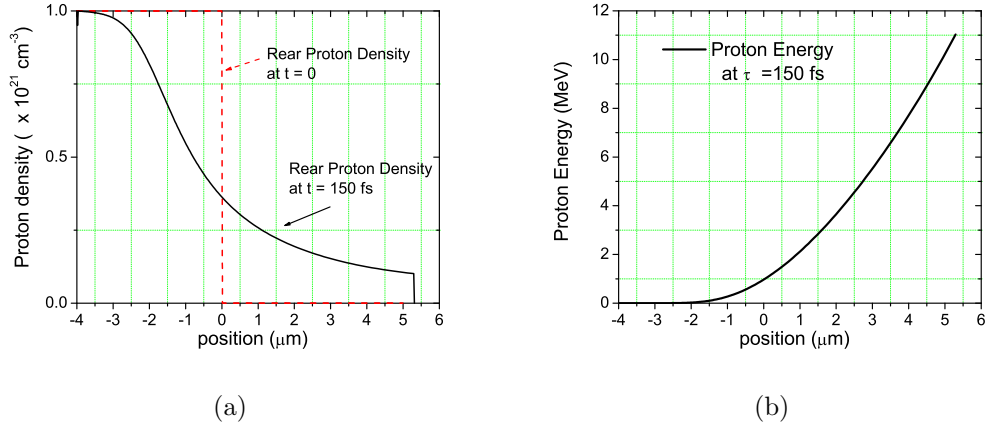
Figure 5.10: Proton density and energy time evolution assuming a $k_B T = 1$ MeV electron temperature from an (a) initial step-like proton density at $t = 0$, and $t = 150$ fs. (b) The corresponding proton energy in MeV at $t = 150$ fs as a function of position.

the pulse duration. In this thesis the measured electron temperature of $\sim$ 1 MeV was used in place of the ponderomotive energy because the ponderomotive assumption greatly differs from the experimental measurements. Using Mora's analytical equation,

$$E_{max} = \frac{1}{2} m_i v_f^2 \simeq 2 Z k_B T \left[\ln \left(\frac{\omega_{pp}\tau}{\sqrt{2 e_E}} + \sqrt{1 + \frac{\omega_{pp}^2 \tau^2}{2 e_E}} \right) \right]^2 \tag{5.5}$$

where ω_{pp} is the proton plasma frequency and τ is the laser duration, $\tau = 30\ fs$, one gets a reasonable value of 2.9 MeV for the maximum proton energy. This value is about half the measured proton energy from thick targets where the rear surface would have maintained its integrity.

To obtain an estimate of the acceleration time, τ_{acc}, the equation of motion given by

$$m_p \frac{d\mathbf{v}}{dt} = q\mathbf{E}(\mathbf{t}) \tag{5.6}$$

where the electric field $\mathbf{E(t)}$ is a function of time is assumed to take the form of a parallel plate capacitor which represents the electron and proton sheath.

$$E(t) = \frac{\sigma}{\varepsilon_0} = \frac{Q_{tot}}{A(t)\,\varepsilon_0}. \tag{5.7}$$

As shown experimentally and in PIC simulations the electron beam diverges with some angle θ thus causing the charge density σ to decrease as a function of time. Assume the area of the parallel plate capacitor as a function of time is given by

$$A(t) = (r_0 + v_{avg}t\tan(\theta))^2 \tag{5.8}$$

where r_0 is the starting size of the rear sheath and v_{avg} is the speed at which the sheath is propagating forward. The half angle θ was experimentally measured to be approximately 15° and $v_{avg} = \sqrt{k_B T/m_e}$ is the average electron velocity where $k_B T \cong 200$ keV was taken from the PIC simulations as shown in the next section. Combining Eqns. [5.6],[5.7],[5.8] one gets the following integral and solution,

$$v_p = \frac{Q_{tot}\,q}{m_p\,\varepsilon_0}\int_0^t \frac{dt}{(r_0 + v_{avg}\tan(\theta)\,t)^2} \tag{5.9}$$

$$v_p = \frac{Q_{tot}\,q}{m_p\,\varepsilon_0}\left[\frac{1}{v_{avg}\tan(\theta)r_0} - \frac{1}{(v_{avg}\tan(\theta))(r_0 + v_{avg}\tan(\theta)\,t)}\right]. \tag{5.10}$$

The total charge $Q_{tot} = n_e[cm^{-3}] \times depth \times \pi(r_0)^2$, where $r_0 = 1\ \mu m$ is the starting radius of the sheath, taken to be approximately the laser radius. The electron cloud is taken to be $2 \times$ the Debye length because the thickness of the sheath begins to smear out as it expands. $n_e[cm^{-3}] = 10^{21}$ was chosen as the electron density and approximately the density at the critical surface. Fig 5.11 shows the energy gain of a test proton within the expanding parallel plate capacitor model as described from Eqn. 5.10. Fig. 5.11 shows the acceleration time, τ_{acc}, is several times longer
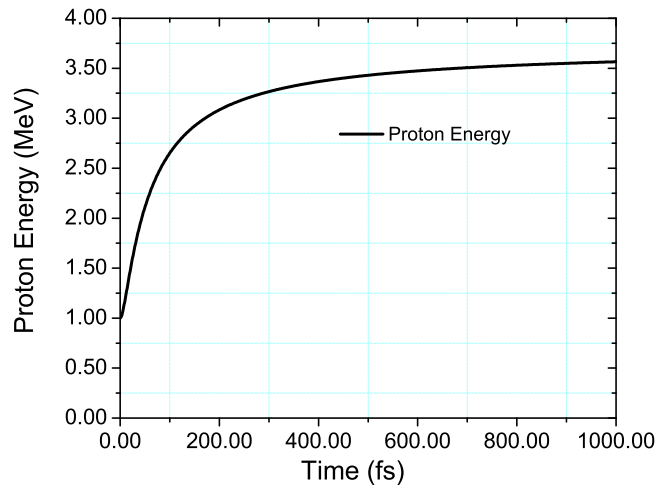
Figure 5.11: Proton energy as a function of time for an expanding parallel plate capacitor model. As the capacitor expands in the transverse direction the electric field decreases no longer accelerating the protons efficiently. The expanding parallel plate capacitor model shows the rear target sheath is maintained for several times the pulse duration.

than the pulse duration and after ∼200 fs the proton energy starts to saturate. Depending on the input variables the absolute number can vary but is approximately $\tau_{acc} = 5 \ \tau_{Laser}$ or 150 fs. For this reason, the acceleration time for the simulations in this section is assumed to be 150 fs. The capacitor model does not account for Q_{tot} as a function of time, since in real life the protons are moving across the capacitor and decreasing the potential. Therefore, this model calculates the energy of the first test proton to cross the capacitor. Eqn. 5.10 suggests Q_{tot} is a more important factor in determining the maximum proton energy then the average electron velocity given by $v_{avg} = \sqrt{k_B T / m_e}$.

Figure 5.12(a) shows the initial proton density gradient taken from the 50 nm Si_3N_4 HYADES simulation (dashed) (Fig. 5.9) for t = 0. The solid curve is the proton layer at time, t = 150 fs. The proton energy as a function of position, Fig. 5.12(b), shows a maximum proton energy of approximately 3.5 MeV. This value is
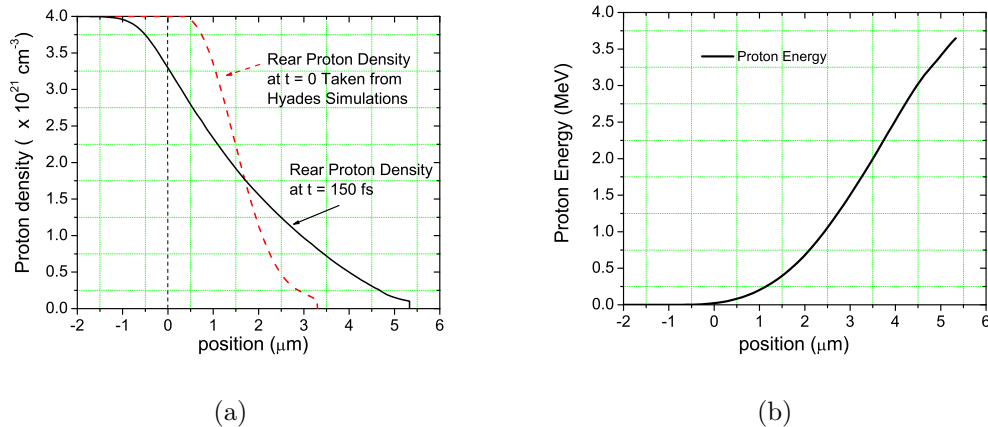
Figure 5.12: Proton density and energy time evolution assuming a $k_B T = 1$ MeV electron temperature and a starting density of taken from the 1-D HYADES simulations for 50 nm Si_3N_4 target. (a) 50 nm Si_3N_4 initial proton density at $t = 0$, and $t = 150$ fs. (b) Proton energy in MeV at $t = 150$ fs as a function of position

much lower than the maximum energy for the initial step-like proton density which produced 11 MeV. This is because the initial proton density gradient reduces the electric fields at the rear of the target. Although the total potential difference of the charge separation is the same, the potential decreases over a larger area because the gradient now does not have the large step density distribution. Therefore, the large proton scale length at the target's rear surface decreases the electric field which can consequently decreases the proton energy by a factor of two or more.

5.5   2D PIC simulations

The analysis of the presented proton acceleration experiments are supported by 2D particle-in-cell simulations based on the code REMP (relativistic electromagnetic particle) [102] mesh code based on particle-in-cell method. The acceleration of ions in high-intensity laser interaction with the thin solid dense target is studied using either an ultra-thin hydrogen foil or a two-layer aluminum-hydrogen foil. In the simulations

presented here the grid mesh size is $\lambda/200$, space and time scales are given in units of λ and $2\lambda/\omega$, respectively, where λ and ω, are the laser pulse wavelength and frequency respectively. The electron density of the foil is varied from 100 n_c - 400 n_c depending on the interaction conditions, where n_c is the critical density of the plasma. The interaction of the laser pulse with the foil is simulated on a grid with size of $(x, y) = (20\lambda, 10\lambda)$ and 16 particles per cell. The laser pulse is introduced at the left boundary and propagates along the x-axis, from left to right. The temporal and spatial profiles of the pulse are Gaussian. The following laser parameters were used in the simulations: laser power of 30 TW, pulse duration of 30 fs, spot size of 3 μm (FWHM). We performed simulations varying target thickness from l=0.01λ to l=1λ.

A two layer hydrogen foil is simulated to represent the hydrogen rich CH target. The first layer is 250λ thick and the electron density is 400 n_c. The second layer is assumed to be 0.05 λ thick and has an electron density of 50 n_c. This second lower density hydrogen layer simulates the rear surface proton contamination and is used for both hydrogen and aluminum simulations. THe two layer setup allows for particles to be independently tracked from both locations. The foil is placed at a distance of 5λ from the left boundary.

The two curves in Fig. 5.13(a) correspond to the protons accelerated from the first layer (squares) and the second layer or rear surface (circles). The incident laser pulse generates a charge separation due to the ponderomotive force pushing the electrons forward until the induced electrostatic field and the ponderomotive potential are balanced. The protons within the laser focal volume will experience the electrostatic field estimated to be $\sim a_0^2/2\gamma$ by Pukhov [86] and shown to be in good agreement in the presented simulations. The maximum longitudinal electrostatic field as a
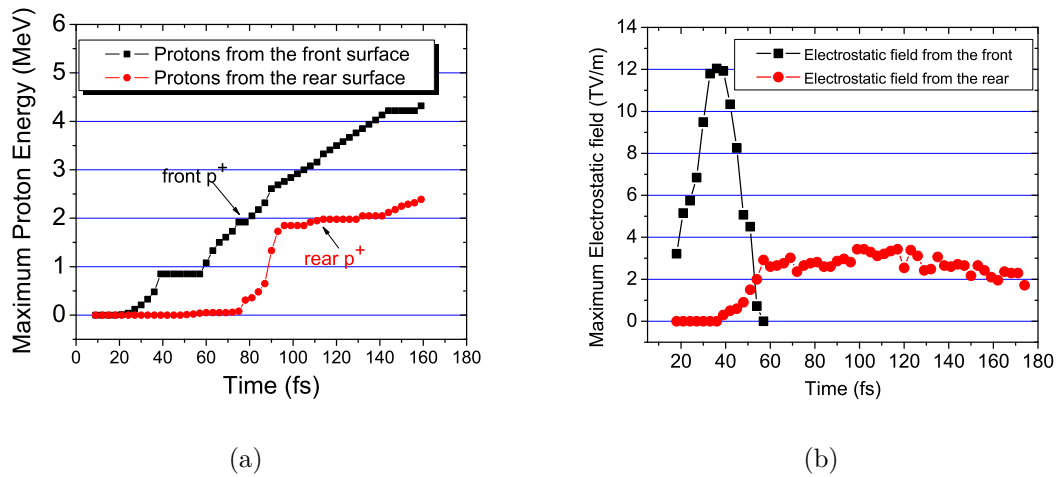
Figure 5.13: (a) PIC simulation results plotting the maximum proton energy at each time step from the first (front - squares) and second (rear - circles) layer of a 400 n_c hydrogen target irradiated with a 30 TW, 30 fs laser. Simulations show two distinct acceleration stages: first, a charge separation at the target front due to the laser ponderomotive force accelerates the protons to ~1 MeV. Second, the protons receive an additional acceleration due to the rear sheath which is maintained over several hundred femtoseconds. Non-hydrogen contain targets only benefit from the rear sheath. (b) PIC simulation results plotting the maximum electrostatic field at each time step from the first (front - squares) and second (rear - circles) layer.

function of time for front (squares) and rear (circles) protons is presented in Fig. 5.13(b) for a 0.35 λ thick two layer hydrogen foil. Fig.5.13(b) shows a strong quasi-electrostatic field rising as the laser arrives at the target front at around ~36 fs, which reaches a maximum value of ~12 TV/m when the laser peak intensity arrives. The electric field at the front of the target exists during the duration of the laser pulse and quickly drops to zero at around 60 fs. The protons, which are accelerated as a result of the front field, are accelerated over roughly 10 nm and propagate into the plasma bulk where they are no longer accelerated by the front sheath. The protons gain about 1 MeV of energy and do not acquire energy as they propagate through the target. Because the simulated target is thin (0.35 λ), a rear sheath field

begins to appear around 40 fs and further accelerates the front protons to ~4.5 MeV. The corresponding proton energy as a function of time is shown in Fig. 5.13(a) for both front (squares) and rear (circles) protons. The front protons gain energy from the front sheath but do not gain energy as they propagate through the target. At the rear surface the protons receive additional energy due to the rear sheath. The rear sheath has a lower field strength but the charge separation is maintained over a much longer time period ($\sim$ 150 fs, which is consistent with the expanding capacitor model). Also, the protons and rear sheath propagate forward together leading to a steady rise in the proton energy gain over time.
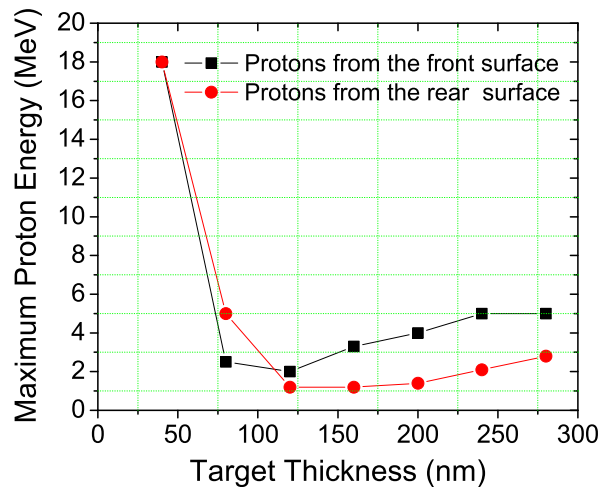
Figure 5.14: Simulation results showing the maximum proton energy as a function of target thickness. "Squares" show protons from the front surface, "circles" shows protons accelerated from the back surface. For targets 125 nm thick and greater the front protons are higher energy due to the two stage acceleration mechanism. The maximum proton energy decreases because the front and rear sheath begin to merge weakening both fields. Below 50 nm the front and rear target (30 TW skin depth ~55 nm) merge and the proton energy jumps 18 MeV.

Simulations of two layer hydrogen foils for varying target thicknesses were performed and qualitatively followed the above situation resulting in slightly different

proton energy values from the front and rear surfaces as shown in Fig. 5.14. It is shown as the target thickness decreases from 300 nm to ~120 nm, both the maximum energy from the front and rear protons decrease. As described above, for hydrogen containing materials the front protons have a higher maximum energy compared to the rear protons. This trend changes as the target thickness is decreased to ~100 nm and the rear proton become more energetic. For target thicknesses ~40 nm there is no clear distinction between the front and rear surface and they merge as the target thickness reaches the relativistic skin depth. This could explain why the maximum proton energy dips for 100 nm thick targets in the experiments.

The two sheath acceleration mechanism is always beneficial for the front protons. However, as the rear protons begin to move they are extracting energy and quenching the rear sheath. Therefore, the two sheath acceleration mechanism is most beneficial for target thicknesses between 200 nm - 600 nm. This is because the front protons encounter the rear sheath and extract energy from the sheath before the rear protons have a chance to do so allowing them to maximize their energy.

It is constructive to visualize the longitudinal fields created by the two charge separations at the front and rear surface. Fig. 5.15(a) shows the front sheath in units of a_0 at t = 36 fs, when the peak of the laser arrives. The front sheath strength is on the order of $a_0/2$ and exists only during the pulse duration. At that time, there is only a longitudinal field present at the target front and the rest of the target appears "transparent". Fig. 5.15(b) taken at t = 120 fs, shows much more structure in the rear longitudinal fields. The thin target is deformed due to the laser's pressure causing the target and rear sheath to move forward together. This was the basis of the expanding parallel plate capacitor model used in the above section to calculate the acceleration time. As time progresses, the rear sheath diverges causing the
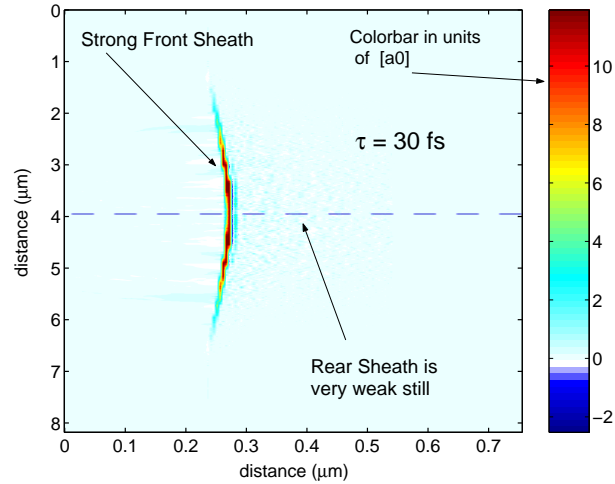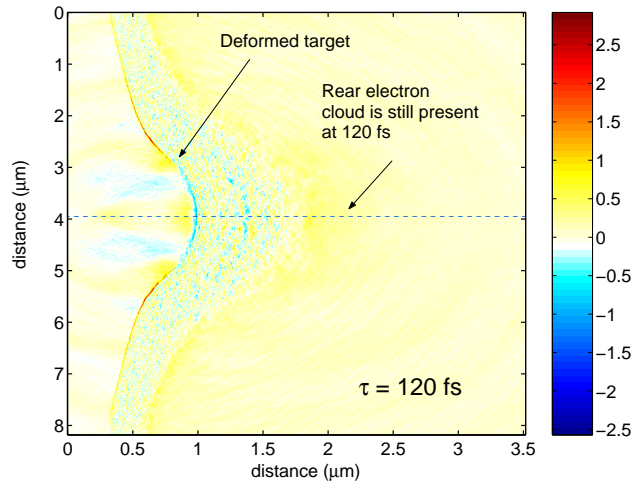
Figure 5.15: PIC simulation results showing the longitudinal electrostatic sheath at (a) 30 fs and (b) 120 fs. Long after the laser pulse has left the target the rear sheath is still present. As (b) shows the rear sheath is diverging and decreasing in strength but is still capable of accelerating protons for ~150 fs.

electrostatic field to decay until the protons can no longer extract energy. Depending on the conditions of the simulation this happens somewhere between 150 fs and 300 fs. Because the proton energy asymptotically approaches some maximum value, allowing the simulations run for 150 fs or 300 fs only changes the maximum energy by a few percent.

Assuming front surface protons are removed by the laser prepulse, the PIC simulations for Si_3N_4 targets follow the same mechanism. A front sheath is created by the ponderomotive force separating the electrons and ions, but because the front sheath exists for the laser duration the ions do not accelerate efficiently. There are no protons within the front sheath capable of being accelerated through the target. As with the hydrogen foil, the rear sheath is created which accelerates the protons from the back surface. Because the protons are starting from rest however, the maximum energy is approximately 2.5 MeV compared to 4 MeV from the hydrogen foil.

Lastly, turning to the electron momentum at 150 fs for a 300 nm hydrogen foil. It is observed in the PIC simulations that most of the electrons are within the target body and a very small percent of hot electrons are able to escape the target resulting in a positively charged foil. The electrons at the rear of the target are trapped due to the positively charged target and oscillate with an energy of approximately 200 keV, which was used on the expanding parallel plate capacitor model.

The PIC simulations are in good agreement with the experimental results. It is observed that the protons accelerated from hydrogen containing targets benefit from both the front and rear charge separations where non-hydrogen containing targets only benefit from the target rear sheath. The front sheath accelerates the protons giving them forward momentum to better extract energy from the rear sheath, thus producing higher energy. For non-hydrogen targets, the rear protons are starting from rest limiting the maximum energy gained.

5.6   Discussion/conclusions

The acceleration mechanism and origin of the most energetic laser generated protons is still debated. Previous experimental work along with simulations suggested

two possible acceleration mechanisms to explain the observed protons. They may originate from the laser irradiated front surface [35, 39, 103] or rear surface [40, 36]. PIC simulations by Pukhov [86] suggest it may be a combination of both mechanisms acting simultaneously.

It was shown that the maximum proton energy obtained from a high-intensity laser interacting with a solid target depends on the hydrogen content and the conductivity (metal vs. dielectic) of the target material. Thick ($>$ 1μm) Mylar and aluminum targets give approximately the same proton energy, however the conditions which create target normal sheath acceleration mechanism are different. For 1 μm thick hydrogen containing targets, the laser's ponderomotive potential isn't strong enough to accelerate front surface protons to the rear of the target before the rear protons begin to accelerate and reduces the rear sheath. In other words, the front protons may arrive at the rear surface too late when the sheath field is reduced and therefore cannot take full advantage of the two accelerating fields as explained above. The Al target produced similar energy compared to $>$1 μm Mylar, not because of a two sheath acceleration, but because the number of accelerated electrons in the Al target is larger thus creating a stronger rear sheath to pull the protons. It is clear from the data that the two stage acceleration mechanism is more pronounced as the target thickness is decreased. This is because the front protons can propagate completely through the ultrathin target and extract energy from the rear sheath before the rear protons begin to do so. Therefore, only thin targets benefit from the two sheath acceleration mechanism.

Turning now to the "thin" ($<$ 500 nm) Si_3N_4 and CH targets which show a clear distinction in the maximum proton energy and the two stage acceleration effect. In the thick non-hydrogen (Al) and hydrogen (Mylar) containing targets the distinction

was not clear because one was an opaque conductor and the other a transparent dielectric. However, for thin targets both are transparent dielectrics and the only major distinction is one has hydrogen and the other does not.

The electron divergence, direction, relative number, temperature, as well as the 3/2 harmonic were all measured and shown to be approximately the same for Si_3N_4 and CH targets. The only major difference is the maximum proton energy and the hydrogen content in the target materials. CH's chemical composition is roughly 60% hydrogen and Si_3N_4 only has hydrogen containing impurities on its surface. The maximum proton energy from the Si_3N_4 targets is about 2 MeV and does not change with target thickness. Whether the target thickness is 50 or 500 nm the maximum proton energy and divergence was measured to be the same.

Particle in cell simulations confirm two distinct acceleration stages for hydrogen containing targets: first, a charge separation at the target front due to the laser's ponderomotive force, and second, the generated target normal sheath acceleration (TNSA) mechanism. As discussed above, in order to take advantage of the two stage acceleration mechanism, the target should be thin enough which allows the front protons to reach the rear sheath and extract the most energy, but not too thin because the front and rear charge separations will begin to merge consequently weakening both sheaths. The front sheath is approximately the laser's skin depth $\delta = \sqrt{(\gamma)}c/w_p$ (approximately 15-50 nm thick for γ=1-10) and the rear sheath is generally quoted as the Debye length. Under ideal laser target conditions, meaning no prepulse or target deformation, PIC simulations show the charge separations begin to merge for targets ~ 100 nm thick. For such thin targets the two charge separations will merge for both H and non-hydrogen containing targets consequently weakening the rear sheath for both.

According to PIC simulations such ultrathin targets are capable of producing energy higher than the observed 2 MeV. However, such thin targets are extremely sensitive to any laser prepulses which cause both the front and rear surfaces to quickly deform. 50 nm thick Si_3N_4 were the thinnest targets capable of producing protons for the experimental conditions presented. The hydrodynamic code HYADES was used to assess the plasma conditions the peak laser pulse interacted with. The hydrodynamic simulation suggests the laser prepulse transforms thin targets into near critical density plasma clouds dramatically changing the interaction conditions and resulting in a lower maximum proton energy. The consequence of the rear surface deformation was analyzed using both PIC simulations and analytical arguments. Both showed the maximum proton energy can drop by 2 - 4 times depending on the specific conditions.

CHAPTER VI

Relativistic Plasma Shutter for Ultra-intense Laser Pulses

In the previous chapter proton generation experiments from solid targets were discussed. Cross polarized wave generation (XPW) was implemented on the HERCULES laser system giving an ASE contrast ratio of 10^{-11}, which was sufficient to generate proton beams from 50 nm dielectric targets. However, the experimental data along with simulations in the previous chapter showed the target was heavily distorted due to the leading edge of laser pulse and suggest the contrast ratio needs to be increased further.

In this chapter, a relativistic transmissive plasma shutter is proposed in order to improve the laser contrast and allow for proton generation from a 30 TW laser interaction with a 30 nm thick target. The relativistic plasma shutter consists of a thin foil placed in front of the target so that the leading edge of the laser pulse fully ionizes the foil. In order for the plasma shutter to be effective, the ablated foil must expand such that the peak electron density is greater than the non-relativistic critical density and less than the relativistic critical density. This plasma will transmit the high intensity peak pulse while rejecting the low intensity pedestal resulting in a significant increase in temporal contrast. When a clean, ultrahigh peak power laser

interacts with a very thin target (< 70 nm) the laser's ponderomotive force deforms the plasma causing the protons to be predominately accelerated toward the laser axis. The improved contrast is confirmed by measuring high energy protons at three different angles from target rear with and without a plasma shutter. Hydrodynamic and Particle-in-cell simulations (PIC) are used to explain the target deformation and proton direction.

6.1 Experimental setup

The experiment was performed using the Hercules laser system. The target consisted of two silicon nitride (Si_3N_4) foils of varying thickness (30 nm or 50 nm) separated by 20 μm. An f/2 off-axis parabolic mirror focused the 800 nm, p-polarized, 30 fs duration, laser pulse into a 3 μm FWHM focal spot diameter irradiating the front edge of the rear foil at a 20° angle of incidence. The peak intensity was 4×10^{20} W/cm^2 ($a_o = 0.85 \times 10^{-8}$ λ [μm] (I [W/cm^2])$^{1/2} = 13.6$) and approximately 2×10^{20} W/cm^2 on the shutter. The laser system had a $\sim 10\%$ shot-to-shot energy fluctuation. The calculated Rayleigh range of the parabola is about 25 μm. The ASE contrast, as measured by a third order autocorrelator, was 10^{-11}, allowing for the ASE intensity (10^9 W/cm^2) to be below the damage threshold for dielectric targets. However, the contrast measured from 30 ps to ~ 1 ps before the laser peak begins to degrade quickly from 10^{-11} to approximately 10^{-6}. Strips of Mylar filters on top of CR-39 track detectors were placed 10 cm behind the target to measure the maximum proton energy. In a separate measurement, the proton spectrum was measured at 0°, 10°, and 20° (laser axis) to the normal using a 2.5 cm long, 0.45 T magnetic spectrometer with a 120 μm diameter pinhole subtending 1.1×10^{-6} steradians.
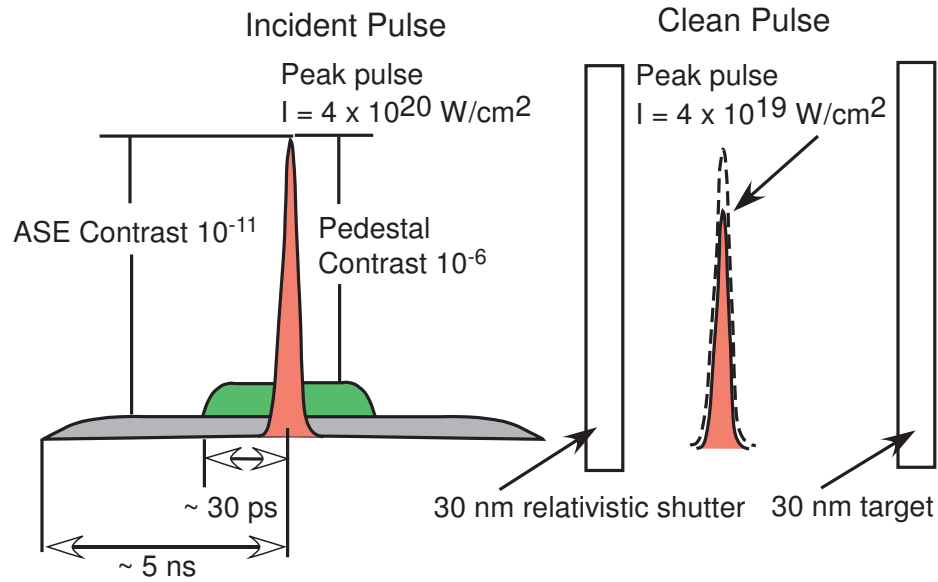
Figure 6.1: Schematic of the relativistic plasma shutter for ultra-intense laser pulses

6.2 Experimental results

6.2.1 Transmission

The thickness of the shutter was chosen based on experimental laser transmission data. For example, if 0% of the laser light was transmitted from a 100 nm shutter, than the target was still above the critical density when the peak pulse arrived. If a 100 nm shutter transmits ~100% of the laser energy, then the target was below the relativistic critical density allowing the laser to transmit through. The transmission data was measured by placing targets of varying thickness 20 μm before the laser focus. The laser light was captured using a parabolic mirror and the total transmitted energy was measured. For thicknesses of 200 nm and above, approximately 0% of the laser energy was transmitted, as shown in figure 6.3.

The transmission rises for 100 nm and 75 nm foils, were on average 6% and 40% of the laser energy respectively. As Fig. 6.3 shows, 50 nm thick targets varied widely in transmitted energy, ranging from ~ 5% to 95% transmission due to laser shot-to-shot
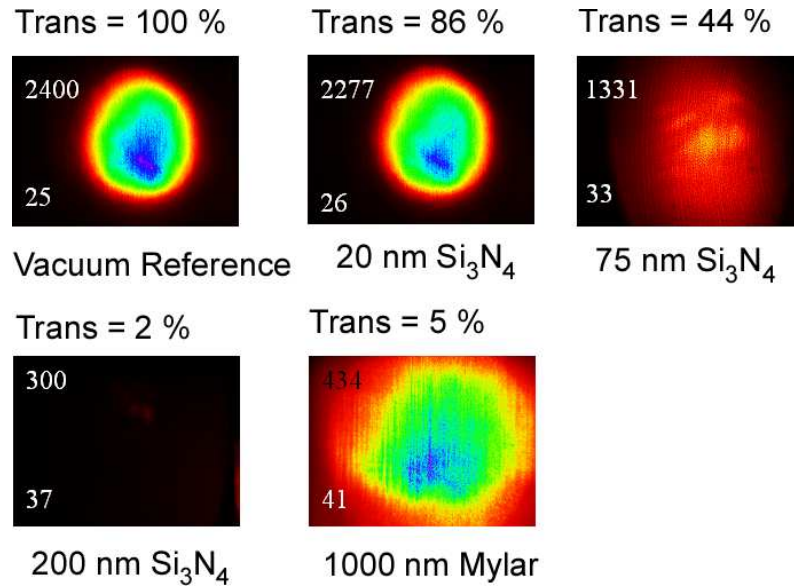
Figure 6.2: Raw laser transmission data imaged onto a CCD.
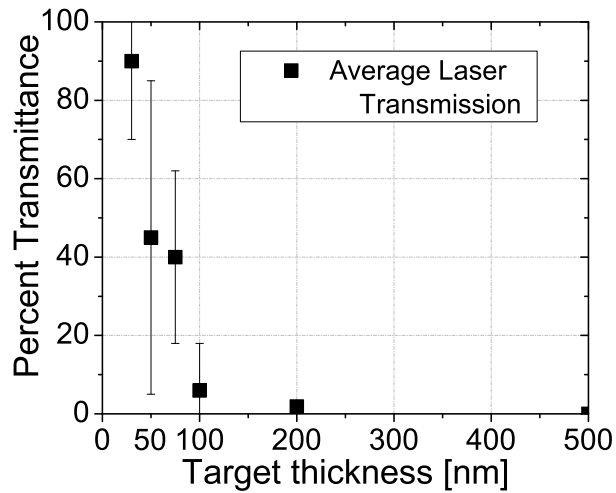
Figure 6.3: Percent transmission for Si_3N_4 foils of varying thickness placed 20 μm before the laser focus.

energy fluctuations. However, 30 nm targets consistently transmitted 70% to 99% of the laser energy, effectively removing between 1% and 30% of the laser's front edge. 30 nm targets were used as a shutter throughout the experiment. The non-relativistic critical density for 800 nm is $n_c = 1.72 \times 10^{21}$ cm^{-3}. For an $a_o = 13.6$ and linearly polarized laser light the time averaged gamma factor $< \gamma >= (1 + a_o^2/2)^{1/2} = 9.7$,

giving the relativistic critical density $n_{c\gamma} = 9.7n_c = 1.66 \times 10^{22}$ cm^{-3}.

Because Si$_3$N$_4$ is a transparent dielectric, the ASE pedestal is below the damage threshold and passes through the intact target. Consequently, the preplasma is caused by the leading edge of the laser "foot." According to hydrodynamic simulations, a peak density between 3-7 n_{cr}, which is between $n_{\gamma c}$ and n_c, is expected for a 0.5-1 mJ, 30 ps "foot" ablating a 30 nm Si$_3$N$_4$ target.

6.2.2   Proton spectrum

Figure 6.4 shows the proton spectrum measured at 0°, 10°, and 20° to the normal for 50 nm Si$_3$N$_4$ targets with and without a 30 nm shutter. The proton spectrum from the 50 nm Si$_3$N$_4$ target shows the highest energy protons are along the target normal direction, and fewer low energy protons are accelerated along the laser axis. The proton spectrum along the target normal axis shows a single temperature of 240 keV, fit using a Boltzmann distribution, $f(E) \sim \exp(-E/T_h)$, where E and T_h are the proton energy and temperature in MeV. Approximately 5×10^6 protons/MeV/str were generated at 2.25 MeV. The proton temperatures along 10° and 20° are 250 keV and 80 keV respectively.

The data clearly shows that when the shutter is inserted, the highest energy protons lie along the laser axis (20°) and exhibit a two temperature spectrum as shown in Fig. 6.4(b). The higher energy protons, which consist of protons above 0.6 MeV, showed a 30% increase in temperature to 340 keV, while the low energy protons show $T_{cold} = 82$ keV, similar to the 50 nm single target. The protons along the target normal have decreased in energy to about 0.75 MeV and yield a much lower proton temperature of 0.06 MeV. Although shot-to-shot variation may occur, the proton spectra exhibit a clear trend. Due to the 30 nm shutter, the protons move

away from the target normal direction toward the laser axis.

To further investigate this pulse cleaning technique, 30 nm targets were irradiated with and without a shutter. Because of the laser prepulse no single 30 nm thick Si_3N_4 target generated any detectable protons. However, by inserting the plasma shutter, 1.8 MeV protons were observed. The maximum proton energy observed from 30 and 50 nm targets with and without a 30 nm shutter is shown in Fig. 6.5. The 50 nm targets showed no significant increase in maximum proton energy by inserting the plasma shutter because of laser energy losses due to propagation through the shutter. Although the proton energy was similar the proton direction shifted toward the laser axis. The next section describes features of the laser plasma interaction observed in the experiment using hydro and PIC simulations.

(a)   (b)
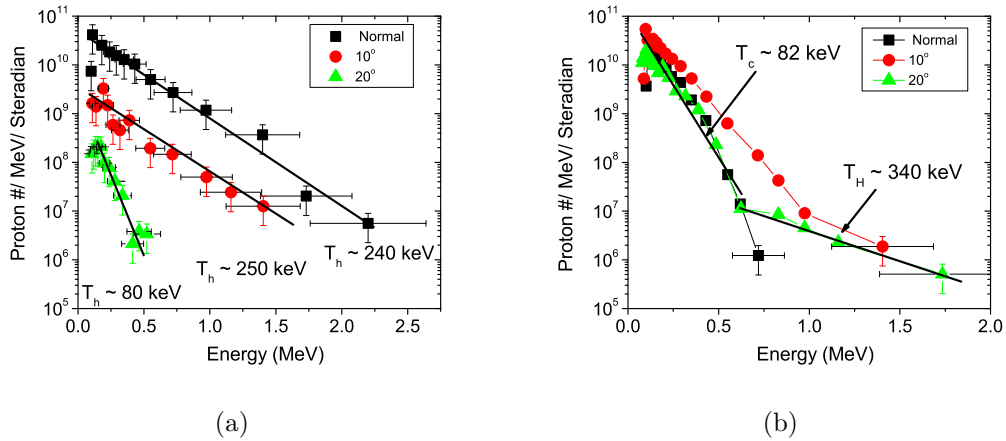
Figure 6.4: Proton beam energy spectrum from CR-39 detectors (a) without a 30 Si_3N_4 shutter and (b) with a 30 nm Si_3N_4 shutter placed in front of a 50 nm Si_3N_4 target. By inserting the shutter, the highest energy protons shift away from the target normal toward the laser axis which is characteristic of a high contrast laser solid interaction.
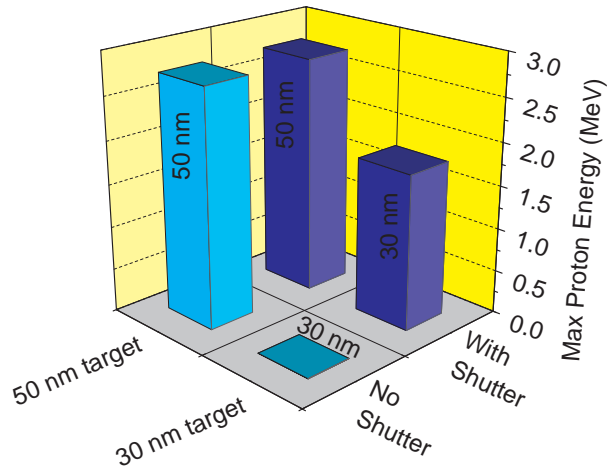
Figure 6.5: The four different cases with and without the 30 nm shutter in front of 50 nm and 30 nm targets. The bargraph shows that 30 nm targets alone generate no protons. By inserting the 30 nm shutter the 1.8 MeV protons are generated. The 50 nm targets does not benefit by inserting the 30 nm shutter and generates the same proton energy.

6.3 Hydrodynamic and PIC simulations

6.3.1 Hydrodynamic simulations

To understand this data it is convenient to separate the laser interaction into two stages. First, the laser prepulse ionizes the shutter creating a cloud of low density plasma expanding in front of the main interaction target. This is simulated using the 1-dimensional hydrodynamics code HYADES [101] in order to characterize the plasma conditions the high intensity peak pulse will experience. The second stage, which is studied using 2-D PIC simulations, tracks the main pulse propagating through the plasma shutter to characterize the laser pulse and then simulates the interaction with the main target.

The hydrodynamic simulation in figure 5.9, in section 5.3 shows the electron density in units of the non-relativistic n_c for Si_3N_4 targets of varying thicknesses. In

the simulations the targets were irradiated with an 800 nm, 1 mJ pulse ramping from 10^9 W/cm² to 10^{15} W/cm² over 30 ps, coming in at a 30 degree angle of incidence as in chapter 5.
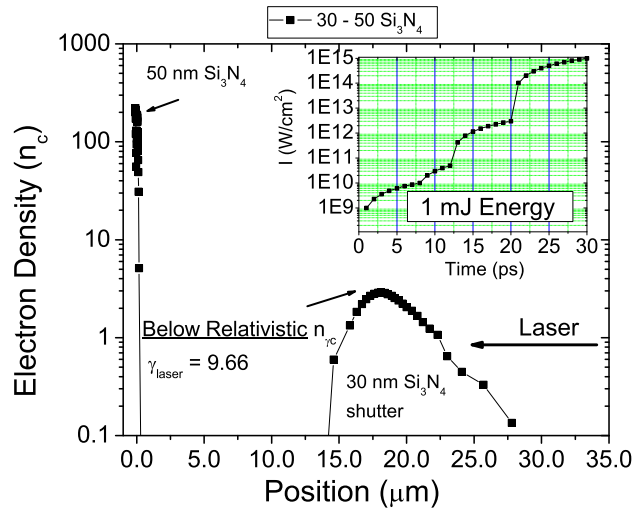
Figure 6.6: HYADES simulation results of the laser prepulse irradiating a 30 nm Si₃N₄ shutter placed 20μm in front of a 50 nm Si₃N₄ target. Insert shows the laser pulse used in the simulations which ramps from 1×10^9 W/cm² to 1×10^{15} W/cm² over 30 ps.

In order to reproduce Fig. 6.3 using the Hyades simulation, the laser foot used had between 1-3 mJ of energy. Based on these simulations it becomes clear that 50 nm targets is transformed into a $\sim$ 5 μm thick, $\sim 10n_c$ peak density cloud of plasma. When the peak laser arrives to interact with such conditions, the rear surface cannot deform and the protons consequently are accelerated along the target normal. To show that the integrity of the second target is maintained and not affected by the expanding shutter, a 30 nm and 50 nm foil placed 20 μm apart was also simulated using HYADES. As shown in Fig 6.6, after 30 ps, the 30 nm shutter has been transformed into a relativistically underdense plasma, and the 50 nm foil has started to heat up and expands from 50 nm to $\sim$ 70 nm with its peak electron

density decreased approximately 20% from 940 n_c (solid density = 3.44 g/cc) to 190 n_c. From this simulation it is observed that the vacuum gap separating the two foils is not breached by the expanding shutter and the second target is essentially intact.

6.3.2   2D PIC simulations

The PIC simulations were performed for two cases. First, the ideal case of the laser pulse interacting with a 70 nm thick target to illustrate what is expected during a clean interaction along with a simulation for a 3 n_c, 10 μm thick, 200 n_c density target which represents the laser interaction with an expanded shutter. As shown in the HYADES simulation, the rear 50 nm target expand from 50 nm to $\sim$ 70 nm due to the front shutter heating and so 70 nm was simulated for completeness. Second, the more realistic case, of the laser interacting with an expanded target due to the laser prepulse. In this case, the target is assumed to have an electron density of 10 n_c, which is above the relativistic critical density of the laser pulse, and 5 μm thick. All the target conditions used in the PIC simulations were taken from the Hyades simulations. As in chapter 5, the 2-D particle-in-cell simulations based on the code REMP [102], and the acceleration of ions in high-intensity laser interaction with the thin solid dense foils was studied by using a two-layer Silicon-hydrogen foil. The laser pulse is introduced at the left boundary and propagates along the x-axis, from left to right. The temporal and spatial profiles of the pulse are Gaussian. The following laser parameters were used in simulations: laser power of 30 TW, pulse duration of 30 fs, spot size of 3 μm (FWHM).

Fig. 6.7 show the electron density at different times as the laser pulse propagates though a 10 μm, 3 n_c plasma cloud. This cloud represents the 30 nm shutter which has expanded and decreased in peak density due to the laser prepulse. The plasma
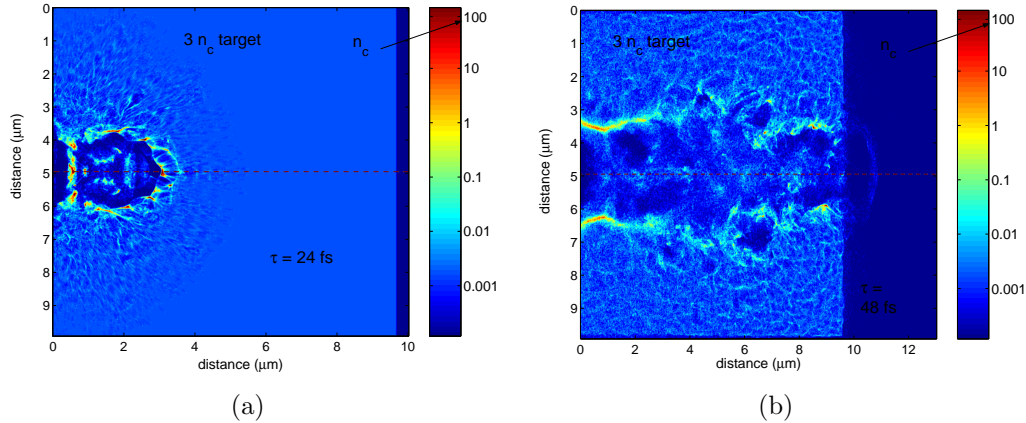
Figure 6.7: Results from 2D-PIC simulations. (a) and (b) show snapshots of the electron density at 24 fs and 28 fs respectively as the laser pulse is propagating through the 10 μm, 3 n_c plasma shutter. This simulation shows $\sim 90\%$ of the laser energy is transmitted through the shutter but the peak intensity decreases by approximately 10 times due to laser divergence.

density shown in the x-y plane is for a normal incident laser pulse. In the first snapshot Fig. 6.7(a) the laser enters from the left and a channel formation is seen due to the expulsion of electrons along the propagation axis. Fig. 6.7(b) is the electron density taken at a later time (t = 48 fs) when laser exits the low density cloud before it is focused on the primary target. The simulations show the laser pulse is guided and the peak intensity is maintained as it propagates through the 10μm plasma cloud. Because of the large separation distance of 20 μm it was not possible to simulate both the shutter and target together.

The following interaction scenario is observed for the 70 nm thick, 200 n_c peak density Si$_3$N$_4$ targets. As the peak intensity of the laser pulse enters the plasma, the laser's Gaussian spatial profile is imprinted upon the accelerated electrons which quickly propagate through the thin target. The time evolution of the targets density profile shows the laser ponderomotive force on the electrons accelerates them forward creating a charge seperation which then accelerate the ions to approximately 0.5 MeV per nucleon. The electrons being much lighter are accelerated immediately creating a
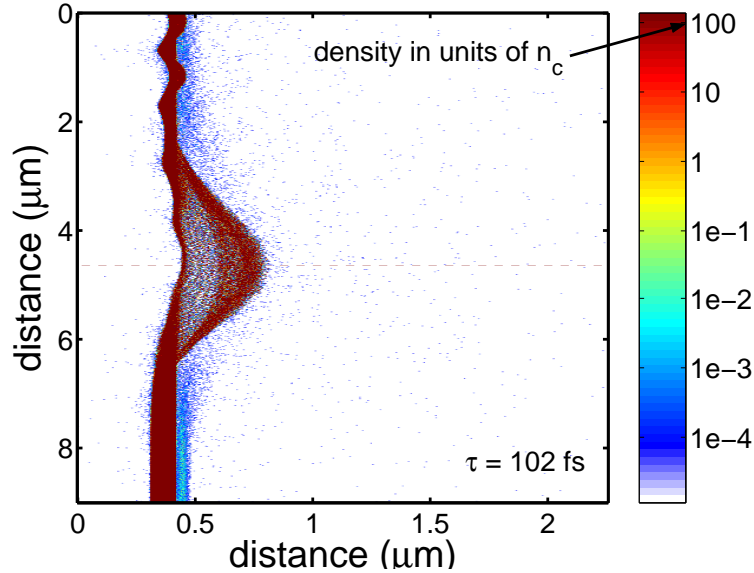
Figure 6.8: PIC simulation results of a 30 TW laser irradiating a 70 nm, 200 n_c, two-layer Si-H target showing the laser's Gaussian spatial profile imprinted upon the electrons and ions at t = 102 fs.

charge separation on the order of the laser's skin depth ($\sim$8 nm). The ions/protons are too heavy to respond quickly to the laser pulse, but show the imprint of the laser's spatial profile long after the laser has turned off. This consequence is observed because the target is so thin and is not capable of dissipating the spatial information before the target expands out. The Si ion density in Fig. 6.8 shows target deforming with a structure matching that of the laser pulse for a 70 nm thick targets at 102 fs.

The electric field due to the charge separation of electrons and ions continues to move as the protons acquire energy from the generated electrostatic sheath. However, target deformation is observed only for sufficiently thin targets. Fig. 6.9, shows the relative number of protons accelerated toward the laser axis direction as a function of target thickness for a 30^0 off normal incident laser. As the target thickness decreases, it becomes easier for the laser pressure to deform the rear surface which in turn directs the protons toward the laser axis. For targets approximately 100 nm thick, 30 TW lasers begin to easily deform the target thus shifting the protons toward the laser
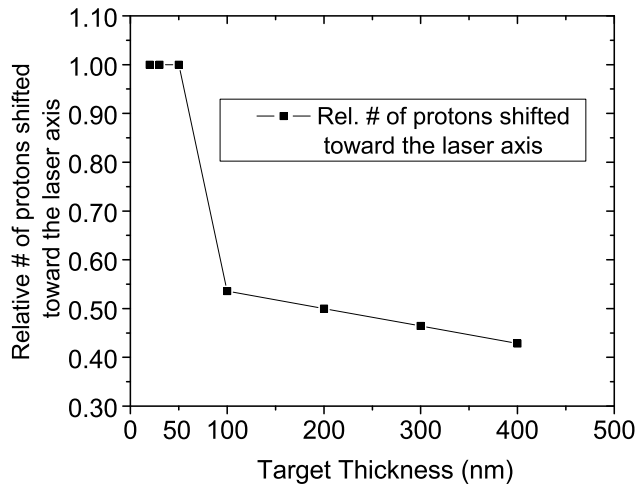
Figure 6.9: PIC simulation results showing the relative number of protons directed toward the laser as axis as a function of target thickness. The simulations were performed using a 30 TW laser incident at 30^0 off normal.

axis. As shown in the Fig. 6.9 the proton deflection angle quickly saturates because the once the target rear surface matches the lasers spatial profile the thinner targets will do the same.

The second case describes the single 50 nm Si_3N_4 target interaction which expanded several microns due to the laser prepulse. After the target expands it is thick enough to maintain the integrity of the targets rear surface. This causes the sheath accelerated protons to be directed along the target normal direction. Fig. 6.10(a) shows the proton deflection angle for 10 n_c, 5 μm thick two-layer Silicon-hydrogen target is along the target normal direction. 10 n_c is above the relativistic critical density for the laser intensity used in the experiments. The simulations show the protons are accelerated normal to the targets rear surface because target deformation cannot happen for such thick targets which is consistent with the experimental results. The protons accelerated from the 50 nm target alone are direction along the target normal. Fig. 6.10(b) shows the maximum proton energy for such thick target

conditions is approximately several MeV.

(a)   (b)
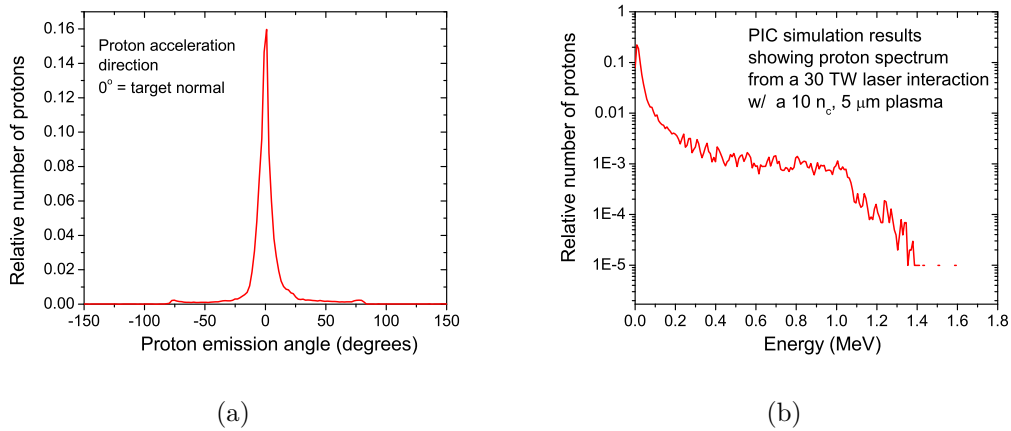
Figure 6.10: PIC simulation results showing a 30 TW laser interaction with a $10n_c$, 5 μm thick two-layer Si-H target. (a) The proton acceleration angle where 0^0 is normal to the target. And (b) the energy spectrum.

The experimental results suggest the plasma shutter did improve the laser contrast resulting in maximum proton energy of $\sim$2 MeV, which is consistent with experiments performed with two plasma mirrors with similar power [104]. Also, the proton energy was the same with and without the plasma shutter. In order to explain this effect, a lineout of the transmitted laser pulse from the 30 nm shutter is shown in Fig. 6.11.

Because the plasma density is below the relativistic critical density a large percent of the laser energy exits the plasma shutter ($\sim 90\%$), and the laser pulse profile does not degrade as it propagates though the plasma due to self focusing. As a reference, Fig. 6.11(a) shows the 30 TW laser pulse coming to a focus on the front side of the 3 n_c, 10 μm thick plasma shutter before the laser interacts with the target. In the absence of a target the electric field in the laser focus is a_0=35. Fig. 6.11(c) shows a $\sim$2 μm thick plasma channel formed by the laser pulse and gives a slightly higher a_0=36.87 indicating a small degree of self focusing and confirming the peak intensity
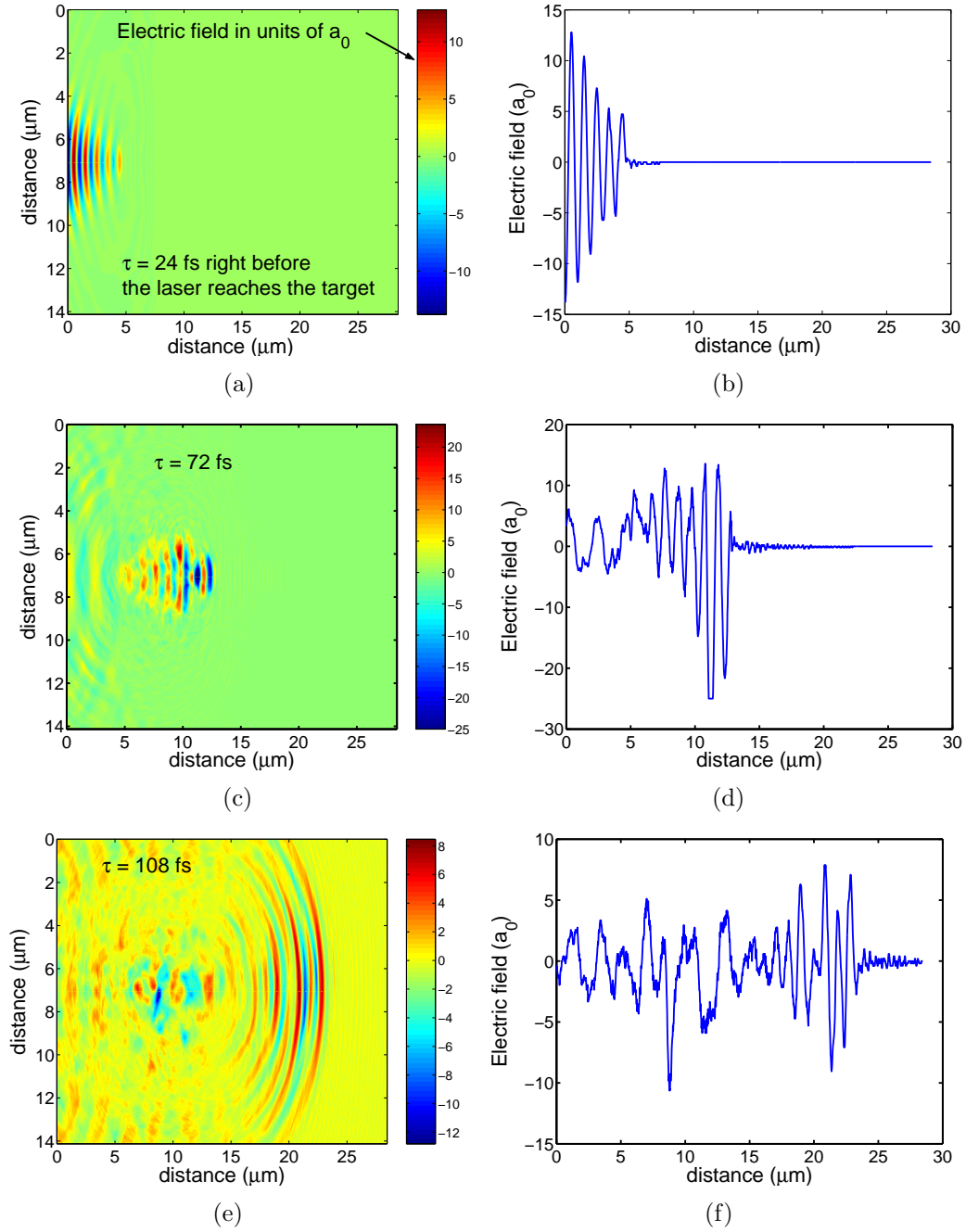
Figure 6.11: PIC simulation results showing the high intensity laser temporal profile before ((a),(b)-lineout) and after ((c),(d)-lineout) passing through the 10 μm 3 n_c plasma shutter. After passing through the plasma cloud the peak intensity laser has decreased by $\sim$10 times.

of the laser is maintained through the plasma shutter. However, Fig. 6.11(e) shows the peak intensity of the laser decreased by a factor of 10, after propagating an

additional 10 μm from the back of the plasma shutter, which is where the target was placed. Assuming the same effect also takes place in the real experiment, and the laser intensity decreased to $\sim 10^{19}$ W/cm^2 this may explain why the 30 nm - 50 nm double target resulted in protons with energy of 2 MeV. Its important to point out, in the real experiment the target position can be optimized and placed closer to the plasma shutter where the peak laser intensity is maintained.

6.4 Discussion/conclusions

After the insertion of the 30 nm shutter two important results were experimentally observed. First, the proton beam's direction shifted from the normal axis toward the laser axis signifying target deformation due to the laser light pressure. In the target normal sheath acceleration regime the protons are accelerated normal to the targets rear surface. If the target experiences a deformation, due to the laser pulse, the proton beam will replicate the structure always propagating normal the target's rear surface. As the PIC simulations showed, the laser pressure will deform a thin target, but this can only happen if the contrast is sufficiently high. It was shown that the peak intensity was maintained as the pulse propagated through a plasma cloud to reach the primary target. However, immediately after exiting the plasma channel, the laser pulse quickly diverged thus decreasing the peak intensity. Although the total transmitted energy is $\sim$80%, the intensity dropped by an order of magnitude to $\sim 10^{19}$ W/cm^2. The second result was a 30 nm shutter in front of a 30 nm target produced 1.8 MeV protons while no protons were detected for a 30 nm target alone.

The results of this chapter have important implications in understanding ultra-high intensity interactions with ultrathin foils. Hydrodynamics simulations showed that a 50 nm thick single target was converted to a near critical density plasma which

expanded several microns in thickness before the main pulse arrived. The relativistic plasma shutter technique is simple to implement and scaleable as the laser power is increased. Use of this technique requires a detailed knowledge of the laser prepulse parameters in order to optimize the laser contrast. Ultimately, one could "shape" the profile of the plasma shutter to suit the needs of the experiment, for example density tapering in the transverse direction to counter filamentation [105].

CHAPTER VII

Conclusions

7.1 Summary

This thesis presents the experimental data studying particle acceleration from high intensity laser plasma interactions. The first set of experiments reports on the production of quasi-monoenergetic electrons with energy up to 320 MeV with a 10 mrad angular divergence by focusing a 40 TW, 30 fs laser with an intensity of 10^{19} W/cm^2 onto a supersonic He gas jet. The experiment demonstrates how the electron beam energy scales as a function of plasma density. The electron beam energy is shown to be controlled by changing the plasma density and ranges between 80 MeV to 120 MeV for plasma densities between $n_e = 3.5 \times 10^{19}$ to 2×10^{19} cm^{-3}. 320 MeV electrons were generated from a lower electron density ranging between $n_e = 1.5 \times 10^{19}$ to 1.8×10^{19} cm^{-3}. Finally, the quasi-monoenergeic electron beams with energy between 100-150 MeV and charge of 0.5 nC were used to perform photonuclear activation of C and Cu and photofission of natural uranium. The electron beams generated by wakefield acceleration are been shown to be more effective in producing high energy γ-rays (tens of MeV) which lie within the giant dipole resonance energy than compared to previous experiments. By using quasi-monoenergetic electrons the radioisotope production rates increases by one to two orders of magnitude per Joule

of laser energy.

The second group of experiments investigated laser driven proton acceleration from submicron targets using high intensity (4×10^{20} W/cm^2), high contrast (10^{-11}) laser pulses. This contrast level was achieved by implementing XPW at the front end of the Hercules laser system. The maximum proton energy generated from ultra-thin targets has been shown to depend on the hydrogen content of the target material and not on the targets thickness up to several microns. The two stages of acceleration observed in PIC simulations was experimentally distinguished through target selection. It was observed that the maximum proton energy for hydrogen containing targets such as Mylar and CH was two times higher than for non-hydrogen containing targets such as Si_3N_4. For thin hydrogen containing targets the protons are accelerated first by charge separation created by the pondermotive potential, propagate through the target body and receive additional acceleration due to the rear sheath, whereas Si_3N_4 only receives TNSA thus yielding lower proton energy. Hydrodynamic simulations confirmed that thin targets are easily deformed by the foot of the laser pulses creating drastically different target conditions than expected. HYADES simulations showed for the parameters of the Hercules pulse shape a 50 nm target creates a 5 μm plasma cloud with a peak electron density of ~ 10 n_c with a large ion density gradient at the rear surface resulting in a weak field rear sheath, thus dropping the proton energy to $\sim$2 MeV.

Finally, a relativistic plasma shutter technique was proposed and tested to further increase the laser contrast. The shutter consists of a thin solid placed 20 μm before the target. As leading edge of the laser fully ionizes the foil it will expands into an underdense plasma allowing for the peak pulse to propagate through it. In the described experiment this technique was used to suppress the picosecond laser pre-

pulse thus creating a sharp interface for proton acceleration, however the technique could be to any experiment of interest. PIC simulation show that a high intensity ($> 10^{20}$ W/cm^2), ideal laser pulse strongly deforms a thin target (< 70 nm) causing the accelerated protons to shift away from the target normal and towards the laser axis. This characteristic effect was observed when the shutter was inserted before a 50 nm target. The protons accelerated from the 50 nm target alone propagated toward the target normal direction indicating rear surface target deformation did not take place. This effect was confirmed when 30 nm target with a 30 nm shutter produced 1.8 MeV protons, but when irradiated alone, didn't produce any detectable proton signal.

In prospect, the characteristics and capabilities of laser particle accelerators are encouraging. They are often compared to the large scale conventional accelerators which have been in development for over 60 years. In 50 years from now, it is foreseeable that small scale laser accelerators will play a significant role in both scientific research and practical applications.

7.2 Future Research

7.2.1 Electron acceleration and capillary discharge

Experiments on electron acceleration presented in this thesis showed electrons with energies greater than 300 MeV can be produced by focusing a 40 TW laser onto a supersonic He gas jet. Future experiments will attempt to increase the electron beam stability, energy, and charge. In order to generate electron beams with better stability and higher energy, one must decrease the plasma density and increase the interaction length allowing electrons to be accelerated over a longer distance. This can be done by using a gas filled [106, 107] or ablative capillary discharge [108] to

guide the high intensity laser pulse. Recently, Leemans *et al.* [109] demonstrated electron beams accelerated to 1 GeV using a 40 TW peak power laser and 3.3 cm gas-filled capillary discharge waveguide. By decreasing the input laser intensity, nonlinear effects such as wavebreaking and filamentation can be reduced, allowing for the production of a stable wakefield structure. The combination of a stable wakefield within a capillary tube, along with an external injection of electrons, could generate stable, high energy, quasi-monoenergetic energy spread, high charge electrons beams.

There are many possible applications for such electron beams. One of particular importance to homeland security is using the electron beam to generate γ-rays for photonuclear resonance excitation of explosive or radioactive materials. Currently, security concerns regarding the contents of airport luggage, among other things, are increasing the demand for inspection technology. X-ray screening only allows the shape of objects to be observed, and is limited in penetration depth due to the low X-ray energy. If the explosive material is molded into common shapes, such as toys, they will not be detected with conventional X-ray security screening.

Nuclear based detection methods, such as nuclear resonance fluorescence (NRF) imaging, have the ability to detect explosives and radioactive material by identifying their elemental composition. All nuclei have unique characteristic energy states, most of which are found below 7 MeV. When in an excited energy state, the nucleus will subsequently decay by the emission of photons in all directions with a signal specific to the nuclear isotope. Therefore, by using a γ-ray beam with a continuous energy distribution, photons at all energies will be present, ensuring excitation. This will provide an immediate and complete identification of the isotopes in the sample.

There are two necessary parameters for this detection system to be effective. First, a highly collimated, large number of γ-rays are needed in order to increase the

number of nuclear excitation events. NRF resonances have very high cross-sections ranging from 1 - 500 barns [66], which correspond to a ~5% - 99% probability of a scattering event. Uranium, for example, has a very high probability of nuclear excitation. If one assumes $\sim 10^{10}$ incident γ-rays upon a sample, and a natural linewidth of approximately 30 meV, the result will be $\sim 10^2$ resonance fluorescence photons radiating in 4π steradian. Assuming a 3×3 cm^2 area high resolution germanium detector placed 1 m away, one would detect about $\sim 10^{-2}$ photons, about five orders of magnitude too low. The second necessary parameter is that the γ-ray beam has a high repetition rate. If a γ-ray beam with a 3 mm diameter is incident upon a 1 square foot briefcase for example, it would take approximately 2000 shots to scan the entire area. Currently, laser accelerated electrons can be produced at approximately 10 Hz, resulting in a ~3 minute scan time.

In summary, laser wakefield accelerated electron beams can be enhanced in energy, charge, and stability by using a capillary waveguide along with an external electron injection into the wakefield. One possible application of such electron beams is their use in nuclear resonance fluorescence production to identify potentially hazardous materials.

7.2.2   Protons acceleration to therapeutic energies (130 MeV)

As discussed in this thesis the dominate mechanism involving proton acceleration from intense laser-solid interactions was the target normal sheath acceleration (TNSA) mechanism. Proton acceleration from micron thick foil targets is a result of the large, hundreds of GV/m electrostatic fields produced from the charge separation of the hot electrons and ions. The ponderomotive force of such ultrahigh intensities push the electrons forward with relativistic velocities (~MeV) while the heavier ions

remain relatively stationary, creating a charge separation which accelerates the ions out of the target.

When a high contrast, high power laser pulse (> 500 TW) interacts with a sub-micron solid target it ionizes the target in less than one optical period thus maintaining the integrity of the overdense plasma. For sufficiently thin targets the lasers ponderomotive force expels the electrons from the target with a transverse dimension on the order of the laser spot size resulting in a net positive charge region. If the energy of the laser accelerated electrons is large enough to overcome the Coulomb attraction of the positive ion region, than the electrons will not return resulting in ion acceleration in the "Coulomb exposition" regime. In terms of the dimensionless electromagnetic vector potential $a_0 = 0.85(\text{I } [\text{W/cm}^2] \ \lambda^2[\mu\text{m}] \ 10^{-18})^{1/2}$ in order to expel all the electrons and achieve the Coulomb explosion regime the following condition must be satisfied

$$a_0 > \pi^2 \frac{N_e}{n_c} \frac{l}{\lambda} \tag{7.1}$$

where N_e is the electron density, n_c is the plasma critical density, c is the speed of light, l is the foil thickness, and λ is the laser wavelength.

2D PIC simulations are used to study the acceleration of ions in high-intensity laser interaction with the thin solid dense foils is studied by using an ultra-thin two-layer aluminum-hydrogen foil. The aluminum and hydrogen layers are characterized by their thickness L_{Al}, L_H and the transverse size D_{Al}, D_H correspondingly. The transverse size of the Al layer is $D_{Al}=10\lambda$, and of the hydrogen layer is $D_H=3\lambda$. The proton energy spectrum from the interaction of a 500 TW laser pulse focused (f/D=1.5, focal spot 1.2 λ, FWHM) onto a thin double-layer foil ($L_{Al}=0.2\lambda$, $L_H=0.05\lambda$) illustrates a sharp maximum around 130 MeV with energy spread of
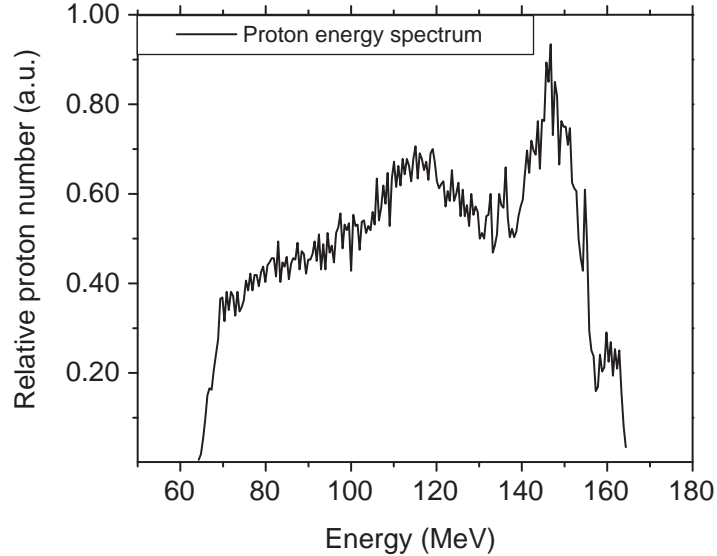
Figure 7.1: The protons energy spectrum from a PIC simulation of a 500 TW laser pulse interacting with a double-layer target demonstrating a proton energy peak above 100 MeV

$\Delta E/E \approx 5\%$ (Fig. 7.1). The simulations show that the heavy ions are accelerated along the laser direction and, due to their repulsive field, inject a thin layer of protons into the laser pulse for direct laser acceleration. The 130 MeV monoenergetic nature of the generated proton beam demonstrates double layer targets are advantageous for proton therapy in the direct Coulomb explosion regime.

In summary, ultrahigh-intensity lasers (10^{22} W/cm^2) offer a unique condition to conduct particle acceleration; however high peak power lasers (TW-PW) have temporal prepulses above the material damage threshold. 2D PIC simulations have shown that such high-intensity, high contrast, short-pulse lasers are capable of accelerating proton beams to quasi-monoenergetic energies above 100 MeV.

BIBLIOGRAPHY

BIBLIOGRAPHY

[1] S. P. D. Mangles, C. D. Murphy, Z. Najmudin, A. G. R. Thomas, J. L. Collier, A. E. Dangor, E. J. Divall, P. S. Foster, J. G. Gallacher, C. J. Hooker, D. A. Jaroszynski, A. J. Langley, W. B. Mori, P. A. Norreys, F. S. Tsung, R. Viskup, B. R. Walton, and K. Krushelnick. Monoenergetic beams of relativistic electrons from intense laser-plasma interactions. *Nature*, 431:535, 2004.

[2] C. G. R. Geddes, C. Toth, J. van Tilborg, E. Esarey, C. B. Schroeder, D. Bruhwiller, C. Nieter, J. Cary, and W. P. Leemans. *Nature*, 431:538, 2004.

[3] J. Faure, Y. Glinec, A. Pukhov, S. Kiselev, S. Gordienko, E. Lefebvre, J.-P. Rousseau, F. Burgy, and V. Malka. A laser-plasma accelerator producing monoenergetic electron beams. *Nature*, 431:541, 2004.

[4] A. Maksimchuk, S. Reed, N. Naumova, V. Chvykov, B. Hou, G. Kalintchenko, T. Matsuoka, J. Nees, P. Rousseau, G. Mourou, and V. Yanovsky. Energy scaling of quasi-monoenergetic electron beams from laser wakefields driven by 40 TW ultrashort pulses. *Appl. Phys. B: Lasers and Optics*, 89:201, 2007.

[5] A. Pukhov and J. Meyer-ter Vehn. Laser wake field acceleration: the highly non-linear broken-wave regime. *Applied Physics B - Lasers and Optics*, 74(4-5):355, 2002.

[6] K. Boyer, T. S. Luk, and C. K. Rhodes. Possibility of optically induced nuclear fission. *Phys. Rev. Lett.*, 60(7):557, 1988.

[7] M. H. Key, M. D. Cable, T. E. Cowan, K. G. Estabrook, B. A. Hammel, S. P. Hatchett, E. A. Henry, D. E. Hinkel, J. D. Kilkenny, J. A. Koch, W. L. Kruer, A. B. Langdon, B. F. Lasinski, R. W. Lee, B. J. MacGowan, A. MacKinnon, J. D. Moody, M. J. Moran, A. A. Offenberger, D. M. Pennington, M. D. Perry, T. J. Phillips, T. C. Sangster, M. S. Singh, M. A. Stoyer, M. Tabak, G. L. Tietbohl, M. Tsukamoto, K. Wharton, and S. C. Wilks. Hot electron production and heating by hot electrons in fast ignitor research. *Phys. Plasmas*, 5(5):1966, 1998.

[8] M. S. Smith and K. E. Rehm. Physics of a rare isotope accelerator. *Rev. Nucl. Part. Sci.*, 51:91, 2001.

[9] A. D. Vanture, D. Zucker, and G. Wallerstein. *Astrophys. J.*, 514:932, 1999.

[10] G. D. Alton and J. R. Beene. The Holifield radioactive ion beam facility at the oak ridge national laboratory: Present status and future plans. *J. Phys. G: Nucl. Part. Phys.*, 24(8):1347, 1998.

[11] M. Roth, T. E. Cowan, M. H. Key, S. P. Hatchett, C. Brown, W. Fountain, J. Johnson, D. M. Pennington, R. A. Snavely, S. C. Wilks, K. Yasuike, H. Ruhl, F. Pegoraro, S. V. Bulanov, E. M. Campbell, M. D. Perry, and H. Powell. Fast ignition by intense laser-accelerated proton beams. *Phys. Rev. Lett.*, 86(3):436, 2001.

[12] M. Borghesi, D.H. Campbell, A. Schiavi, O. Willi, A.J. Mackinnon, D. Hicks, P. Patel, L.A. Gizzi, M. Galimberti, and R.J. Clarke. Laser-produced protons and their application as a particle probe. *Laser and Particle Beams*, 20(2):269, 2002.

[13] M. Borghesi, P. Audebert, S.V. Bulabov, T. E. Cowan, J. Fuchs, J.C. Gauthier, A.J. Mackinnon, P.K. Patel, G. Pretzler, L. Romagnani, A. Schiavi, T. Toncian, and O. Willi. High-intensity laser-plasma interaction studies employing laser-driven proton probes. *Laser and Particle Beams*, 23(3):291, 2005.

[14] R. R. Wilson. Radiological use of fast protons. *Radiology*, 47(5):487, 1946.

[15] E. S. Sarachik and G. T. Schappert. Classical theory of the scattering of intense laser radiation by free electrons. *Phys. Rev. D*, 1(10):2738, 1970.

[16] P. Gibbon. *Short Pulse Laser Interactions with Matter - An Introduction.* Imperial College Press, London, 2005.

[17] G. S. Sarkisov, V. Yu. Bychenkov, V. N. Novikov, V. T. Tikhonchuk, A. Maksimchuk, S. Y. Chen, R. Wagner, G. Mourou, and D. Umstadter. Self-focusing, channel formation, and high-energy ion generation in interaction of an intense short laser pulse with a he jet. *Phys. Rev. E*, 59(6):7042, 1999.

[18] A. B. Borisov, A. V. Borovskiy, O. B. Shiryaev, V. V. Korobkin, A. M. Prokhorov, J. C. Solem, T. S. Luk, K. Boyer, and C. K. Rhodes. Relativistic and charge-displacement self-channeling of intense ultrashort laser pulses in plasmas. *Phys. Rev. A*, 45(8):5830, 1992.

[19] G. Z. Sun, E. Ott, Y. C. Lee, and P. Guzdar. Self-focusing of short intense pulses in plasmas. *Phys. of Fluids*, 30(2):526, 1987.

[20] T. Tajima and J. M. Dawson. Laser electron accelerator. *Phys. Rev. Lett.*, 43(4):267, 1979.

[21] E. Esarey, P. Sprangle, J. Krall, and A. Ting. Overview of plasma based accelerator concepts. *Plasma Science, IEEE Transactions on*, 24(2):252, 1996.

[22] J. M. Dawson. Nonlinear electron oscillations in a cold plasma. *Phys. Rev.*, 113(2):383, 1959.

[23] E. Esarey and M. Pilloff. Trapping and acceleration in nonlinear plasma waves. *Phys. Plasmas*, 2:1432, 1995.

[24] A. I. Akhiezer and R. V. Polovin. Trapping and acceleration in nonlinear plasma waves. *Sov. Phys. JETP*, 3:696, 1956.

[25] W. Lu, M. Tzoufras, C. Joshi, F. S. Tsung, W. B. Mori, J. Vieira, R. A. Fonseca, and L. O. Silva. Generating multi-GeV electron bunches using single stage laser wakefield acceleration in a 3D nonlinear regime. *Phys. Rev. ST Accel. Beams*, 10(6):061301, 2007.

[26] D. Strickland and G. Mourou. Compression of amplified chirped optical pulses. *Optics Communications*, 56(3):219, 1985.

[27] W. L. Kruer. *The Physics of Laser Plasma Interactions*. Westview Press, 1988.

[28] S. C. Wilks and W. L. Kruer. Absorption of ultrashort, ultra-intense laser light by solids and overdense plasmas. *IEEE J. Quantum Electron.*, 33(11):1954, 1997.

[29] F. Brunel. Not-so-resonant, resonant absorption. *Phys. Rev. Lett.*, 59(1):52, 1987.

[30] F. Brunel. *Phys. of Fluids*, 31(1):2714, 1988.

[31] M. I. K. Santala, M. Zepf, I. Watts, F. N. Beg, E. Clark, M. Tatarakis, K. Krushelnick, A. E. Dangor, T. McCanny, I. Spencer, R. P. Singhal, K. W. D. Ledingham, S. C. Wilks, A. C. Machacek, J. S. Wark, R. Allott, R. J. Clarke, and P. A. Norreys. Effect of the plasma density scale length on the direction of fast electrons in relativistic laser-solid interactions. *Phys. Rev. Lett.*, 84(7):1459, 2000.

[32] W. Kruer and K. Estabrook. J×B heating by very intense laser light. *Phys. Fluids*, 28:430, 1985.

[33] S. C. Wilks, W. L. Kruer, M. Tabak, and A. B. Langdon. Absorption of ultra-intense laser pulses. *Phys. Rev. Lett.*, 69(9):1383, 1992.

[34] P. McKenna, K. W. D. Ledingham, J. M. Yang, L. Robson, T. McCanny, S. Shimizu, R. J. Clarke, D. Neely, K. Spohr, R. Chapman, R. P. Singhal, K. Krushelnick, M. S. Wei, and P. A. Norreys. Characterization of proton and heavier ion acceleration in ultrahigh-intensity laser interactions with heated target foils. *Physical Review E (Statistical, Nonlinear, and Soft Matter Physics)*, 70(3):036405, 2004.

[35] A. Maksimchuk, S. Gu, K. Flippo, D. Umstadter, and V. Yu. Bychenkov. Forward ion acceleration in thin films driven by a high-intensity laser. *Phys. Rev. Lett.*, 84(18):4108, 2000.

[36] A. J. Mackinnon, Y. Sentoku, P. K. Patel, D. W. Price, S. Hatchett, M. H. Key, C. Andersen, R. Snavely, and R. R. Freeman. Enhancement of proton acceleration by hot-electron recirculation in thin foils irradiated by ultraintense laser pulses. *Phys. Rev. Lett.*, 88(21):215006, 2002.

[37] W. Sentoku, T. E. Cowan, A. Kemp, and H. Ruhl. High energy proton acceleration in tnteraction of short laser pulse with dense plasma target. *Physics of Plasmas*, 10:2009, 2003.

[38] S. C. Wilks, A. B. Langdon, T. E. Cowan, M. Roth, M. Singh, S. Hatchett, M. H. Key, D. Pennington, A. MacKinnon, and R. A. Snavely. Energetic proton generation in ultra-intense laser–solid interactions. *Physics of Plasmas*, 8(2):542, 2001.

[39] E. L. Clark, K. Krushelnick, J. R. Davies, M. Zepf, M. Tatarakis, F. N. Beg, A. Machacek, P. A. Norreys, M. I. K. Santala, I. Watts, and A. E. Dangor. Measurements of energetic proton transport through magnetized plasma from intense laser interactions with solids. *Phys. Rev. Lett.*, 84(4):670, 2000.

[40] R. A. Snavely, M. H. Key, S. P. Hatchett, T. E. Cowan, M. Roth, T. W. Phillips, M. A. Stoyer, E. A. Henry, T. C. Sangster, M. S. Singh, S. C. Wilks, A. MacKinnon, A. Offenberger, D. M. Pennington, K. Yasuike, A. B. Langdon, B. F. Lasinski, J. Johnson, M. D. Perry, and E. M. Campbell. Intense high-energy proton beams from petawatt-laser irradiation of solids. *Phys. Rev. Lett.*, 85(14):2945, 2000.

[41] P. Mora. Plasma expansion into a vacuum. *Phys. Rev. Lett.*, 90(18):185002, 2003.

[42] J. E. Crow, P. L. Auer, and J. E. Allen. The expansion of a plasma into a vacuum. *Journal of Plasma Physics*, 14:65, 1975.

[43] S. P. Hatchett, C. G. Brown, T. E. Cowan, E. A. Henry, J. S. Johnson, M. H. Key, J. A. Koch, A. B. Langdon, B. F. Lasinski, Richard W. Lee, A. J. Mackinnon, D. M. Pennington, M. D. Perry, T. W. Phillips, M. Roth, T. C. Sangster, Mike S. Singh, R. A. Snavely, M. A. Stoyer, S. C. Wilks, and K. Yasuike. *AIP*, 7(5):2076, 2000.

[44] J. Fuchs, P. Antici, E. d'Humiares, E. Lefebvre, M. Borghesi, E. Brambrink, C. A. Cecchetti, M. Kaluza, V. Malka, M. Manclossi, S. Meyroneinc, P. Mora, J. Schreiber, T. Toncian, H. Papin, and P. Audebert. Energetic proton generation in ultra-intense laser–solid interactions. *Nature Physics*, 2:48, 2006.

[45] M. Passoni, V. T. Tikhonchuk, M. Lontano, and V. Yu. Bychenkov. Charge separation effects in solid targets and ion acceleration with a two-temperature electron distribution. *Physical Review E (Statistical, Nonlinear, and Soft Matter Physics)*, 69(2):026411, 2004.

[46] V. Chvykov, P. Rousseau, S. Reed, G. Kalinchenko, and V. Yanovsky. Reply to comment on "generation of 10^{11} contrast 50 TW laser pulses". *Opt. Lett.*, 31(20):2993, 2006.

[47] D. E. Spence, P. N. Kean, and W. Sibbett. 60-fsec pulse generation from a self-mode-locked ti:sapphire laser. *Opt. Lett.*, 16(1):42, 1991.

[48] U. Keller, G. W. 'tHooft, W. H. Knox, and J. E. Cunningham. Femtosecond pulses from a continuously self-starting passively mode-locked Ti:sapphire laser. *Opt. Lett.*, 16(13):1022, 1991.

[49] H. A. Haus. Mode-locking of lasers. *IEEE J. Select. Top. Quant. Elect*, 6:1173, 2000.

[50] W. Koechner. *Solid-state Laser Engineering.* Springer, 1999.

[51] P. S. Banks, M. D. Perry, V. Yanovsky, S. N. Fochs, B. C. Stuart, and J. Zweiback. Novel all-reflective stretcher for chirped-pulse amplification ofultrashort pulses. *IEEE J. Quant. Elect*, 36:268, 2000.

[52] V. Yanovsky, C. Felix, and G. Mourou. High-energy broad-band regenerative amplifier for chirped-pulse amplification. *Selected Topics in Quantum Electronics, IEEE Journal of*, 7(4):539, Jul/Aug 2001.

[53] M. Born and E. Wolf. *Principles of Optics: Electromagnetic Theory of Propagation, Interference and Diffraction of Light.* Cambridge University Press, 1999.

[54] J. Primot. Theoretical description of Shack-Hartmann wave-front sensor. *Opt Comm*, 222:81, 2003.

[55] S.-W. Bahk, P. Rousseau, T. A. Planchon, V. Chvykov, G. Kalintchenko, A. Maksimchuk, G. A. Mourou, and V. Yanovsky. Generation and characterization of the highest laser intensities (10^{22} W/cm^2). *Opt. Lett.*, 29(24):2837, 2004.

[56] J. Itatani, J. Faure, M. Nantel, G. Mourou, and S. Watanabe. Suppression of the amplified spontaneous emission in chirped-pulse-amplification lasers by clean high-energy seed-pulse injection. *Opt. Comm.*, 148:70, 1998.

[57] G. Doumy, F. Quéré, O. Gobert, M. Perdrix, Ph. Martin, P. Audebert, J. C. Gauthier, J. P. Geindre, and T. Wittmann. Complete characterization of a plasma mirror for the production of high-contrast ultraintense laser pulses. *Physical Review E (Statistical, Nonlinear, and Soft Matter Physics)*, 69(2):026402, 2004.

[58] A. Jullien, O. Albert, F. Burgy, G. Hamoniaux, J. P. Rousseau, J. P. Chambaret, F. A. Rochereau, G. Chériaux, J. Etchepare, N. Minkovski, and S. M.

Saltiel. temporal contrast for femtosecond ultraintense lasers by cross-polarized wave generation. *Opt. Lett.*, 30(8):920, 2005.

[59] N. Minkovski, S. M. Saltiel, G. I. Petrov, O. Albert, and J. Etchepare. Polarization rotation induced by cascaded third-order processes. *Opt. Lett.*, 27(22):2025, 2002.

[60] R. DeSalvo, M. Sheik-Bahae, A. A. Said, D. J. Hagan, and E. W. Van Stryland. Z-scan measurements of the anisotropy of nonlinear refraction and absorption in crystals. *Opt. Lett.*, 18(3):194, 1993.

[61] V. Yanovsky, C. Felix, and G. Mourou. Why ring regenerative amplification (regen). *Applied Physics B: Lasers and Optics*, 74(1):s181, 2004.

[62] A. Maksimchuk, S. Reed, N. Naumova, V. Chvykov, B. Hou, G. Kalintchenko, T. Matsuoka, J. Nees, P. Rousseau, G. Mourou, and V. Yanovsky. Generation and characterization of quasi-monoenergetic electron beams from laser wakefield. *Journal de Physique IV (Proceedings)*, 133:1123, 2006.

[63] S. A. Reed, V. Chvykov, G. Kalintchenko, T. Matsuoka, V. Yanovsky, C. R. Vane, J. R. Beene, D. Stracener, D. R. Schultz, and A. Maksimchuk. Efficient initiation of photonuclear reactions using quasimonoenergetic electron beams from laser wakefield acceleration. *J. Appl. Phys.*, 102:073103, 2007.

[64] N. H. Matlis, S. Reed, S. S. Bulanov, V. Chvykov, G. Kalintchenko, T. Matsuoka, P. Rousseau, V. Yanovsky, A. Maksimchuk, S. Kalmykov, G. Shvets, and M. C. Downer. Snapshots of laser wakefields. *Nature Physics*, 2:749, 2006.

[65] Nuclear structure NuDat and National Nuclear Data Center (NNDC); http://www.nndc.bnl.gov/nudat2/. decay Data.

[66] National Nuclear Data Center (NNDC); (CSISRS alias EXFOR); http://www.nndc.bnl.gov/exfor/exfor00.htm. EXFOR 2005, Experimental Nuclear Reaction Data.

[67] G. Malka, M. M. Aleonard, J. F. Chemin, G. Claverie, M. Harston, V. T. Tikhonchuk, J. N. Scheurer, S. Fritzler, V. Malka, P. Balcou, G. Grillon, S. D. Moustaizis, L. Notebaert, M. Pittman, and E. Lefebvre. Optimizing photonuclear reactions with a high-intensity laser. *Proc. SPIE*, 4510(1):47–51, 2001.

[68] Detector Description GEANT3 and 1994 Simulation Tool, CERN Program Library Long Writeup W5013.

[69] P. A. Norreys, M. Santala, E. Clark, M. Zepf, I. Watts, F. N. Beg, K. Krushelnick, M. Tatarakis, A. E. Dangor, X. Fang, P. Graham, T. McCanny, R. P. Singhal, K. W. D. Ledingham, A. Creswell, D. C. W. Sanderson, J. Magill, A. Machacek, J. S. Wark, R. Allott, B. Kennedy, and D. Neely. Observation of a highly directional γ-ray beam from ultrashort, ultraintense laser pulse interactions with solids. *Phys. Plasmas*, 6:2150, 1999.

[70] W. P. Leemans, P. Catravas, E. Esarey, C. G. R. Geddes, C. Toth, R. Trines, C. B. Schroeder, B. A. Shadwick, J. van Tilborg, and J. Faure. Electron-yield enhancement in a laser-wakefield accelerator driven by asymmetric laser pulses. *Phys. Rev. Lett.*, 89(17):174802, 2002.

[71] S. Reed, V. Chvykov, G. Kalintchenko, T. Matsuoka, P. Rousseau, V. Yanovsky, C.R. Vane, J.R. Beene, D. Stracener, D. R. Schultz, and A. Maksimchuk. Photonuclear fission with quasimonoenergetic electron beams from laser wakefields. *Appl. Phys. Lett.*, 89:231107, 2006.

[72] V. A. Rubchenya and J. Aysto. Theoretical predictions for neutron rich fission product yields: Study for rnb projects. *EURISOL Research Report*, 2003.

[73] H. Schwoerer, F. Ewald, R. Sauerbrey, J. Galy, J. Magill, V. Rondinella, R. Schenkel, and T. Butz. Fission of actinides using a tabletop laser. *Europhys. Lett*, 61(1):47, 2003.

[74] K. W. D. Ledingham, I. Spencer, T. McCanny, R. P. Singhal, M. I. K. Santala, E. Clark, I. Watts, F. N. Beg, M. Zepf, K. Krushelnick, M. Tatarakis, A. E. Dangor, P. A. Norreys, R. Allott, D. Neely, R. J. Clark, A. C. Machacek, J. S. Wark, A. J. Cresswell, D. C. W. Sanderson, and J. Magill. Photonuclear physics when a multiterawatt laser pulse interacts with solid targets. *Phys. Rev. Lett.*, 84(5):899, 2000.

[75] T. E. Cowan, M. Roth, J. Johnson, C. Brown, M. Christ, W. Fountain, S. Hatchett, E. A. Henry, A. W. Hunt, M. H. Key, A. MacKinnon, T. Parnell, D. M. Pennington, M. D. Perry, T. W. Phillips, T. C. Sangster, M. Singh, R. Snavely, M. Stoyer, Y. Takahashi, S. C. Wilks, and K. Yasuike. Intense electron and proton beams from petawatt laser-matter interaction. *Nuclear Instruments and Methods in Physics Research A*, 455:130, 2000.

[76] T. E. Cowan, A. W. Hunt, T. W. Phillips, S. C. Wilks, M. D. Perry, C. Brown, W. Fountain, S. Hatchett, J. Johnson, M. H. Key, T. Parnell, D. M. Pennington, R. A. Snavely, and Y. Takahashi. Photonuclear fission from high energy electrons from ultraintense laser-solid interactions. *Phys. Rev. Lett.*, 84(5):903, 2000.

[77] J. T. Caldwell, E. J. Dowdy, B. L. Berman, R. A. Alvarez, and P. Meyer. Giant resonance for the actinide nuclei: Photoneutron and photofission cross sections for ^{235}U, ^{236}U, ^{238}U, and ^{232}Th. *Phys. Rev. C*, 21(4):1215, 1980.

[78] J. C. Sanabria, B. L. Berman, C. Cetina, P. L. Cole, G. Feldman, N. R. Kolb, R. E. Pywell, J. M. Vogt, V. G. Nedorezov, A. S. Sudov, and G. Ya. Kezerashvili. Photofission of actinide nuclei in the quasideuteron and lower part of the δ energy region. *Phys. Rev. C*, 61(3):034604, 2000.

[79] Y. Glinec, J. Faure, A. Guemnie-Tafo, V. Malka, H. Monard, J. P. Larbre, V. De Waele, J. L. Marignier, and M. Mostafavi. Absolute calibration for a

broad range single shot electron spectrometer. *Rev. Sci. Instrum*, 77:103301, 2006.

[80] M. Borghesi, D. H. Campbell, A. Schiavi, M. G. Haines, and O. Willi. Electric field detection in laser-plasma interaction experiments via the proton imaging technique. *Phys. Plasmas*, 9(5):2214, 2002.

[81] S. V. Bulanov, T. Zh. Esirkepov, V. S. Khoroshkov, A. V. Kuznetsov, and F. Pegoraro. Oncological hadrontherapy with laser ion accelerators. *Phys. Letters A*, 299(2-3):240, 2002.

[82] S. J. Gitomer, R. D. Jones, F. Begay, A. W. Ehler, J. F. Kephart, and R. Kristal. Fast ions and hot electrons in the laserplasma interaction. *Phys. of Fluids*, 29(8):2679, 1986.

[83] J. R. Davies. Proton acceleration by fast electrons in lasersolid interactions. *Laser and Particle Beams*, 20(2):243, 2002.

[84] S. S. Bulanov, A. Brantov, V. Y. Bychenkov, V. Chvykov, G. Kalinchenko, T. Matsuoka, P. Rousseau, S. Reed, V. Yanovsky, K. Krushelnick, D. W. Litzenberg, and A. Maksimchuk. Accelerating protons to therapeutic energies with ultra-intense ultra-clean and ultra-short laser pulses. *Phys. Rev. Lett.*, 2007 (submitted).

[85] M. Zepf, E. L. Clark, F. N. Beg, R. J. Clarke, A. E. Dangor, A. Gopal, K. Krushelnick, P. A. Norreys, M. Tatarakis, U. Wagner, and M. S. Wei. Proton acceleration from high-intensity laser interactions with thin foil targets. *Phys. Rev. Lett.*, 90(6):064801, 2003.

[86] A. Pukhov. Three-dimensional simulations of ion acceleration from a foil irradiated by a short-pulse laser. *Phys. Rev. Lett.*, 86(16):3562, 2001.

[87] E. d'Humires, E. Lefebvre, L. Gremillet, and V. Malka. Proton acceleration mechanisms in high-intensity laser interaction with thin foils. *Phys. Plasmas*, 12:062704, 2005.

[88] F. Pisani, A. Bernardinello, D. Batani, A. Antonicci, E. Martinolli, M. Koenig, L. Gremillet, F. Amiranoff, S. Baton, J. Davies, T. Hall, D. Scott, P. Norreys, A. Djaoui, C. Rousseaux, P. Fews, H. Bandulet, and H. Pepin. Experimental evidence of electric inhibition in fast electron penetration and of electric-field-limited fast electron transport in dense matter. *Phys. Rev. E*, 62(5):R5927, 2000.

[89] S. Sengupta, A. S. Sandhu, G. R. Kumar, A. Das, and P. K. Kaw. Short laser pulse induced generation of hot electrons and their anomalous stopping in overdense plasmas. *Nucl. Fusion*, 45(11):1377, 2005.

[90] R. A. Snavely, M. H. Key, S. P. Hatchett, T. E. Cowan, M. Roth, T. W. Phillips, M. A. Stoyer, E. A. Henry, T. C. Sangster, M. S. Singh, S. C. Wilks, A. MacKinnon, A. Offenberger, D. M. Pennington, K. Yasuike, A. B. Langdon, B. F. Lasinski, J. Johnson, M. D. Perry, and E. M. Campbell. Intense high-energy proton beams from petawatt-laser irradiation of solids. *Phys. Rev. Lett.*, 85(14):2945, 2000.

[91] Y. Kishimoto, K. Mima, T. Watanabe, and K. Nishikawa. Analysis of fast-ion velocity distributions in laser plasmas with a truncated maxwellian velocity distribution of hot electrons. *Phys. Fluids*, 26(8):2308, 1983.

[92] V. Yu. Bychenkov, V. N. Novikov, D. Batani, V. T. Tikhonchuk, and S. G. Bochkarev. Ion acceleration in expanding multispecies plasmas. *Phys. Fluids*, 11(6):3242, 2004.

[93] A. M. Koehler. Proton radiography. *Science*, 160(3825):303, 1969.

[94] M. Borghesi, A. J. Mackinnon, D. H. Campbell, D. G. Hicks, S. Kar, P. K. Patel, D. Price, L. Romagnani, A. Schiavi, and O. Willi. Multi-mev proton source investigations in ultraintense laser-foil interactions. *Physical Review Letters*, 92(5):055003, 2004.

[95] T. E. Cowan, J. Fuchs, H. Ruhl, A. Kemp, P. Audebert, M. Roth, R. Stephens, I. Barton, A. Blazevic, E. Brambrink, J. Cobble, J. Fernández, J.-C. Gauthier, M. Geissel, M. Hegelich, J. Kaae, S. Karsch, G. P. Le Sage, S. Letzring, M. Manclossi, S. Meyroneinc, A. Newkirk, H. Pépin, and N. Renard-LeGalloudec. Ultralow emittance, multi-MeV proton beams from a laser virtual-cathode plasma accelerator. *Physical Review Letters*, 92(20):204801, 2004.

[96] A. J. Kemp, R. E. W. Pfund, and J. Meyer ter Vehn. Modeling ultrafast laser-driven ionization dynamics with monte carlo collisional particle-in-cell simulations. *Physics of Plasmas*, 11(12):5648, 2004.

[97] S. J. Gitomer, R. D. Jones, F. Begay, A. W. Ehler, J. F. Kephart, and R. Kristal. Fast ions and hot electrons in the laserplasma interaction. *Physics of Fluids*, 29(8):2679, 1986.

[98] D. J. Bond, J. D. Hares, and J. D. Kilkenny. Demonstration of resistive inhibition of fast electrons from laser-produced plasmas in low-density gold targets. *Phys. Rev. Lett.*, 45(4):252, 1980.

[99] B. Luther-Davies, A. Perry, and K. A. Nugent. K_α emission measurements and superthermal electron transport in layered laser-irradiated disk targets. *Phys. Rev. A*, 35(10):4306, 1987.

[100] National Institute of Standards, Technology (NIST): Stopping Power, Range Tables for protons, electrons respectively.

http://physics.nist.gov/PhysRefData/Star/Text/PSTAR.html, and http://physics.nist.gov/PhysRefData/Star/Text/ESTAR.html.

[101] J. T. Larsen and S. M. Lane. Hyades: A plasma hydrodynamics code for dense plasma studies. *J. Quant. Spectrosc. Radiat. Transfer*, 51:179, 1994.

[102] T. Zh. Esirkepov. Exact charge conservation scheme for particle-in-cell simulation with an arbitrary form-factor. *Computer Physics Communications*, 135(2):144, 2001.

[103] E. L. Clark, K. Krushelnick, M. Zepf, F. N. Beg, M. Tatarakis, A. Machacek, M. I. K. Santala, I. Watts, P. A. Norreys, and A. E. Dangor. Energetic heavy-ion and proton generation from ultraintense laser-plasma interactions with solids. *Phys. Rev. Lett.*, 85(8):1654, 2000.

[104] D. Neely, P. Foster, A. Robinson, F. Lindau, O. Lundh, A. Persson, C. G. Wahlström, and P. McKenna. Enhanced proton beams from ultrathin targets driven by high contrast laser pulses. *Appl. Phys. Lett.*, 89:021502, 2006.

[105] P. E. Young, C. H. Still, D. E. Hinkel, W. L. Kruer, E. A. Williams, R. L. Berger, and K. G. Estabrook. Observations of laser-beam bending due to transverse plasma flow. *Phys. Rev. Lett.*, 81(7):1425, 1998.

[106] D. J. Spence and S. M. Hooker. Investigation of a hydrogen plasma waveguide. *Phys. Rev. E*, 63(1):015401, 2000.

[107] A. Butler, D. J. Spence, and S. M. Hooker. Guiding of high-intensity laser pulses with a hydrogen-filled capillary discharge waveguide. *Phys. Rev. Lett.*, 89(18):185003, 2002.

[108] K. A. Janulewicz, M. Schnürer, J. Tümmler, G. Priebe, E. Risse, P. V. Nickles, B. Greenberg, M. Levin, A. Pukhov, P. Mandelbaum, and A. Zigler. Enhancement of a 24.77-nm line emitted by the plasma of a boron nitride capillary discharge irradiated by a high-intensity ultrashort laser pulse. *Opt. Lett.*, 30(12):1572, 2005.

[109] W. P. Leemans, B. Nagler, A. J. Gonsalves, Cs. Tóth, K. Nakamura, C. G. R. Geddes, E. Esarey, C. B. Schroeder, and S. M. Hooker. Gev electron beams from a centimetre-scale accelerator. *Nature Physics*, 2:696, 2006.